A MULTI-FIDELITY NUMERICAL FRAMEWORK FOR PREDICTING WIND LOADS ON BUILDINGS

A DISSERTATION
SUBMITTED TO THE DEPARTMENT OF CIVIL AND ENVIRONMENTAL ENGINEERING
AND THE COMMITTEE ON GRADUATE STUDIES
OF STANFORD UNIVERSITY
IN PARTIAL FULFILLMENT OF THE REQUIREMENTS
FOR THE DEGREE OF
DOCTOR OF PHILOSOPHY

Giacomo Lamberti
September 2020

Preface

According to the Revision of World Urbanization Prospects, published by the United Nations in 2018, 2.5 billion people are expected to populate big cities by 2050. As a consequence, the number of high-rise buildings has drastically increased over the last decades, to fulfill the need of expansion of urban areas [2]. Not only are tall buildings increasing in number, they are also becoming taller, more slender and complex in shape, making the design process very challenging. Another recent tendency in high-rise buildings' construction is the employment of glazed panels to cover the external facades. Cladding design requires accurate estimations of wind loads to guarantee the structural integrity of the panels, without resorting to overly conservative designs. This is especially important near the corners and edges of high-rise buildings' side walls, where the wind-induced pressure can result in extreme suction loads.

Nowadays wind tunnel experiments are required by the building standards to estimate the wind loads on tall buildings and their components. The procedure is well established, but limited in the number of measurements locations and spatial resolution. Computational fluid-dynamics (CFD) offers an attractive alternative to the wind engineering community, given the potential to provide the complete 3-dimensional flow field in complex geometries with a spatial resolution equal to the grid resolution. Nevertheless, significant progress is still necessary to guarantee the accuracy of the results and extensively employ CFD simulations for design purposes. In addition, the computational cost should be reasonable to practically use the simulations in the design process.

The accuracy of CFD simulations of atmospheric boundary layer (ABL) flows can be compromised by two factors: uncertainties in the operating parameters, such as the boundary conditions, and simplified model assumptions, such as the turbulence model. The presence of these uncertainties is limiting the use of CFD to qualitative analysis in early design phases. This could be addressed by incorporating methods for uncertainty quantification (UQ) in the predictive models. By providing predictions in terms of mean values and confidence intervals, the models can provide significantly more meaningful information to designers and engineers than the outcome of a single deterministic simulation.

Therefore, the long-term goal of this research is to enable the extensive use of CFD simulations

throughout the different phases of high-rise building's design, by improving the reliability and efficiency of the numerical simulations. To achieve this goal, two CFD models with different level of fidelity and computational cost are employed: large-eddies simulations (LES) and Reynolds-averaged Navier-Stokes (RANS) simulations. Validation with wind tunnel data is carried out at all stages, to evaluate the performance of the proposed numerical framework.

LES can directly provide the main quantities of interest (QoIs) of cladding design, i.e. the peak pressure distribution around the building and the design pressure of the panels. However, the generation of proper inflow conditions can be challenging and result in significant uncertainty in the results. Therefore the first goal of this thesis is to address this challenge and improve the confidence in the LES prediction of the pressure distribution around high-rise buildings. As a first step, an inflow generation method able to accurately produce user-specified turbulence statistics, while maintaining low computational cost, is developed. The method is the starting point of a LES UQ framework, that has not only the goal to produce desired ABL statistics, but also to account for the inherent uncertainty in the definition of these target profiles. The framework provides a systematic way to address the great sensitivity to the inflow conditions, that LES on high-rise buildings manifested in literature [123]. The results demonstrate that, if the incoming boundary layer is properly generated and the underlying uncertainty is considered, LES can provide accurate prediction of the QoIs of cladding design.

The computational cost of LES simulations can be prohibitive for wind engineering applications, especially during the early phases of design; for this reason, despite the turbulence model represents an important source of error, RANS simulations still represent an attractive tool. In this regard, the second objective of this thesis is to improve the confidence in the RANS prediction of the mean pressure distribution around the building, by quantifying the combined effect of uncertainties in the inflow conditions and turbulence model. The results confirm the well know RANS limitations in dealing with the flow around bluff bodies and the great level of uncertainty introduced by the turbulence model. Therefore, to overcome these issues a multi-fidelity framework is established, by leveraging a limited number of LES simulations. Validation against LES at different wind directions, shows significant improvement in the mean pressure prediction, over the standard RANS method.

When designing cladding systems, we are ultimately interested in the pressure fluctuations. Therefore, the third objective of the thesis is to extend the multi-fidelity framework to enable the calculation of the root mean square pressure from RANS simulations and a limited number of LES. In this regard, a machine learning framework is proposed, to relate the LES data of rms pressure coefficient to RANS time-averaged quantities. The results demonstrate that the procedure has the potential to drastically reduce the number of LES simulations needed for design, while assuring good level of accuracy.

Contents

Preface **iv**

1 Introduction **1**
1.1 Motivation . . . 1
1.2 Objectives . . . 2
1.3 Structure of the thesis . . . 4

2 State of the art **6**
2.1 Wind tunnel experiments . . . 6
2.1.1 Pressure peaks . . . 7
2.1.2 Extreme value analysis . . . 7
2.2 CFD simulations . . . 8
2.2.1 LES . . . 9
2.2.2 RANS . . . 10
2.3 Summary . . . 13

3 Wind Tunnel experiments **15**
3.1 Experimental setup . . . 16
3.1.1 Velocity measurements . . . 16
3.1.2 Pressure measurements . . . 17
3.2 Quantities of interest . . . 19
3.3 Results . . . 19
3.3.1 Velocity statistics . . . 20
3.3.2 Pressure statistics . . . 22
3.3.3 Pressure peaks . . . 25
3.3.4 Extreme value analysis . . . 32
3.4 Summary . . . 33

4 LES: optimizing inflow conditions **35**
4.1 CFD model . . . 35
4.2 Preliminary results . . . 37
4.2.1 Baseline simulation . . . 37
4.2.2 Sensitivity analysis . . . 40
4.3 Gradient-based optimization . . . 43
4.3.1 Bezier parametrization . . . 43
4.3.2 Objective functions . . . 44
4.4 Results . . . 45
4.4.1 Optimization of input Reynolds stresses . . . 45
4.4.2 Optimization of input Reynolds stresses and time scales . . . 49
4.5 Summary . . . 50

5 LES: inflow sensitivity analysis **52**
5.1 Methods . . . 52
5.1.1 CFD model . . . 52
5.1.2 Characterization of the inflow uncertainty . . . 54
5.2 Results . . . 55
5.2.1 Baseline LES . . . 55
5.2.2 Velocity statistics . . . 59
5.2.3 Pressure statistics . . . 61
5.3 Summary . . . 71

6 RANS: inflow and turbulence model UQ **73**
6.1 Methods . . . 74
6.1.1 CFD model . . . 74
6.1.2 Inflow UQ . . . 75
6.1.3 Turbulence model UQ . . . 76
6.1.4 Second order probability . . . 77
6.2 Results . . . 77
6.2.1 Inflow UQ . . . 78
6.2.2 Turbulence model UQ . . . 80
6.2.3 Second order probability . . . 85
6.3 Summary . . . 91

7 Multi-fidelity framework **94**
7.1 CFD models . . . 95
7.1.1 RANS . . . 95

7.1.2 LES . . . 95
7.2 Multi-fidelity method . . . 95
7.3 Results . . . 97
7.3.1 Mean pressure coefficient . . . 97
7.3.2 Rms pressure coefficient . . . 103
7.4 Summary . . . 107

8 Multi-fidelity machine learning framework 111
8.1 Machine learning method . . . 111
8.1.1 Features and Dataset . . . 112
8.1.2 Principal component analysis . . . 114
8.1.3 Hyperparameters and model search . . . 115
8.2 Results . . . 116
8.2.1 Comparison of RMSE . . . 119
8.2.2 0° wind direction . . . 119
8.2.3 20° wind direction . . . 120
8.2.4 40° wind direction . . . 122
8.2.5 60° wind direction . . . 124
8.2.6 80° wind direction . . . 124
8.3 Summary . . . 126

9 Conclusions 128
9.1 Contributions . . . 128
9.2 Future work . . . 129

Bibliography 130

List of Tables

3.1 Sampling frequency, total duration and reference velocity at roof height for the velocity measurements performed in both facilities. 17

3.2 Sampling frequency, total duration and reference velocity at roof height for the pressure measurements performed in both facilities. 18

3.3 Peak pressure coefficient relative to a 22% probability of exceedance, 20° wind direction. 33

6.1 Inflow uncertain parameters. 75

7.1 Root mean square error (RMSE) of C_P prediction. 98

7.2 Root mean square error (RMSE) of C_p' prediction. 103

8.1 Features of the machine learning model, where τ_w is the wall shear stress vector and H the height of the building; ν and ρ are the kinematic viscosity and density of the air, respectively. 112

8.2 Kullback-Leibler divergence between wind directions in the test and training sets. . . 115

8.3 Root mean square error (RMSE) of the selected models. 115

8.4 Root mean square error (RMSE) of the neural network and Paterson-Holmes models, for each of the 5 wind directions in the test set. 118

List of Figures

1.1 Structure of the proposed numerical framework, where $C_{P,RANS}$, $C_{P,MF}$ and $C_{P,LES}$ are the mean pressure coefficients outcome of the RANS, multi-fidelity and LES frameworks, respectively; similarly, $C'_{p,MF}$, $\check{C}_{p,MF}$, $C'_{p,LES}$ and $\check{C}_{p,LES}$ are the rms and peak pressure coefficients outcome of the multi-fidelity and LES methods. 5

3.1 PoliMi experimental setup of velocity measurements. 16
3.2 Sketch of the building model. 17
3.3 Pictures of the test sections of both wind tunnels and close-up of the aluminum tiles. 18
3.4 Comparison of nondimensional mean velocity between PoliMi and WoW data. 20
3.5 Comparison of turbulence intensities between PoliMi and WoW data. 20
3.6 Comparison of nondimensional integral time-scales between PoliMi and WoW data. . 21
3.7 Comparison of streamwise velocity spectra between PoliMi and WoW data at 0.67m height, compared to the Von-Karman spectrum adapted for wind engineering [38]. . 21
3.8 Comparison of pressure coefficient first and second order statistics at 0°. Once again, tiles on the right and on the left of each subplot refer to 0° and 180° wind directions respectively. 22
3.9 Comparison of mean and rms pressure coefficients at 0° wind direction. 23
3.10 Non-dimensional power spectral density of the pressure coefficient at 0° wind direction on top-corner and mid-edge taps. 24
3.11 Comparison of mean and rms pressure coefficients at 20° wind direction. 25
3.12 Comparison of pressure coefficient first and second order statistics at 20° wind direction. 26
3.13 Non-dimensional power spectral density of the pressure coefficient at 20° wind direction on top-corner and mid-edge taps. 26
3.14 Time-series of pressure coefficient at 20° wind direction on top-corner tap. The red arrows indicate the negative peaks lower than $C_p = -5$ 27
3.15 Probability density functions of pressure coefficient at 20° wind direction. 28
3.16 Probability density functions of area-averaged pressure coefficient on $2 \times 3\text{m}^2$ panels, at 20° wind direction. 29

3.17 Time-series of pressure coefficient at 20° wind direction on top-corner tap, the red arrows indicate a negative peak lower than $C_p = -5$, and distribution of pressure coefficient around the tile at the time instant of the negative peak. 30
3.18 Time-series of pressure coefficient at 20° wind direction on top-corner tap, the red arrows indicate a negative peak lower than $C_p = -5$, and distribution of pressure coefficient around the tile at the time instant of the negative peak. 31
3.19 Comparison of peak pressure coefficients relative to a 22% probability of exceedance, at 20° wind directions. 32
3.20 Design pressure coefficient for panels of increasing area, at 20° wind direction.. . . . 33

4.1 Generation of synthetic turbulence in the LES. Iso-surfaces of the second invariant of the velocity gradient tensor Q colored by values of velocity magnitude. 36
4.2 Comparison of the experimental mean velocity profile with the mean velocity profile computed by the baseline simulation 5m downstream of the inlet. 38
4.3 Decay of turbulence kinetic energy in the LES. 38
4.4 Comparison of the experimental turbulence kinetic energy and Reynolds stress profiles with the corresponding profiles computed by the baseline simulation 5m downstream of the inlet. 39
4.5 Comparison of the experimental integral length scales with the length scales computed by the baseline simulation 5m downstream of the inlet. 40
4.6 Influence of the inflow parameters on the mean velocity $5m$ downstream of the inlet. The inflow parameters are doubled one at a time; the legend indicates the doubled parameter. 41
4.7 Influence of the inflow parameters on the Reynolds stresses $5m$ downstream of the inlet. The inflow parameters are doubled one at a time; the legend indicates the doubled parameter. 42
4.8 Influence of the inflow parameters on the integral length scales $5m$ downstream of the inlet. The inflow parameters are doubled one at a time; the legend indicates the doubled parameter. 43
4.9 Parametrization of the input Reynolds stresses with Bezier curves. 44
4.10 Input Reynolds stresses modified by the optimization. 45
4.11 Reynolds stresses 5m downstream of the inlet as a result of the optimization. 46
4.12 Modeled integral length-scales 5m downstream of the inlet as a result of the optimization. 47
4.13 Modeled power spectrum, $5m$ downstream of the inlet, as a result of the optimization. 48
4.14 Modeled Reynolds stresses 5m downstream of the inlet as a result of the second optimization problem. 49
4.15 Modeled integral length-scales 5m downstream of the inlet as a result of the second optimization problem. 50

5.1 Domain and mesh 53
5.2 ABL profiles for the inflow sensitivity analysis. 54
5.3 Instantaneous velocity field from the baseline LES simulation. 56
5.4 Power spectral density on top-corner and mid-edge taps. 57
5.5 Time-series of pressure coefficient on top-corner tap. 57
5.6 Time-series of pressure coefficient on top-corner tap and pressure coefficient distribution on the tile at the time instant of the negative peak. 58
5.7 Contours of instantaneous pressure coefficient and iso-surface of the second invariant of the velocity gradient tensor $Q = 2,000\text{s}^{-2}$, colored by the instantaneous pressure coefficient. 59
5.8 Turbulence statistics at the building location from the ensemble of LES. 60
5.9 Effect of the different uncertain inflow parameters on the turbulence statistics at the building location. The profiles are obtained by averaging the results of the simulations with a fixed value for one of the parameters, reported in the corresponding label in the legend. 60
5.10 Mean pressure coefficient distribution on the building's lateral facade. 62
5.11 Mean pressure coefficient profiles: baseline LES (black dots) and sensitivity intervals (gray area) compared to the wind tunnel data (red circles). 62
5.12 Effect of the different uncertain inflow parameters on the mean pressure coefficient profiles. The profiles are obtained by averaging the results of the simulations with a fixed value for one of the parameters, reported in the corresponding label in the legend. 63
5.13 Rms pressure coefficient distribution on the building's lateral facade. 64
5.14 Rms pressure coefficient profiles: baseline LES (black dots) and sensitivity intervals (gray area) compared to the wind tunnel data (red circles). 65
5.15 Effect of the different inflow parameters on the rms pressure coefficient profiles. The profiles are obtained by averaging the results of the simulations with a fixed value for one of the parameters, reported in the corresponding label in the legend. 66
5.16 Distribution of peak pressure coefficient relative to a 22% probability of exceedance on the building's lateral facade. 67
5.17 Profiles of peak pressure coefficient relative to a 22% probability of exceedance: baseline LES (black dots) and sensitivity intervals (gray area) compared to the wind tunnel data (red circles). 68
5.18 Effect of the different inflow parameters on the peak pressure coefficient profiles. The profiles are obtained by averaging the results of the simulations with a fixed value for one of the parameters, reported in the corresponding label in the legend. 69
5.19 Cumulative density functions of the extreme values of the pressure coefficient averaged over a $2 \times 3\text{m}^2$ panel. 70

5.20 Design pressure coefficients as a function of panel size. 70
5.21 Effect of the different inflow parameters on the design pressure coefficient profiles. The profiles are obtained by averaging the results of the simulations with a fixed value for one of the parameters, reported in the corresponding label in the legend. . 71

6.1 Barycentric map. 76
6.2 Mean pressure coefficient on building's lateral facade at 0°. 78
6.3 Profiles of mean and 95% credible interval (black dots and gray region respectively) of pressure coefficient compared to the measurements (red circles) at 0°. 79
6.4 Mean pressure coefficient on building's lateral facade at 20°. 80
6.5 Profiles of mean and 95% credible interval (black dots and gray region respectively) of pressure coefficient compared to the measurements (red circles) at 20°. 81
6.6 Mean velocity contours at half the building height. Baseline simulation with mean inflow parameters and simulations with 1-, 2-, and 3-component perturbations, at 0° wind direction. 81
6.7 Pressure coefficient contours on the lateral facade. Baseline simulation with mean inflow parameters and simulations with 1-, 2-, and 3-component perturbations, at 0° wind direction. 82
6.8 Mean velocity contours at half the building height. Baseline simulation with mean inflow parameters and simulations with 1-, 2-, and 3-component perturbations, at 20° wind direction. 83
6.9 Pressure coefficient contours on the lateral facade. Baseline simulation with mean inflow parameters and simulations with 1-, 2-, and 3-component perturbations, at 20° wind direction. 84
6.10 Sensitivity of the pressure coefficient to the size of the perturbation, at 20° wind direction. 85
6.11 Cumulative density functions of pressure coefficients on four taps at 0°; the result from the inflow UQ (black) is compared to the 1-component perturbation (blue), the 2-component perturbation (orange), the 3-component perturbation (yellow) and the wind tunnel data (red). 86
6.12 Profiles of pressure coefficient at 0° wind direction. Mean and 95% credible interval computed from the inflow UQ (gray), the 1-component perturbation (blue), the 2-component perturbation (green) and the 3-component perturbation (yellow), compared to the measurements (red circles). 88
6.13 Profiles of pressure coefficient at 0°. Mean and credible interval computed from the combination of inflow and turbulence model UQ (gray), compared to the measurements (red circles). 89

6.14 Probability distributions of pressure coefficients computed on top-corner tap at 20°; the result from the inflow UQ (black) is compared to the 1-component perturbation (blue), 2-component perturbation (orange), 3-component perturbation (yellow) and wind tunnel data (red). 90
6.15 Profiles of pressure coefficient at 20°. Mean and 95% credible intervals computed from the inflow UQ (gray), the 1-component perturbation (blue), the 2-component perturbation (green) and the 3-component perturbation (yellow), compared to the measurements (red circles). 91
6.16 Profiles of pressure coefficient at 20°. Mean and credible interval computed from the combination of inflow and turbulence model UQ (gray), compared to the measurements (red circles). 92

7.1 Quadrature points of polynomial expansions. 96
7.2 Contours of mean pressure coefficient at 0°. 98
7.3 Profiles of mean pressure coefficient at 0°. 99
7.4 Contours of mean pressure coefficient at 20°. 100
7.5 Profiles of mean pressure coefficient at 20°. 100
7.6 Contours of mean pressure coefficient at 40°. 101
7.7 Profiles of mean pressure coefficient at 40°. 102
7.8 Contours of mean pressure coefficient at 60°. 102
7.9 Profiles of mean pressure coefficient at 60°. 103
7.10 Contours of rms pressure coefficient at 0°. 104
7.11 Profiles of rms pressure coefficient at 0°. 105
7.12 Contours of rms pressure coefficient at 20°. 106
7.13 Profiles of rms pressure coefficient at 20°. 106
7.14 Contours of rms pressure coefficient at 40°. 107
7.15 Profiles of rms pressure coefficient at 40°. 108
7.16 Contours of rms pressure coefficient at 60°. 108
7.17 Profiles of rms pressure coefficient at 60°. 109

8.1 Contours of the output and features at 0° wind direction. 113
8.2 Sketch of the data-driven approach. 113
8.3 Contours of the joint distribution of the first two principal components. 114
8.4 Neural network acrhirecture. 116
8.5 Contours of rms pressure coefficient at 45° wind direction. 117
8.6 Contours of rms pressure coefficient at 0° wind direction. 120
8.7 Profiles of rms pressure coefficient at 0° wind direction. 121
8.8 Contours of rms pressure coefficient at 20° wind direction. 121

8.9 Profiles of rms pressure coefficient at 20° wind direction. 122
8.10 Contours of rms pressure coefficient at 40° wind direction. 123
8.11 Profiles of rms pressure coefficient at 40° wind direction. 123
8.12 Contours of rms pressure coefficient at 60° wind direction. 124
8.13 Profiles of rms pressure coefficient at 60° wind direction. 125
8.14 Contours of rms pressure coefficient at 80° wind direction. 125
8.15 Profiles of rms pressure coefficient at 80° wind direction. 126

Chapter 1

Introduction

1.1 Motivation

The 2018 Revision of World Urbanization Prospects, produced by the Population Division of the UN Department of Economic and Social Affairs (UN DESA), estimated that around 55% of the world's population today lives in urban areas. An additional 2.5 billion people are expected to populate big cities by 2050, following the trend of continuous population growth and increasing migration from rural to urban areas. As a consequence, the number of high-rise buildings has drastically increased over the last decades, to fulfill the need of expansion of urban areas [2]. According to the 2019 review of the Council on Tall Buildings and Urban Habitat (CTBUH), 126 buildings taller than 200m were completed in 2019, 26 of which are categorized as supertall buildings, higher than 300m.

Not only are tall buildings increasing in number, they are also becoming taller, more slender and complex in shape, making the design process very challenging. Another recent tendency in high-rise buildings' construction is the employment of glazed panels to cover the external facades. Cladding design requires accurate estimations of wind loads to guarantee the structural integrity of the panels, without resorting to overly conservative designs. This is especially important near the corners and edges of high-rise buildings' side walls, where the wind-induced pressure is characterized by a strong non-Gaussian behavior [40, 116, 63, 101, 93, 19] that can result in extreme suction loads. Importantly, pressure peaks with different characteristics have been observed on the lateral facade of high-rise buildings: some events are extremely localized in space and time, while others have a larger spatial and temporal extent [4]. The former are usually the strongest events, but are not expected to cause significant damage to the facade; the latter, even though weaker, should determine the design loads. To properly dimension glazed panels, it is important to distinguish between these two kinds of phenomena.

Different methods are commonly employed to predict wind loads on buildings and their components, such as building codes, wind tunnel tests and numerical simulations. Building codes represent

the simplest approach; they provide the design pressure loads using analytic expressions that are functions of many operating parameters, which aim to represent standardized building sites and geometries. Nonetheless, when considering structures like high-rise buildings, for which wind forces can be the most critical loads, the details of the building's site and geometry need to be represented more accurately. In this case, wind tunnel experiments are required, since they represent the most reliable method. The main drawback of wind tunnel experiments lies in limitations in terms of the number of measurement locations and their spatial resolution. When dimensioning components like glazed panels, the number of pressure taps required to accurately estimate the local pressure distribution can be too high for routine wind tunnel tests; therefore, alternative solutions are needed to estimate the area-averaged pressure acting on the panels from limited measurement locations. Computational fluid-dynamics (CFD) offers an attractive alternative to the wind engineering community, given the potential to provide the complete 3-dimensional flow field in complex geometries with a spatial resolution equal to the grid resolution. Nevertheless, significant progress is still necessary to guarantee the accuracy of the results and extensively employ CFD simulations for design purposes. This is particularly true when considering complex wind loading problems, in which the accuracy of the results is critical to assure structural integrity. In addition, the computational cost should be reasonable to practically use the simulations in the design process.

The accuracy of CFD simulations of atmospheric boundary layer (ABL) flows can be compromised by two factors: uncertainties in the operating parameters, such as the boundary conditions, and simplified model assumptions, such as the turbulence model. The uncertainties in the operating parameters can be classified as aleatory uncertainties, because they are inherent to the problem and cannot be reduced by additional knowledge; aleatory uncertainties can be naturally defined within a stochastic framework [110]. Simplified model assumptions represent instead epistemic uncertainties, which could be reduced by including additional physics in the model; these are not easily defined within a probabilistic framework [110]. The presence of these uncertainties is limiting the use of CFD to qualitative analysis in early design phases. This could be addressed by incorporating methods for uncertainty quantification (UQ) in the predictive models. By providing predictions in terms of mean values and confidence intervals, the models will provide significantly more meaningful information to designers and engineers, than the outcome of a single deterministic simulation.

1.2 Objectives

The long-term goal of this research is to enable the extensive use of CFD simulations throughout the different phases of high-rise building's design, by improving the reliability and efficiency of the numerical simulations. To achieve this goal, two CFD models with different level of fidelity and computational cost will be employed: large-eddies simulations (LES) and Reynolds-averaged Navier-Stokes (RANS) simulations.

LES can directly provide the main quantities of interest for cladding design, i.e. the peak pressure distribution around the building and the design pressure of the panels. However, the generation of proper inflow conditions can be challenging and result in significant uncertainty in the results. Therefore the first goal of this thesis is to address this challenge and improve the confidence in the LES prediction. As a first step, an inflow generation method able to accurately produce desired turbulence statistics, while maintaining low computational cost, will be developed. Then, by accounting for uncertainties in the definition of the input parameters of the method, design values with upper and lower limits will be provided.

The computational cost of LES simulations can be prohibitive for wind engineering applications, especially during the early phases of design; for this reason, despite the turbulence model represents an important source of error, RANS simulations are still an attractive tool. In this regard, the second objective of this thesis is to improve the confidence in the RANS prediction of the mean pressure distribution around the building, by quantifying the combined effect of uncertainties in the inflow conditions and turbulence model. Furthermore, with the goal of improving the accuracy and reducing the uncertainty in the mean pressure prediction, a multi-fidelity framework will be established, by leveraging a limited number of LES simulations.

When designing cladding systems, we are ultimately interested in the peak pressure distribution on the building and the design pressure of the panels. Therefore, the third objective of the thesis is to extend the multi-fidelity framework to enable the calculation of the peak pressure from RANS simulations and a limited number of LES. Specifically, a data-driven model will be constructed to compute the root mean square (rms) pressure, from RANS variables. The mean and rms quantities could then be used to estimate the peak pressure distribution.

Finally, wind tunnel measurements will be used to validate the numerical frameworks and the results will be analyzed to improve our understanding of the physics that govern the pressure peaks phenomena. The following specific objectives are identified:

1. Wind tunnel experiments:
   (a) compare the data acquired in two different wind tunnels,
   (b) investigate the nature of the different pressure peaks phenomena,
   (c) validate the numerical frameworks.
2. LES framework:
   (a) establish an efficient and accurate inflow generation method to produce an incoming ABL with desired turbulence statistics,
   (b) study the sensitivity of the mean, rms and peak pressure distributions around the building and design pressure of glazed panels, to the input parameters of the inflow generation method.

3. RANS framework:
   (a) quantify the uncertainty in the mean pressure distribution around the building, caused by the inflow conditions and turbulence model.
4. Multi-fidelity framework:
   (a) improve the accuracy of the RANS prediction of the mean pressure distribution around the building,
   (b) construct a machine learning model to compute the rms pressure distribution around the building, from the RANS flow field.

1.3 Structure of the thesis

Figure 1.1 sketches the various components of the proposed numerical framework, which aims to support cladding design at all stages. These components are presented in the remainder of the thesis, as follows:

- Chapter 2 reviews the state of the art of wind tunnel experiments and CFD simulations for the task of estimating wind loads on high-rise buildings. In particular, the chapter analyzes recent developments in the fields of UQ and machine learning, to identify possible areas of progress in the field of cladding design.
- Chapter 3 introduces the test case selected for validation, i.e. a wind tunnel experiment on a high-rise building model. The same experiment was performed in two different ABL facilities; thus, the chapter presents the comparison of the ABL and pressure statistics resulting from the two tests. The effect of the incoming boundary layer on the mean, rms and peak pressure distributions and design pressure of glazed panels, is analyzed. Furthermore, the chapter investigates the nature of the pressure peaks phenomena that occur next to the corners and edges of high-rise buildings.
- Chapter 4 proposes a novel inflow generation framework for LES simulations of ABL flows; the framework combines a synthetic turbulence generator with an optimization procedure, which calibrates the input parameters of the turbulence generator until desired characteristics are obtained at the location of interest.
- Chapter 5 employs the inflow generation method proposed in Chapter 4, to perform LES simulations of the selected test case. The chapter investigates the effect of the inherent uncertainty in the definition of the inflow boundary conditions, on the mean, rms and peak pressure distributions around the building and design pressure of glazed panels.

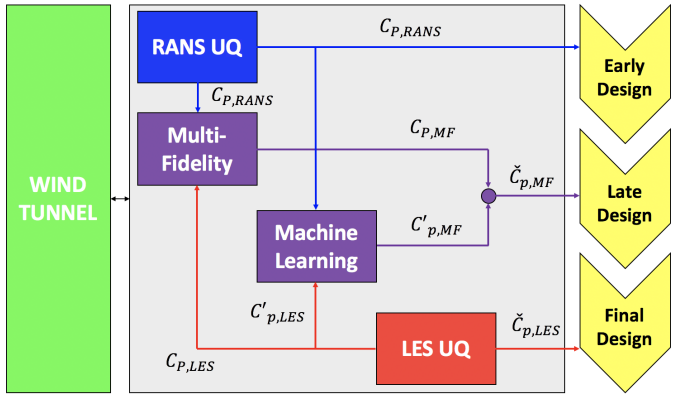

Figure 1.1: Structure of the proposed numerical framework, where $C_{P,RANS}$, $C_{P,MF}$ and $C_{P,LES}$ are the mean pressure coefficients outcome of the RANS, multi-fidelity and LES frameworks, respectively; similarly, $C'_{p,MF}$, $\check{C}_{p,MF}$, $C'_{p,LES}$ and $\check{C}_{p,LES}$ are the rms and peak pressure coefficients outcome of the multi-fidelity and LES methods.

- Chapter 6 presents the RANS UQ methodology to quantify the combined effect of inflow and turbulence model uncertainties on the mean pressure distribution on the building.
- Chapter 7 explores a multi-fidelity approach, that leverages a small number of LES simulations to improve the RANS prediction of the mean pressure around the building, and enable the computation of the rms pressure from the RANS flow field.
- Chapter 8 proposes a multi-fidelity machine learning framework to improve the accuracy in the prediction of the rms pressure, from RANS variables.
- Chapter 9 summarizes the contributions of the thesis and identifies possible areas of future research.

Chapter 2

State of the art

This chapter reviews the state of the art of the wind engineering practice to estimate wind loads on buildings and their components. Section 2.1 highlights the current established procedure for cladding design, consisting of wind tunnel experiments on reduced-scale models. Section 2.2 reviews the latest progress made in CFD simulations for wind loading applications. Recent developments in the fields of UQ and machine learning for CFD applications are also introduced, to identify possible areas of improvement for the wind loading practice.

2.1 Wind tunnel experiments

Nowadays, wind tunnel experiments are considered the most reliable method to estimate pressure loads on tall buildings and their components. Two methods are commonly adopted: the high frequency force balance (HFFB) and the synchronous multi-pressure sensing system (SMPSS). During a HFFB experiment the model of the building is placed on a force balance, that directly measures the global forces acting on the building [125, 15, 16]. During a SMPSS experiment instead, pressure time-series are recorded in several points on the building's surface by means of a synchronous multi-pressure sensing system (SMPSS) [117, 77, 41, 14, 16, 59, 47, 134]. The main advantage of the method is that details about the local pressure distribution can be obtained, differently from the HFFB experiments. Hence, the SMPSS method is the preferred solution when considering wind loads on components such as glazed panels, whose dimensioning is determined by the local pressure distribution. Nonetheless, the number of pressure taps that is used in routine SMPSS tests is insufficient to accurately estimate the area-averaged pressure on each cladding panel from integration of the local pressure distribution. Therefore, alternative methods have been developed to estimate the area-averaged pressure from limited measurement locations. A common approach is to assume a linear relationship between the duration and spatial extension of the pressure peak phenomena. Under this assumption, the pressure time-series can be filtered to remove extremely localized peak

events that are not relevant for cladding design [68, 21, 43]. However, the assumption of a linear relationship between the duration and the size of the peak events can introduce inaccuracies in the calculated design loads [4].

2.1.1 Pressure peaks

During cladding experiments it is not uncommon to observe strong negative peaks of pressure next to the corners and edges of the building. In these locations, the wind-induced pressure is indeed characterized by a strong non-Gaussian behavior [40, 116, 63, 101, 93, 19]. Importantly, peak events with different characteristics can be observed: some events are very localized in space and time, others have larger spatial and temporal extension. Some work has been done in the past to study the physical mechanism behind the latter kind of pressure peaks. In particular, the pressure measurements and flow visualizations conducted in [100], showed that the large negative peaks could be related to the roll-up of the separated shear layer. The wind tunnel tests performed in [116], indicated that the peaks could be related to vortex shedding; this seemed to hold also at higher turbulence intensities, at which the periodicity deteriorates and the vortex shedding occurs intermittently. The authors of [76] explained the occurrence of the large negative peaks with the mechanism of formation of the standing vortex at the upper corner of the side walls, and the inverted conical vortex at the lower corner. Nevertheless, these studies didn't observe nor consider the former type of suction events that can be experienced on high-rise buildings' facades, i.e. the extremely strong and localized pressure peaks. Conversely, very sharp and localized pressure peaks, up to 15 standard deviations from the mean value, were observed during the wind tunnel experiment carried out in [4]. The authors investigated the relationship between the duration and the spatial extent of the suction events; they concluded that the moving-average filter technique [68, 67], does not produce accurate results when considering high-rise buildings' lateral facades.

2.1.2 Extreme value analysis

An exhaustive literature review on the most used peak estimation methods was performed in [33]; the study, which included more than 150 journal and conference papers, identified 6 popular methods:

1. The single worst peak method [114] estimates the peak pressure as the most extreme value recorded during a sampling period.

2. In the ensemble average method [44] the pressure time-series is divided in equal-length segments, the most extreme value is extracted from each segment and the peak value is estimated as the average of the extreme values.

3. The Gumbel-fitting method [42] follows the same procedure of the ensemble average method to extract the extreme values from the time-series; then, a Gumbel distribution is fitted to the

extremes and the value corresponding to a certain fractile is output as peak value.

4. The Cook and Mayne method [20] is a variant of the Gumbel-fitting method, in which the parameters of the distribution are computed using 16 extremes, extracted from 10-60min segments in full-scale, and the chosen fractile is 78%. When 16 segments longer than 10min in full-scale are not available because of time constraints in the experiment, a correction should be applied on the parameters of the Gumbel distribution [21].

5. The translation methods [57, 101, 63] employ the full-time series to estimate the probability distribution of the peak, rather than using only the extreme values.

6. In the peak factor method [26, 27] the peak value is estimated as the sum of the mean value plus the standard deviation times a peak factor. According to [27], the peak response of most structures is within 3.5-4.5 standard deviations from the mean response.

Within the above methods, the Gumbel-fitting procedure is considered the most reliable one [93]; in particular, the Cook and Mayne method is the most popular choice. In [33] the uncertainty resulting from the Gumbel method was also investigated. The authors carried out a parametric study to quantify the effect of segments' length, number of segments and area-averaging, on the peak pressure estimate. The study concluded that to obtain accurate estimate of the peak pressure corresponding to 10min in full-scale, the minimum sampling duration is 30 minutes, i.e. 30 segments of length 1min. When considering peaks with large magnitude and area-averaged values, 15 peak values should be enough to accurately fit the Gumbel distribution.

The peak factor method for Gaussian processes [27] has been widely used in wind codes and standards [63], given its simplicity and shorter sampling duration requirement. Nonetheless, the method generally produces non-conservative estimates of the peak pressure in those regions of the building where the pressure signal is strongly non-Gaussian, i.e. next to the corners and edges. When the signal is close to Gaussian, such as away from corners and edges, or when filtered or area-averaged time-series are considered, the method leads to similar results to the Gumbel method.

2.2 CFD simulations

To estimate the design wind loads on tall buildings and their components, wind tunnel experiments are required by the building standards. CFD simulations are currently considered not enough trustworthy for such a delicate task. Nonetheless, important progress has been made in the past few decades to improve the accuracy and efficiency of the numerical simulations. This section summarizes the strengths, weaknesses and state of the art of the two most popular CFD models: LES and RANS.

2.2.1 LES

In LES, a low-pass filter is applied to the Navier-Stokes equations. As a result only the larger energy-containing scales of turbulence are resolved, while the smaller, more isotropic scales are modeled [95]. For incompressible turbulent flows, LES solves for the instantaneous resolved pressure and velocity fields, thus allowing direct estimate of the pressure peaks. The main drawback of LES simulations is the computational cost, which is often too high for practical wind engineering applications.

Inflow generation methods

The main challenge in LES of ABL flows is the definition of a turbulent inflow condition that accurately represents the surface layer in terms of mean velocity, turbulence intensities and turbulence length-scales. The methods to generate turbulent inflow conditions are generally classified in two categories: precursor methods and synthetic turbulence generators. Precursor or recycling methods employ either a separate simulation or a region upstream of the domain of interest to generate the turbulent inflow conditions [75, 85, 73, 120, 119, 24, 131]. These methods resolve upstream roughness elements in the simulations to generate a turbulent flow representative of an ABL. The computational cost of this approach presents a limitation for practical wind engineering applications. Moreover, the resulting boundary layer characteristics will depend on the chosen roughness configuration, providing only indirect control over the turbulence statistics. When the initial configuration does not provide the desired Reynolds stresses and integral length-scales, a time-consuming trial and error approach that involves modifying the roughness configuration and re-meshing the domain is required.

Synthetic turbulence generators represent an efficient alternative, providing full control over the turbulence statistics near the inflow boundary at a lower computational cost. They can be further classified as digital filter methods, random field generation (RFG) methods and synthetic eddy methods (SEM), which each have their strengths and weaknesses. Several variants of digital filter methods, which produce coherent structures in space and time by filtering a random velocity field, were specifically developed for ABL applications [132, 119, 60, 25, 24, 131]. Their main limitation is that they do not automatically generate a divergence-free velocity field; corrections need to be applied to avoid spurious pressure fluctuations in the domain [60]. The RFG methods generate a turbulent flow field that is guaranteed to be divergence-free, but their drawback is that the velocity field is characterized by Gaussian spectra and therefore not representative of an ABL [109, 24]. As a result, modifications to provide desired turbulence spectra and correlations are required [48, 1, 90]. The SEM methods, which produce velocity fluctuations based on the superposition of eddies [53, 52, 119, 66, 94, 131], also do not guarantee a divergence-free velocity field. Finally, an important shared limitation of all synthetic turbulence generators is that the generated turbulent velocity field is not a solution of the system of equations being solved. As a result, the specified inflow statistics will develop towards an equilibrium condition downstream of the inlet, and the final result will depend

on the subgrid model, the wall model and the discretization used. It is not uncommon to observe a strong decrease in the turbulence intensity between the inlet and the downstream location of interest [58, 54]. The problem is similar to the horizontal inhomogeneity observed in RANS simulations of the ABL [6, 87], but the solution is more involved because of the complex interaction between the wall model, the subgrid model and the numerics.

Single building simulations

Despite the challenges related to the inflow generation and the high computational cost, LES has gained in popularity in the wind engineering community over the last decade, especially for single building simulations [120, 124]. The importance of the inflow conditions has been clearly demonstrated on two benchmark test cases. In [11], 70 simulations and experiments of pressure coefficients on a rectangular cylinder were compared, while the authors of [123] reviewed LES and experiments on the high-rise CAARC (Commonwealth Advisory Aeronautical Council) building. In both cases significant discrepancies were observed between the different experimental and numerical results on the lateral facades, and it was suggested that differences in the inflow conditions could be responsible for these discrepancies. Several other studies also concluded that good agreement between LES and experimental results is strongly dependent on the accuracy of the specified inflow conditions [70, 24, 1, 91, 96].

Many studies focused on validating inflow generation methods against wind tunnel data. The authors of [24] performed LES on the CAARC building using three different inflow methods and demonstrated significant scatter in the predicted mean and root mean square pressure coefficients, in the separation region. In [49] LES simulations of a high-rise building were performed, using a synthetic turbulence generator; the authors considered 2 different velocity and turbulence intensity profiles, and showed that the specified mean velocity profile mainly influences the mean pressure on the building, while the prescribed turbulence intensity has a stronger effect on the pressure fluctuations. In [25] several LES simulations were performed, using a different synthetic turbulence generator and considering baseline and halved values for the turbulence intensity and integral length-scales; the authors concluded that the specified integral length-scales have a smaller effect on the mean and rms pressure coefficients on the building's surface, compared to the turbulence intensity.

2.2.2 RANS

The Reynolds-averaged Navier-Stokes equations are obtained by first decomposing the instantaneous physical quantities (i.e. pressure and velocity) in a mean and a fluctuating component, and then averaging the equations. The additional term resulting from this procedure, namely the divergence of the Reynolds stress tensor, requires additional modeling. The most common approach is to model the Reynolds stresses using the linear eddy-viscosity hypothesis [95].

Despite the inability of linear eddy-viscosity models to accurately predict inherently transient features of bluff body flows, such as stagnation, separation and reattachment, RANS simulations are widely employed in wind engineering applications given the low computational cost. However, the low fidelity of the results is limiting their application to qualitative analysis or to less critical tasks like modeling wind comfort, pollutant dispersion and natural ventilation [9, 115, 80, 8, 7]. Many wind engineering studies have focused on comparing the results of RANS simulations with different turbulence models. Some of these studies concluded that the revised $k-\epsilon$ models, such as the RNG $k-\epsilon$ model [113], provide more accurate results than the standard $k-\epsilon$ model in predicting the pressure distribution on tall buildings [126, 98, 74]. The wind-induced pressure acting on the CAARC building was computed in [23]; the results obtained with RANS simulations with the RNG $k-\epsilon$ turbulence model showed good accuracy on the windward facade, when compared to high-fidelity simulations and wind tunnel data; however, limitations in predicting the correct pressure distribution were experienced on the lateral facade of the building, where flow separation and reattachment occur. Similar conclusion were drawn in [82], where RANS simulations of the wind-induced pressure on a building with and without balconies, were performed. More recently, [81] presented a comparative study of RANS simulations with various turbulence and wall models for a super-tall building with circular cross-section. The study concluded that the accuracy of the pressure distribution on the building depends upon the correct identification of the flow separation and reattachment points.

UQ

The level of accuracy that can be achieved by RANS simulations, is inherently limited by the underlying linear-eddy viscosity assumption. Recently, research has focused on establishing methods to quantify the uncertainty introduced by RANS turbulence models [28]. A physics-based method that aims to quantify turbulence model uncertainty by perturbing the modeled Reynolds stress tensor has been proposed in [30]. The perturbations are based on the eigenvalue decomposition of the Reynolds stress tensor and can be introduced in the eigenvalues, eigenvectors and amplitude of the tensor. Perturbations of the eigenvalues in particular, aim to make the turbulence more $1-$, $2-$ and $3-$ dimensional; it can be shown that the $1-$ and $3-$ component limiting states correspond to maximum and minimum production of turbulence kinetic energy, respectively [37]. The method has been shown to provide realistic bounds on RANS flow predictions in a variety of configurations, such as channel and duct flows, wind engineering flows [36] and separated flows [50, 37]. Further development and validation of this method for wind loading applications would support its use to inform engineering design.

In addition to uncertainty due to the turbulence model, the definition of inflow boundary conditions that are representative of a neutral surface layer can pose a challenge. Several studies have indicated the need to ensure horizontal homogeneity of the velocity and turbulence profiles specified at the inflow by providing a consistent formulation between the inflow conditions, the wall function,

and the turbulence model [97, 124, 87]. However, even when the formulation is consistent, the inflow conditions of ABL flows can be highly variable, and therefore challenging to define exactly [102, 99]. Recent studies have addressed this challenge in predictions of urban canopy flow and dispersion, by employing methods that can propagate uncertainty in the definition of the inflow profiles to the quantities of interest (QoIs) [32, 111]. Specifically, a non-intrusive polynomial chaos expansion (PCE) [129] method was used to propagate the inflow uncertainty.

The inflow boundary condition is a source of aleatory uncertainty, inherent to the problem, while the uncertainty introduced by the turbulence model is an epistemic uncertainty, related to model assumptions and missing physics. To propagate the combined effect of aleatory and epistemic uncertainties to the QoIs, different methods have been formulated [118]. For example, the second-order probability framework employs an inner and an outer loop: the inner loop quantifies the effect of aleatory uncertainties, while the outer loop specifies the epistemic uncertain variables. As a result, each set of epistemic variables will produce a probability distribution for the QoIs [118].

Recently, to improve the accuracy of RANS simulations and reduce the uncertainty in their results, multi-fidelity frameworks for UQ have been developed [92]. These combine the results of many low-fidelity simulations, i.e. RANS, to the outcome of few high-fidelity simulations, LES for instance. The multi-fidelity method developed in [83], employs PCE and stochastic collocation to construct stochastic models for both the low-fidelity model and the discrepancy function between low- and high-fidelity models. Even though the surrogate model of the discrepancy function is constructed using a coarser grid of input realizations than the low-fidelity model, the combination of the two can often achieve high-fidelity performance in the finer grid. Another popular strategy is to employ a hierarchy of models with different fidelity levels, knows as multi-level method [34]; for example one could use simulations with increasing grid resolution as models with increasing level of fidelity. Both the multi-fidelity and multi-level strategies were employed in [55] to quantify the uncertainty in simulations of irradiated particle-laden turbulence. The authors attributed the better performance of the multi-fidelity framework to the good correlation between high- and low-fidelity models.

Pressure fluctuations

Even if RANS simulations could provide accurate predictions of the mean pressure distribution on the building, additional models will be necessary to retrieve an estimate of the pressure peaks that define the design loads. One option is to generate artificial pressure fluctuations from the RANS averaged quantities, by performing an additional simulation that solves the Poisson equation for the pressure fluctuations [69, 46]. A simpler and cheaper approach is to employ empirical relationships that provide the root mean square pressure as a function of the local mean pressure, turbulent kinetic energy and inlet velocity [88, 105, 89, 97]. Nevertheless, these empirical models were formulated

using wind tunnel data acquired for low-rise buildings. Not only were the geometries not representative of high-rise building designs, but the measurements were also limited to a small number of locations around the building. As a result, none of these relationships produces accurate results when considering the lateral facades of high-rise buildings [56].

Machine learning

As an alternative to standard empirical models, one could explore data-driven procedures that aim to find a functional form that can accurately represent available data. Recently, several studies have successfully used machine learning to relate RANS time-averaged quantities to high-fidelity data [28, 12]. In [72], the authors computed 20 physical quantities from RANS variables, and used these as features in a machine learning procedure to estimate regions of high uncertainty in RANS simulations. Specifically, the features were pre-processed to be made Galilean invariant, which is essential to add physical meaning to the machine learning prediction. In [71] a methodology to obtain invariant features was developed; the procedure was then applied to learn the turbulent diffusivity in film cooling flows [78]. The same authors attempted to provide an interpretation to their machine learning model by analyzing the importance of each feature in making the prediction [79]. In [45], various machine learning models were trained to predict the mean and rms pressure coefficients around circular cylinders, as a function of the Reynolds number, turbulence intensity and cylinder diameter.

When the problem under consideration is high-dimensional, as often the case in machine learning applications, dimension reduction techniques can be useful to visualize the data and reduce the computational cost of the procedure. A popular approach in fluid-dynamics is principal component analysis (PCA), also know as proper orthogonal decomposition (POD) [12, 107]. Similarly, active subspace methods [17] have been recently employed to reduce the dimensionality of several CFD problems [18, 106, 122].

2.3 Summary

Despite the great progress that has been made in the past few decades to improve the trade-off between accuracy and computational cost of the numerical simulations, CFD is still considered not reliable enough for critical wind loading problems.

Within the CFD models, LES certainly represents the most likely candidate for near future employment in the design process. Nonetheless, the inflow generation problem is still an active area of research. In this regard, synthetic turbulence generators seem the most natural and efficient choice to produce incoming ABLs with desired characteristics. However the problem of turbulence decay needs to be addressed, while maintaining the computational cost reasonable for design. Furthermore, no matter what inflow generation method is used, the ABL to be modelled is inherently uncertain;

thus, a systematic way of accounting for the effect of this uncertainty on the design QoIs is needed.

On the other hand, RANS simulations, despite their limitations, may still represent a useful tool, given the low computational cost. Innovative methods such as uncertainty quantification and machine learning could support the use of RANS for wind loading applications, especially during the early phases of design. A UQ procedure that quantifies the combined effect of inflow and turbulence models uncertainties may increase the confidence in the RANS prediction. Furthermore, multi-fidelity methods could be employed to reduce the uncertainty in the RANS result and further improve the accuracy of the prediction. Finally. machine learning has the potential to fill the gap between the fact that RANS can only provide mean quantities and the need of peak values for design.

Chapter 3

Wind Tunnel experiments

This chapter presents the test case selected for validation of the numerical framework, namely a wind tunnel experiment on a high-rise building model. The experiment was originally performed in the ABL wind tunnel of Politecnico di Milano (PoliMi). It focused on measuring the pressure distribution in the most critical regions on a high-rise building facade, i.e. adjacent to the corners and edges of the side walls, for an open-terrain exposure and different inflow directions.

The same high-rise building model was then tested at the Wall of Wind (WoW) facility of Florida International University. The objective of this second round of tests was to verify the conclusions observed at PoliMi. Hence, the tests were performed using a similar open-terrain exposure, considering a subset of critical inflow directions identified at PoliMi [4, 64]. To promote the dissemination of the data as a benchmark test case for the determination of wind loading on high-rise buildings, the PoliMi dataset is available to the scientific community on the open-access repository Zenodo [86], while the WoW dataset is available on the Stanford digital repository (SDR, [104]).

In the remaining of the chapter, we first discuss the experimental set-up in both wind tunnels. Then, we present the comparison of the results. To verify the consistency of the two incoming ABLs, we compare the profiles of mean velocity, turbulence intensity, integral time-scales and spectra. The wind pressure measurements are first compared in terms of the mean, root mean square and spectra of the pressure coefficients. Subsequently, the frequency and intensity of the pressure peaks is analyzed; to interpret these results, visualization of the spatial and temporal extent of individual peak events and of their effect on the area-averaged pressure on a cladding element, is performed. Finally, extreme value analysis is used to compute the peak pressure coefficient on individual taps and the design pressure coefficient of glazed panels.

3.1 Experimental setup

The PoliMi facility is a closed-circuit wind tunnel; the boundary layer test section has a cross section of 14×4 m^2 and is 35m long. The models are placed at a distance of 10m from the inlet, in the center of a turntable of radius 6.5m, to enable tests at different wind directions. The WoW ABL facility is an open-circuit wind tunnel with a 6.1m wide and 4.3m high test section and a turntable with a radius of 4.9m. In the following, we first describe the set-up of the velocity measurements, performed at the center of the turntable in absence of the model to characterize the ABL in both wind tunnels. Subsequently we introduce the set-up for the pressure measurements on the high-rise building.

3.1.1 Velocity measurements

In the PoliMi wind tunnel, a detailed characterization of the ABL was carried out using 3D hot-wires with a sampling frequency of 2000Hz. The velocity components were measured at 280 points distributed on a plane at the building location, as shown in Figure 3.1. The outcome of the experiment consists of 20s time-series of the three velocity components at 5 spanwise locations (0.6m apart) and 56 vertical locations (43.7mm apart below 0.75m and 87.5mm apart above).

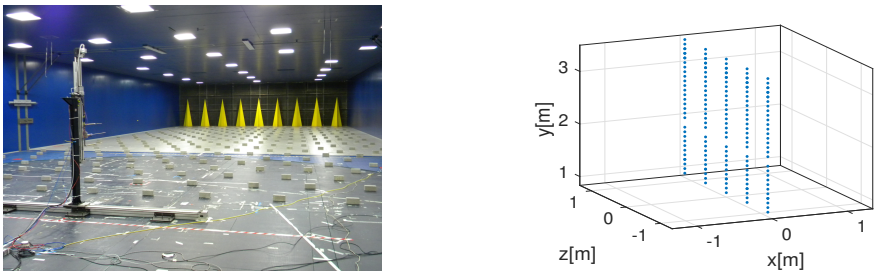

(a) Setup of the experiment to characterize the ABL at PoliMi

(b) Coordinates of the hot-wire measurements

Figure 3.1: PoliMi experimental setup of velocity measurements.

The ABL in the WoW was characterized using TFI Cobra probes with a sampling frequency of 2500Hz; 60s time-series of the three components of velocity were recorded at 6 vertical locations in the center of the turntable. The spatial resolution of these measurements varied between 0.3m and 0.6m. Table 3.1 summarizes the parameters of the two experiments in terms of sampling frequency, total duration and reference velocity at roof height. The WoW tests were run at a higher reference velocity than the PoliMi tests; the comparisons in section 3.3.1 will be presented in terms of non-dimensional quantities.

	$f_{samp}[Hz]$	$T[s]$	$U_{ref}[m/s]$
PoliMi	2000	20	7.8
WoW	2500	60	35.4

Table 3.1: Sampling frequency, total duration and reference velocity at roof height for the velocity measurements performed in both facilities.

3.1.2 Pressure measurements

Building model

The same high-rise building model was used in both experimental facilities. It is a 1m wide, 0.3m deep and 2m high rectangular box, representative of a 100m tall building in full-scale. The model was placed at the center of a turntable to allow testing at different inflow directions (Figure 3.2). Using the symmetry of the model, the wind tunnel data obtained for the 180° exposure will be used for a more complete validation of the pressure distribution at 0°. Therefore, the combination of these two wind directions will be referred to as the 0° wind direction for the remaining of the thesis.

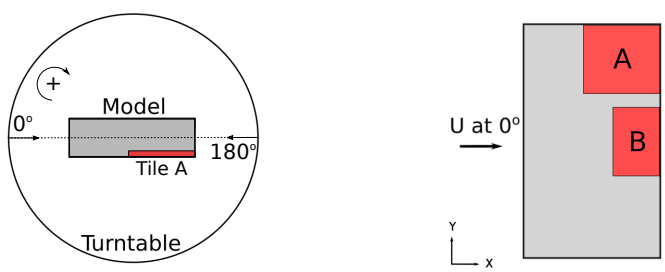

(a) Top view of the turntable, indicating the convention used for the wind direction

(b) Side view of the building model

Figure 3.2: Sketch of the building model.

The experiment was designed to enable a detailed study of the pressure distribution in the regions of the building where the highest pressure peaks are expected, i.e. near the corners and edges of the building [4]. Therefore, two aluminum tiles containing 224 and 223 pressure taps respectively, were designed: tile A located on the top-corner of the model and tile B centered at 1m height adjacent to the building edge (Figure 3.2). The minimum tap distance is 3.4mm on both tiles; the resolution is progressively decreased when moving away from the building edges. The pressure taps have an internal diameter of 1.3mm; they are connected to the pressure scanner system through rubber tubes with the same diameter to avoid discontinuities. Figure 3.3 shows the distribution of the pressure taps on tile A, together with the set-up of the experiment in the two wind tunnel facilities. The tubing system introduces distortion in the pressure signal; the raw pressure measurements are divided by the tubing frequency response function to account for this distortion and reconstruct the original pressure signal before post-processing.

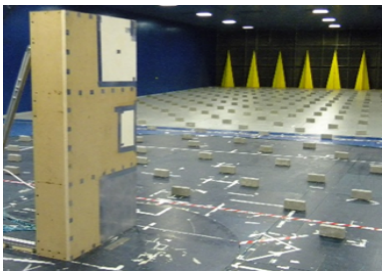

(a) PoliMi test section

(b) WoW test section

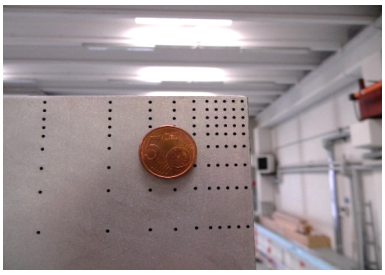

(c) pressure tap distribution on tile A

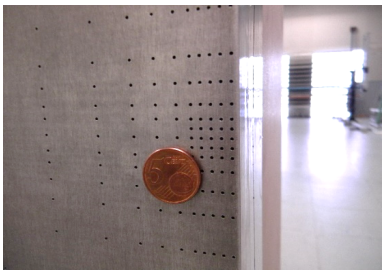

(d) pressure tap distribution on tile B

Figure 3.3: Pictures of the test sections of both wind tunnels and close-up of the aluminum tiles.

Pressure Measurement System

At PoliMi, the model was instrumented with 7 PSI ESP-32 HD high-speed pressure scanners, connected to a data acquisition system with a sampling frequency of 500Hz. The outcome of each test consists of 300s time-series of pressure measured at 446 taps. The reference velocity of $\sim$ 11.8m/s at 2m height was measured during each test by a Pitot tube located 7m upwind of the building. The reference pressure was computed by pneumatically averaging the pressure recorded at 4 different points across the test section, during each test.

The WoW measurements were performed using pressure scanners with a sampling rate of 520Hz. As in the PoliMi wind tunnel, 300s time-series of pressure were recorded at 446 taps. The tests were performed at the same Reynolds number, i.e. with a target reference velocity of 11.8m/s at 2m height. At the beginning of the experiment, TFI Cobra probes were employed to measure the velocity at two vertical locations at a lateral distance of 2m from the building. Since the facility is an open-circuit wind tunnel, the reference pressure was determined from the nearest weather station. The details of both experiments are summarized in Table 3.2.

	$f_{samp}[Hz]$	$T[s]$	$U[m/s]$
PoliMi	500	300	11.7
WoW	520	300	11.0

Table 3.2: Sampling frequency, total duration and reference velocity at roof height for the pressure measurements performed in both facilities.

3.2 Quantities of interest

Throughout the thesis, the pressure values will be always presented as non-dimensional pressure coefficients defined as

$$C_p(t) = \frac{p(t) - p_{ref}}{\frac{1}{2}\rho U^2} \tag{3.1}$$

where p is the instantaneous pressure, p_{ref} the reference pressure, ρ the density of the air and U the reference velocity at roof height. The mean, rms and peak pressure coefficients are given by:

$$C_P = \frac{P}{\frac{1}{2}\rho U^2}, \qquad C'_p = \frac{\sqrt{\overline{p'^2}}}{\frac{1}{2}\rho U^2}, \qquad \check{C}_p = \frac{\check{p}}{\frac{1}{2}\rho U^2} \tag{3.2}$$

where P and p' represent the mean and fluctuating pressures, respectively, and $\check{p}$ is the peak pressure calculated using one of the methods highlighted in Section 2.1.2. In this chapter and in Chapter 5, the Cook and Mayne method [21] is employed and the peak values relative to a 22% probability of exceedance are reported.

From an engineering design point-of-view, surface pressure measurements are usually performed to assess the load on cladding elements and their supporting structure. The relevance of the peak phenomena is therefore determined by their effect on the area-averaged pressure acting on the panels. By exploiting the high density of pressure taps used in the experiments, we can compute the area-averaged pressure acting on a cladding element by direct numerical integration:

$$p_{AA}(t) = \frac{\sum C_{p,i}(t) A_i}{\sum A_i} \tag{3.3}$$

where p_{AA} is the area-averaged pressure on the panel, p_i is the pressure recorded by the i-th tap, A_i is the tributary area of the i-th tap. By applying the extreme values analysis to the area-averaged pressure coefficient, the design pressure coefficient of the panels $\check{C}_{p,d}$ can be computed.

3.3 Results

In this section, we first compare the velocity statistics of the incoming boundary layers generated in the two wind tunnels in terms of the mean velocity, turbulence intensities, integral time-scales and velocity spectra. Subsequently, we present the comparison of the pressure measurements both in terms of statistics, i.e. mean, root mean square and spectra, and in terms of time-series and peak events.

3.3.1 Velocity statistics

In the following plots, the gray error-bars represent the variation of the velocity statistics measured at the different spanwise locations in the PoliMi wind tunnel, and the gray circles indicate the corresponding spanwise-averaged values; the red dots represent the data measured at WoW.

Figure 3.4 shows the profiles of mean streamwise velocity, nondimensionalized by the reference velocity at roof height. The profiles are shown both in linear and logarithmic scale. The WoW measurements are within the spanwise variation of PoliMi data at all available measurement heights. When plotted in logarithmic scale, the velocity profiles manifest the expected linear trend of a neutral ABL. By fitting regression lines to the data, we obtain a roughness length of $\sim$ 3mm and $\sim$ 2.5mm for the PoliMi and WoW tests respectively.

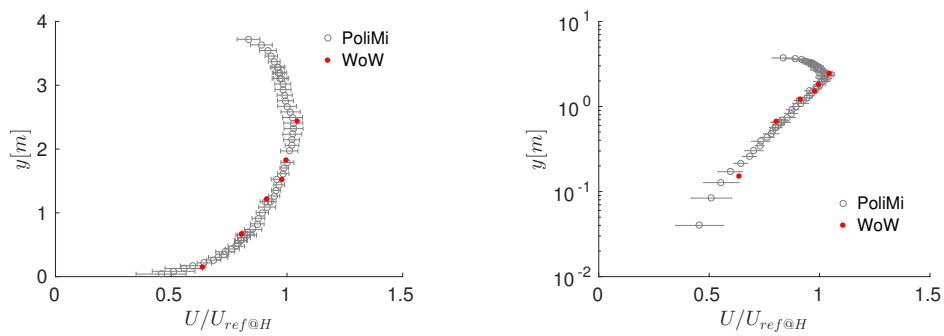

(a) linear-scale (b) log-scale

Figure 3.4: Comparison of nondimensional mean velocity between PoliMi and WoW data.

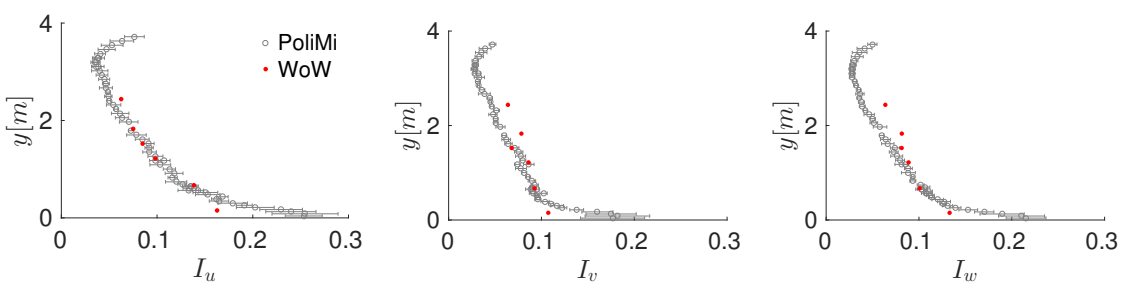

(a) streamwise turbulence intensity (b) vertical turbulence intensity (c) spanwise turbulence intensity

Figure 3.5: Comparison of turbulence intensities between PoliMi and WoW data.

The turbulence intensities, defined as the ratio of the root mean square and the mean velocity, are compared in Figure 3.5. The streamwise turbulence intensity measured at WoW is within the interval defined by the spanwise variation in the PoliMi experiments, except for the lowest and highest points. The highest discrepancy occurs close to the ground where the turbulence intensity

in WoW is ~ 0.07 lower than the PoliMi spanwise-averaged value. The WoW profiles of vertical turbulence intensity are ~ 0.06 lower close to the ground and ~ 0.02 higher above 1.8m. Similarly, the spanwise turbulence intensity computed from WoW data at 0.15m height is ~ 0.045 lower than PoliMi spanwise-averaged value at the same height and above 1.5m it is $\sim 0.02 - 0.03$ higher.

Figure 3.6 shows the comparison in terms of non dimensional integral time-scales; the profiles are nondimensionalized using the reference velocity at roof height and the height of the building. All three components show reasonable agreement, considering that a significant spanwise variation is observed in the PoliMi experiment. The main discrepancy between the two datasets again appears close to the ground in the vertical and spanwise profiles.

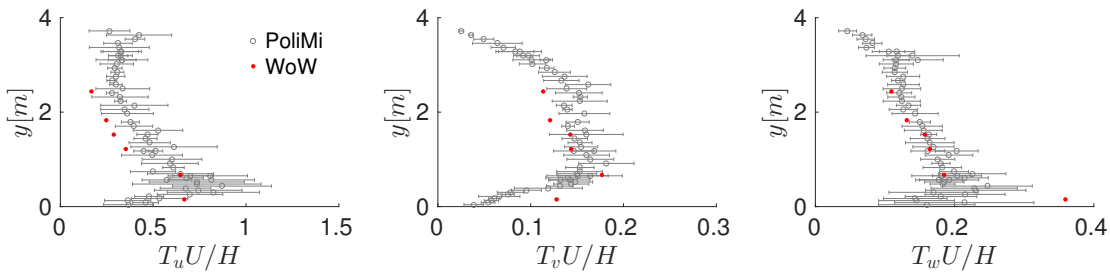

(a) streamwise time-scale (b) vertical time-scale (c) spanwise time-scale

Figure 3.6: Comparison of nondimensional integral time-scales between PoliMi and WoW data.

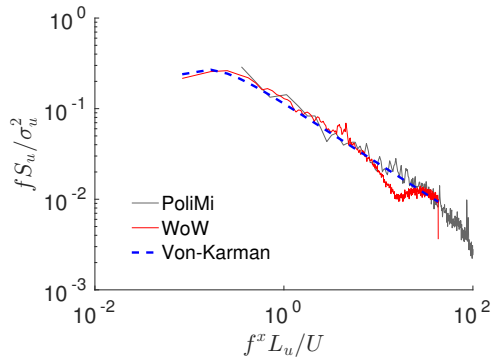

Figure 3.7: Comparison of streamwise velocity spectra between PoliMi and WoW data at 0.67m height, compared to the Von-Karman spectrum adapted for wind engineering [38].

Finally, the power spectra of the streamwise velocity component are compared to the standard Von-Karman spectrum in Figure 3.7. The three profiles agree well throughout the range of nondimensional frequencies that the two experiments have in common. The longer time-series measured in the WoW test allow to capture larger scales compared to the PoliMi experiment; this is evident from the lower frequencies in the spectrum computed from the WoW data. Conversely, even though the sampling frequency of the cobra probes is higher than the sampling frequency of the hot-wires,

the spectrum measured at PoliMi contains higher nondimensional frequencies compared to WoW data. This is a result of the fact that the Reynolds number of the WoW experiment is almost 5 times larger than the Reynolds number of the PoliMi test; therefore, the sampling frequency of 2500Hz does not enable the measurement of scales as small as in the PoliMi wind tunnel.

The comparison of the velocity statistics indicates that the PoliMi and WoW experimental set-ups have very similar incoming ABLs, both in terms of the time-averaged velocity and the turbulence quantities.

3.3.2 Pressure statistics

In this section, we first compare the pressure statistics measured in the two wind tunnels, for two configurations: 0° and 20° wind directions. Subsequently, we present the comparison of the time-series and peak values for the 20° wind direction, which produced the strongest suction peaks [4].

0° wind direction

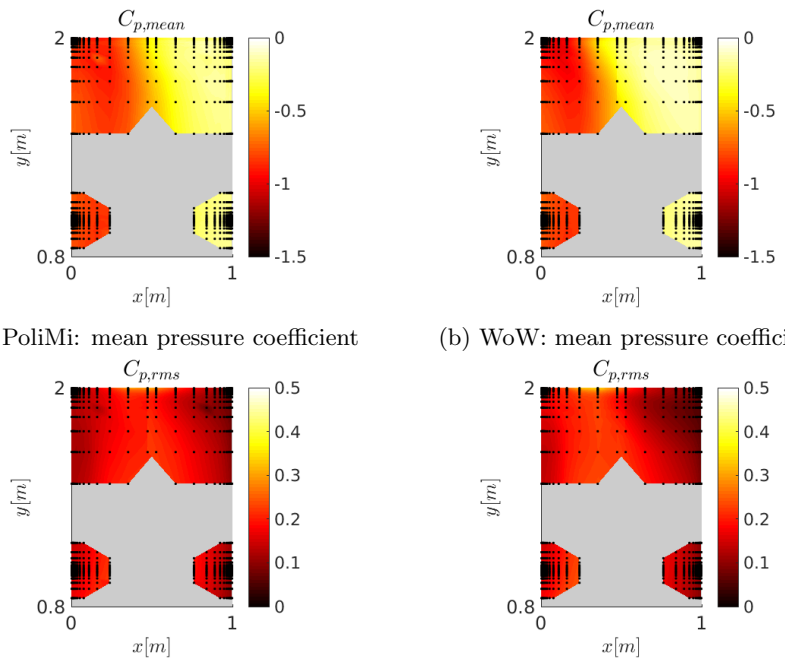

(a) PoliMi: mean pressure coefficient

(b) WoW: mean pressure coefficient

(c) PoliMi: rms pressure coefficient

(d) WoW: rms pressure coefficient

Figure 3.8: Comparison of pressure coefficient first and second order statistics at 0°. Once again, tiles on the right and on the left of each subplot refer to 0° and 180° wind directions respectively.

Figure 3.8 shows the distribution of the pressure coefficient statistics on the building's lateral facade at 0° wind direction. The mean pressure coefficients recorded in both wind tunnels agree well

qualitatively: the flow first separates at the windward edge generating an area of relatively strong negative pressure coefficient (red region in Figures 3.8a and 3.8b), then it reattaches in the rear part of the model (yellow region in Figures 3.8a and 3.8b). From the contour plot it appears that the WoW data experiences a slightly stronger negative pressure coefficient, especially in the separation region. The distribution of the rms pressure coefficient is shown in Figures 3.8c and 3.8d. Both sets of measurements show high fluctuations in the region of flow separation and reattachment; the rms C_p computed at WoW is slightly higher than the PoliMi one, especially in the separation region.

Figure 3.9 provides a more quantitative comparison, showing the statistics of the pressure coefficient along two rows of taps on tiles A and B respectively. The highest discrepancy is experienced in the top part of the model (tile A) in the reattachment region. The maximum difference in the time-averaged pressure coefficient along the row of taps at 1.76m height, is ~ 0.19 (Figure 3.9b); the maximum difference in rms C_p is ~ 0.04 (Figure 3.9c). Along the row of taps at 1m (Figures 3.9f), the agreement between the two data-sets is rather good in both upwind and downwind locations. The maximum discrepancy in time-averaged and rms coefficients is ~ 0.05 and ~ 0.02 respectively.

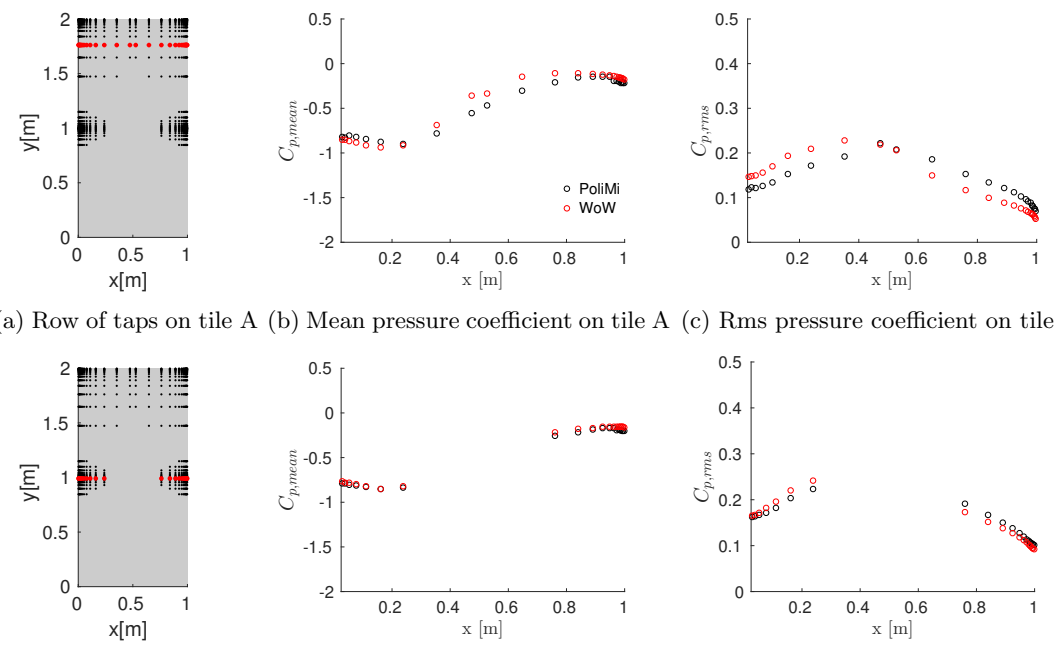

(a) Row of taps on tile A (b) Mean pressure coefficient on tile A (c) Rms pressure coefficient on tile A

(d) Row of taps on tile B (e) Mean pressure coefficient on tile B (f) Rms pressure coefficient on tile B

Figure 3.9: Comparison of mean and rms pressure coefficients at 0° wind direction.

The difference between the two experiments could partially be explained by looking at the characteristics of the incoming boundary layers. While the mean velocity profiles agree well (Figure 3.4), the profiles of turbulence intensity manifest some discrepancies above 1.7m (Figure 3.5). The higher turbulence intensities generated at WoW could result in higher pressure fluctuations in the

separation region, compared to the PoliMi experiment [100]. Furthermore, the higher turbulence intensities in the WoW experiment could cause the reattachment point of the flow to move upstream, resulting in faster recovery and lower absolute values of mean and fluctuating C_p in the rear portion of the model [100, 42].

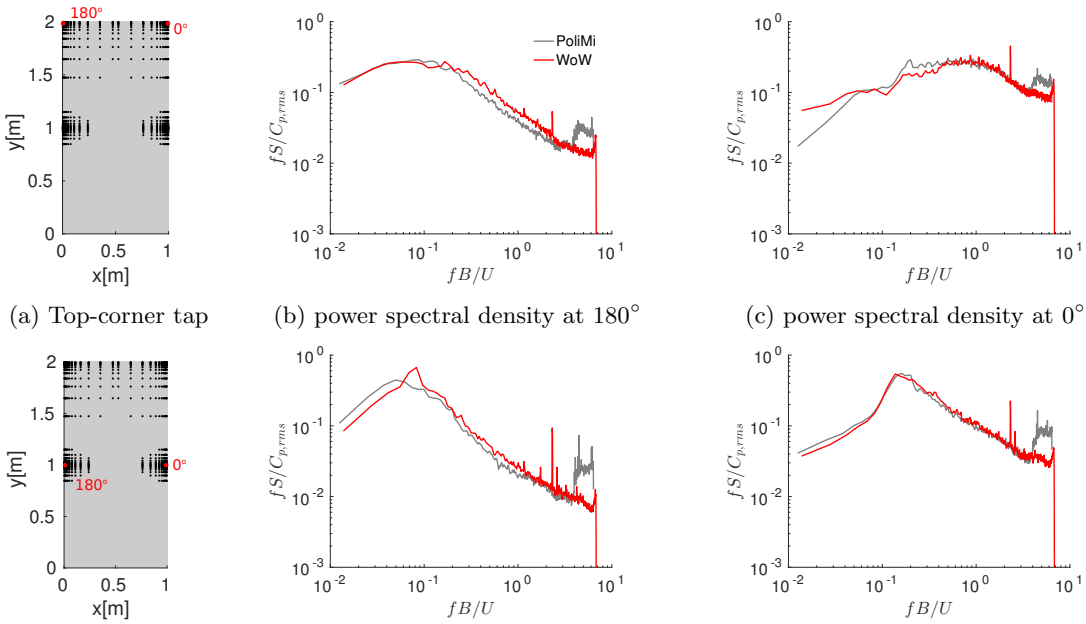

(a) Top-corner tap (b) power spectral density at 180° (c) power spectral density at 0°

(d) Mid-edge tap (e) power spectral density at 180° (f) power spectral density at 0°

Figure 3.10: Non-dimensional power spectral density of the pressure coefficient at 0° wind direction on top-corner and mid-edge taps.

In Figure 3.10 we plot the power spectral density of the pressure coefficient measured in the same tap at 0° and 180° wind directions (marked by the red dots). The power spectra are adimensionalized using the frequency; the adimensional frequency is computed using the reference velocity at roof height and the width of the model (B). The comparison between the two experiments shows good agreement at most frequencies. Considering the top-corner tap (tile A), the only significant deviation appears at 0° at low frequencies, where WoW data reaches higher energy-content compared to PoliMi ones. Focusing on the pressure tap at 1m height (tile B), we can see that in both experiments the highest energy content occurs around $\frac{fB}{U} \sim 0.15$ and 0.08, when the tap is located either in the separation region (Figure 3.10e) or in the rear portion of the model (Figure 3.10f), respectively. The more local peaks observed at very high-frequencies are likely due to experimental noise.

20° wind direction

Figure 3.11 shows the distribution of the mean and rms pressure coefficients on the building's lateral facade at 20° wind direction. In this configuration both tiles are located in the wake of the building

and experience relatively strong suction and pressure fluctuations. The mean pressure coefficient measured at WoW appears slightly less strong than the PoliMi one (Figures 3.19a and 3.19b), while no significant differences in rms C_p are evident from Figures 3.11c and 3.11d.

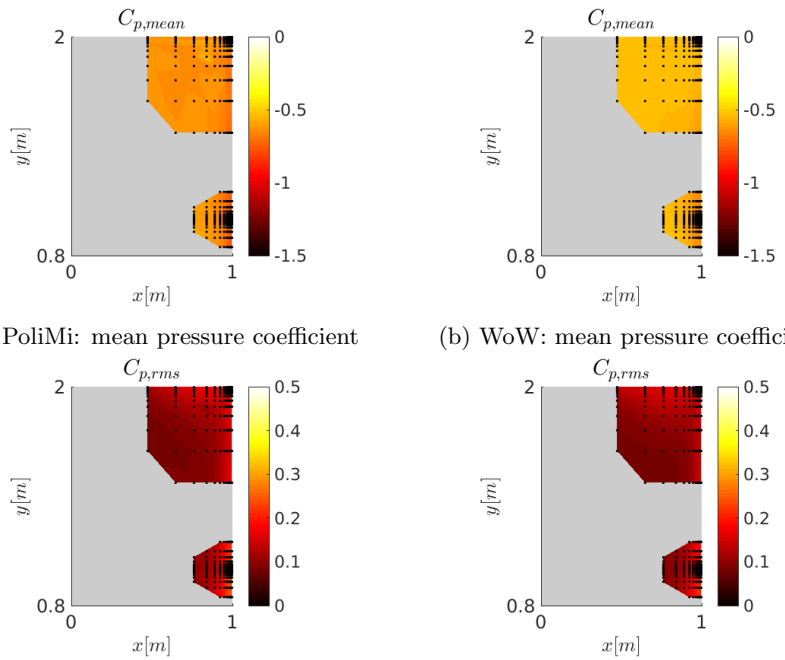

(a) PoliMi: mean pressure coefficient

(b) WoW: mean pressure coefficient

(c) PoliMi: rms pressure coefficient

(d) WoW: rms pressure coefficient

Figure 3.11: Comparison of mean and rms pressure coefficients at 20° wind direction.

A quantitative comparison is again presented by considering two rows of taps along the building's lateral facade (Figure 3.12). The maximum discrepancy between the two data-sets along the row of taps selected on tile A is ~ 0.15 and ~ 0.02, for first and second order statistics respectively (Figures 3.12b and 3.12c); focusing on tile B, the difference in the mean and rms C_p is ~ 0.13 and ~ 0.03 respectively (Figures 3.12b and 3.12c). As for the 0° wind directions, these discrepancies could be caused by the differences in the boundary layer turbulence intensities.

Figure 3.13 shows the power spectral density of the pressure coefficient measured in two taps (marked by the red dots) at 20° wind direction. The agreement between the two data-sets over the range of frequencies considered is good. When considering the pressure tap at 1m height, both experiments exhibit the highest energy content around $\frac{fB}{U} \sim 0.05$.

3.3.3 Pressure peaks

The comparison in terms of pressure peaks focuses only on the 20° case, since this represents the most interesting and critical situation for the locations of interest [4]. We first compare the frequency

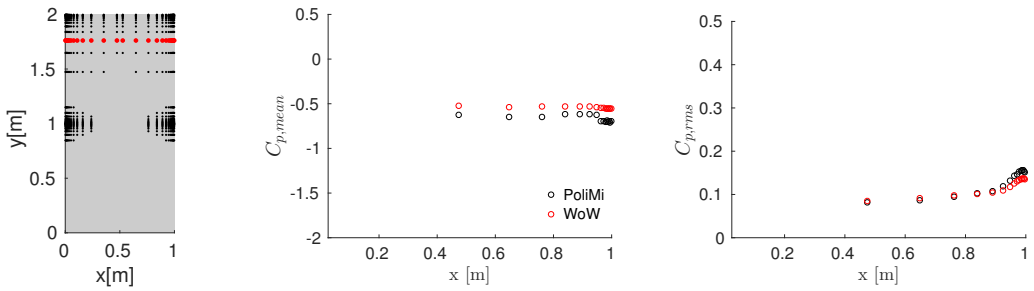

(a) Row of taps on tile A (b) Mean pressure coefficient on tile A (c) Rms pressure coefficient on tile A

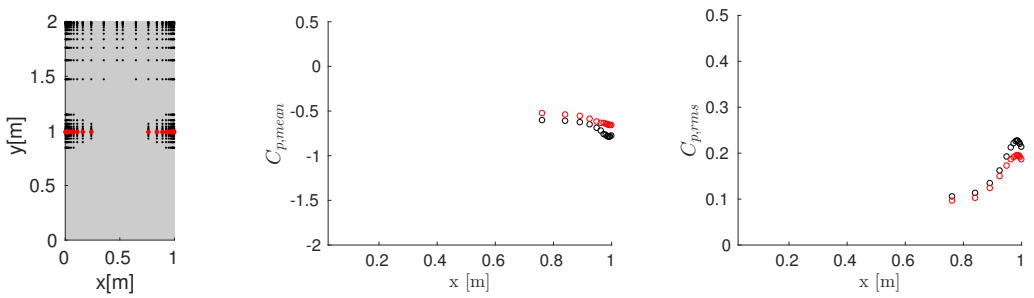

(d) Row of taps on tile A (e) Mean pressure coefficient on tile B (f) Rms pressure coefficient on tile B

Figure 3.12: Comparison of pressure coefficient first and second order statistics at 20° wind direction.

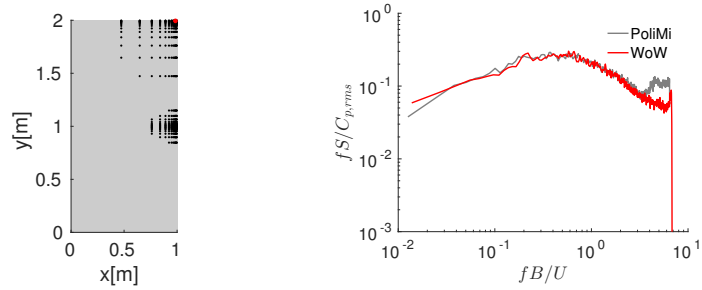

(a) Top-corner tap (b) power spectral density at 20°

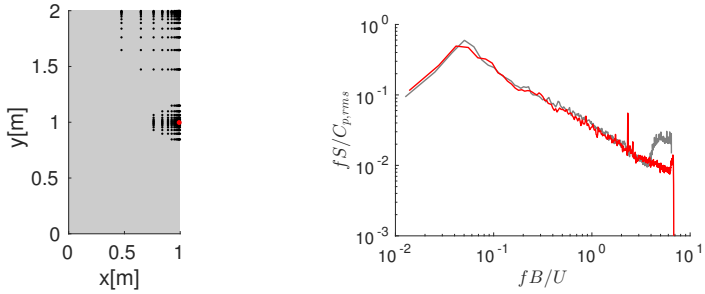

(c) Mid-edge tap (d) power spectral density at 20°

Figure 3.13: Non-dimensional power spectral density of the pressure coefficient at 20° wind direction on top-corner and mid-edge taps.

and strength of the local suction events observed during the two experiments by considering the time-series and the probability distributions of the pressure coefficient measured at an individual pressure tap. Subsequently, we present the probability distributions of the area-averaged pressure coefficient, considering a typical cladding panel of $2 \times 3\text{m}^2$. To support the interpretation of the results, snapshots of the pressure time-series surrounding two different negative peak events are visualized.

In Figure 3.14 we show the time-series of the pressure coefficients recorded on a pressure tap adjacent to the corner of tile A, at 20° wind direction.

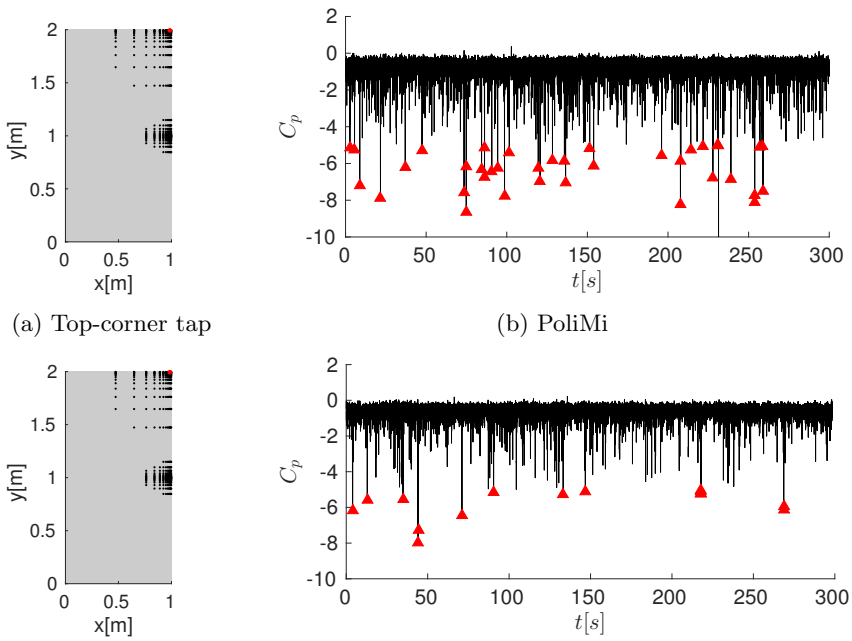

(a) Top-corner tap (b) PoliMi

(c) Top-corner tap (d) WoW

Figure 3.14: Time-series of pressure coefficient at 20° wind direction on top-corner tap. The red arrows indicate the negative peaks lower than $C_p = -5$

During the 300s period of the experiments, multiple negative peaks occur in both tests: 38 and 15 peaks stronger than $C_p = -5$ appear in the PoliMi and WoW time-series respectively (red arrows in Figure 3.14). The largest negative pressure coefficient recorded at PoliMi is ~ -10, while at WoW it is ~ -8. Qualitatively, the time-series exhibit very similar behavior, but the negative peak values measured at PoliMi are slightly stronger and more frequent than the WoW ones. Figure 3.15 shows the probability density functions (PDFs) of the pressure coefficients in both experiments on the same top-corner tap, and on a mid-edge tap on Tile B. The PDFs are shown both in linear and logarithmic scale. A similar non-Gaussian behavior is found: the distributions are significantly skewed to the left as a result of the negative pressure coefficient peaks. The plot in logarithmic

scale highlights this asymmetry, with the left tail of the PDFs following a nearly linear trend. The effect is more pronounced on tile A than tile B; specifically the skewness of the PDFs on the top-corner tap is ~ -4.27 and ~ -4.35 for PoliMi and WoW data respectively (Figure 3.15b), while the corresponding values of skewness on the mid-edge tap are ~ -0.65 and ~ -0.69 (Figure 3.15e).

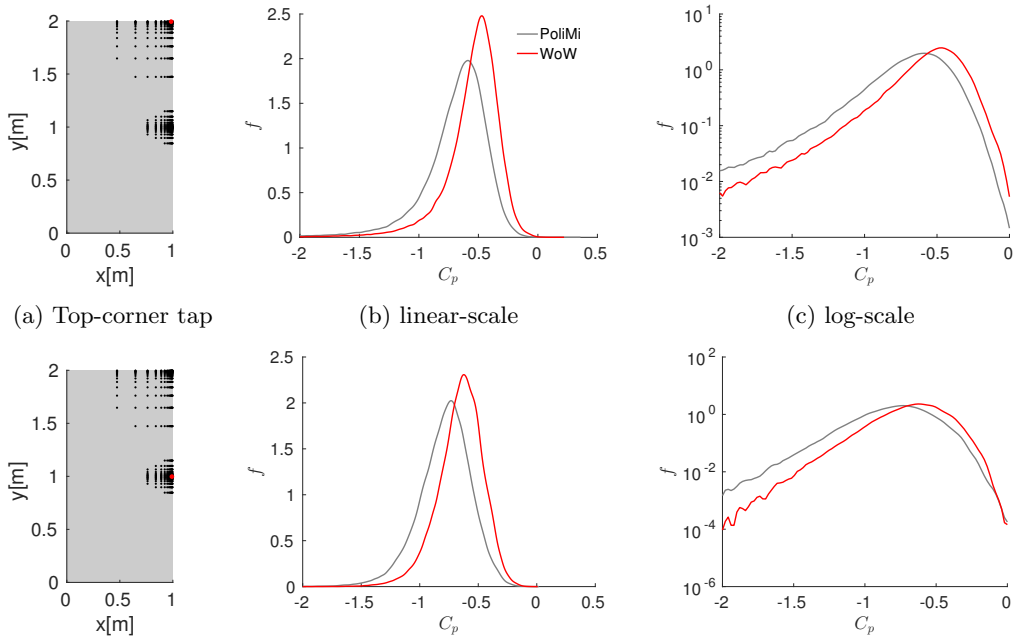

(a) Top-corner tap (b) linear-scale (c) log-scale

(d) Mid-edge tap (e) linear-scale (f) log-scale

Figure 3.15: Probability density functions of pressure coefficient at 20° wind direction.

Figure 3.16 shows the PDFs of the pressure coefficient averaged over a $2 \times 3\text{m}^2$ cladding panel, highlighted in red in Figures 3.16a and 3.16d. The averaging operation filters out the most negative pressure coefficient peaks; as a result the PDFs manifest a less pronounced non-Gaussian behavior. The skewness of the PDFs on the top-corner panel is now reduced to ~ -1.11 and ~ -1.33 for PoliMi and WoW data respectively (Figure 3.16b), while the ones on the mid-edge panel are ~ -0.57 and ~ -0.58 (Figure 3.16e).

The high spatial resolution of the pressure taps enables further analysis of the spatial characteristics of the peak events to interpret the difference between the pdfs of the local and area-averaged pressure coefficients. Figure 3.17 depicts short time intervals around the occurrence of the peaks on the top-corner tap (Figures 3.17b and 3.17e) and the corresponding spatial distribution of the pressure coefficient at the time instants marked by the red arrows (Figures 3.17c and 3.17f). In addition, the pressure coefficient averaged over a $2 \times 3\text{m}^2$ panel (sketched in Figure 3.17c), is plotted during the same time period. In both experiments, extremely concentrated peak events, both in time and space, are recorded in the same location, for the same wind direction. This type of events, which

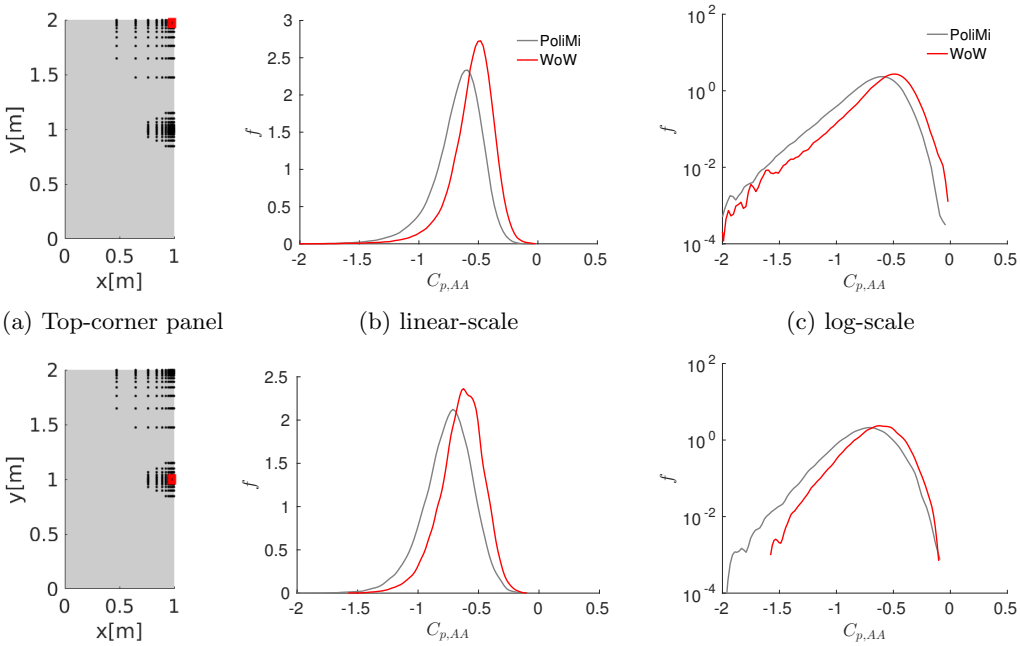

(a) Top-corner panel (b) linear-scale (c) log-scale

(d) Mid-edge panel (e) linear-scale (f) log-scale

Figure 3.16: Probability density functions of area-averaged pressure coefficient on $2 \times 3\text{m}^2$ panels, at 20° wind direction.

are limited in space and time, have a small effect on the area-averaged pressure, as evident from Figures 3.17b and 3.17e. Specifically, during the peak event observed at PoliMi, the area-averaged pressure coefficient drops below the mean value by ~ 0.7 for a period of time of ~ 34ms; at WoW a drop in area-averaged pressure coefficient of ~ 0.6 is observed for ~ 40ms. This type of event is likely not critical for the panel.

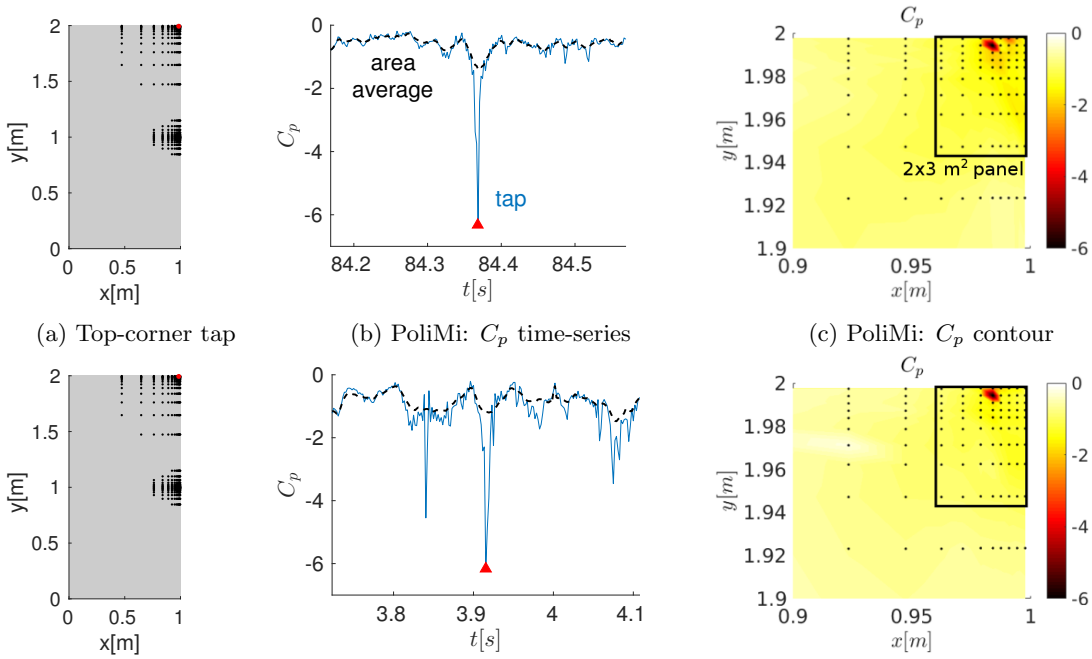

(a) Top-corner tap (b) PoliMi: C_p time-series (c) PoliMi: C_p contour

(d) Top-corner tap (e) WoW: C_p time-series (f) WoW: C_p contour

Figure 3.17: Time-series of pressure coefficient at 20° wind direction on top-corner tap, the red arrows indicate a negative peak lower than $C_p = -5$, and distribution of pressure coefficient around the tile at the time instant of the negative peak.

A completely different phenomenon can be observed during different time instants. Figure 3.18 depicts short time-series around the occurrence of pressure peaks at two nearby taps, indicated by the circles in the corresponding contour plots. The contour plots (Figures 3.18c and 3.18f) show the spatial distribution of the pressure coefficient at the time instants marked by the red arrows in the time-series (Figures 3.18b and 3.18e). In this case, both PoliMi and WoW tests experience a strong negative pressure coefficient, up to $C_p = -5$, that impacts a large portion of the tile. The time-series reveal that when the negative peak occurs in *tap 1*, *tap 2* experiences a negative peak at the same time, although weaker. This suction event extends for a longer time period than before, as evident from Figures 3.18b and 3.18e, and causes the area-averaged pressure to significantly deviate from the mean value. During the suction event measured at PoliMi, the area-averaged pressure coefficient drops below the mean value by ~ 1, for a period of time of ~ 120ms; at WoW a drop

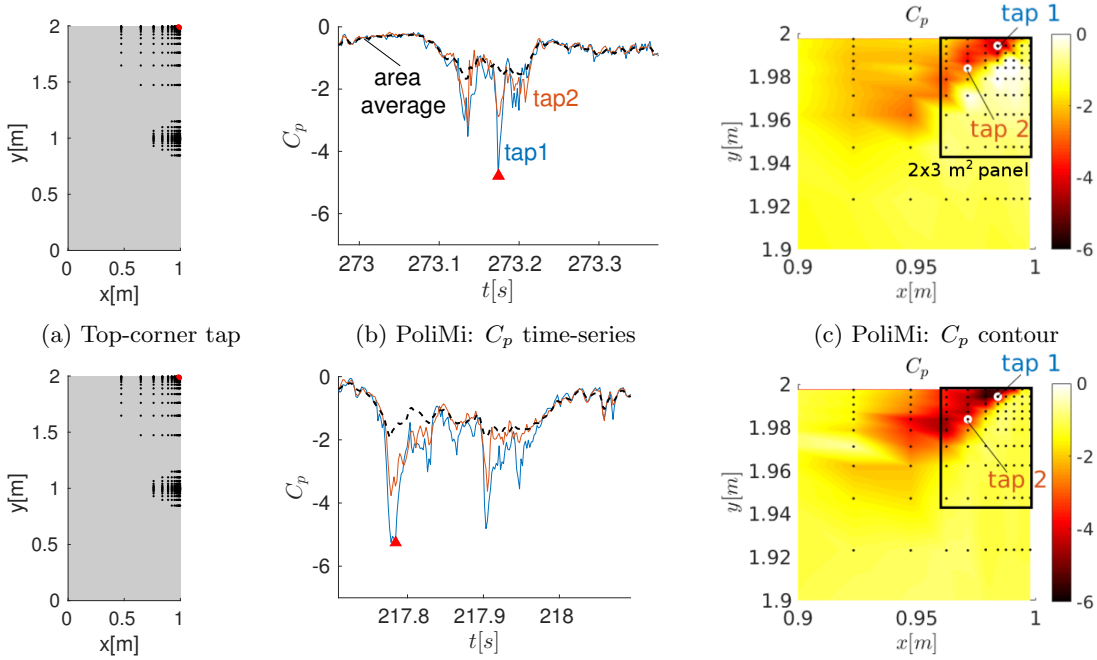

(a) Top-corner tap (b) PoliMi: C_p time-series (c) PoliMi: C_p contour

(d) Top-corner tap (e) WoW: C_p time-series (f) WoW: C_p contour

Figure 3.18: Time-series of pressure coefficient at 20° wind direction on top-corner tap, the red arrows indicate a negative peak lower than $C_p = -5$, and distribution of pressure coefficient around the tile at the time instant of the negative peak.

in area-averaged pressure coefficient of ~ 1.35 is observed for ~ 270ms. This phenomenon appears to be consistent between the two datasets, and likely represents a more critical situation than the sharp and concentrated peak of Figure 3.17.

3.3.4 Extreme value analysis

To compute the design pressure coefficients from the two datasets, we employ extreme value analysis both on the individual pressure taps and on the area-averaged value. In each case, the peak pressure coefficient is computed according to the Cook & Mayne method [21]: the time history of pressure coefficient is divided in windows, the most negative pressure coefficient is extracted from each window and a Gumbel distribution is fitted to the extreme values. We used 16 windows of size 18s, equivalent to 5min in full-scale (assuming a full-scale reference velocity of 30m/s). Since the resulting windows are shorter than the recommended 10min window size, the Gumbel distribution is corrected according to the method proposed by Cook and Mayne [21]. Figure 3.19 shows the spatial distribution of the peak pressure coefficients with a 22% probability of exceedance adjacent to the top corner of the building's lateral facade. As expected, this region of the building experiences the highest negative values; here the sharp and strong suction events, such as the ones of Figure 3.17, cause the peak pressure coefficient to reach negative values below ~ -7. The spatial distribution is very similar between both experiments, but the PoliMi values are generally lower than those obtained from the WoW; this is consistent with the higher frequency and strength of the negative peak events observed in the time series.

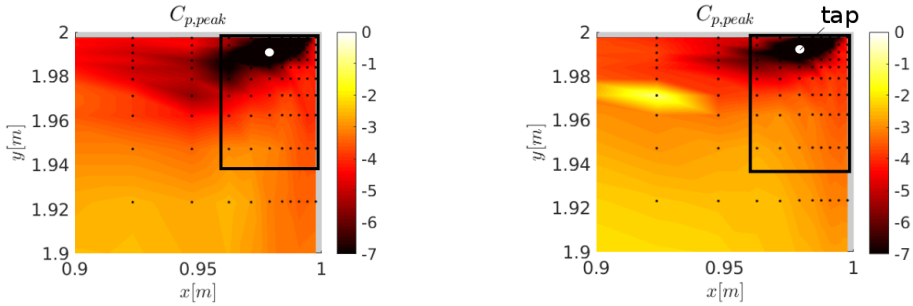

(a) PoliMi (b) WoW

Figure 3.19: Comparison of peak pressure coefficients relative to a 22% probability of exceedance, at 20° wind directions.

In terms of cladding design, the quantity of interest is the design pressure on the panels. Table 3.3 compares the design pressure coefficients relative to a 22% of exceedance and referenced to the dynamic pressure at roof height. We report both the local design pressure coefficients obtained from the single pressure tap indicated in Figure 3.19, and the values calculated for a $2 \times 3\text{m}^2$ panel, as sketched in Figure 3.19. The difference in the local values is 26%, but it reduces to only 10% when

considering the area-averaged design pressure coefficient. This can be attributed to the localized effect of a subset of the strong suction events (Figure 3.17). As for the rms C_p, the differences in the design pressure coefficients obtained from both experiments could be related to the higher turbulence intensities that characterize the ABL at WoW. If the higher turbulence intensity causes the reattachment point of the flow on the side wall to move upstream, the flow will recover faster and could exhibit less strong and less frequent pressure fluctuations in the rear portion of the model [100, 42].

	PoliMi	WoW
Top-corner tap	-12.60	-9.37
Top-corner panel	-3.34	-3.01

Table 3.3: Peak pressure coefficient relative to a 22% probability of exceedance, 20° wind direction.

Finally, Figure 3.20b shows the decrease in the absolute value of the design pressure coefficient for panels of increasing dimension, keeping the aspect ratio constant to 1.5 (Figure 3.20a). The results show good agreement between both experiments: the maximum discrepancy is $\sim 10\%$. The design pressure coefficients calculated from the PoliMi test are consistently more negative than the WoW values, which is a consequence of the more frequent and stronger suction events.

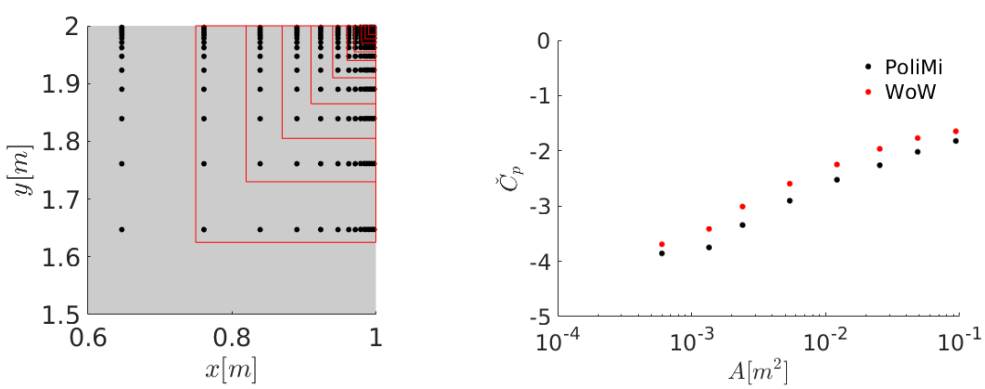

(a) Panels (b) Design pressure coefficient

Figure 3.20: Design pressure coefficient for panels of increasing area, at 20° wind direction..

3.4 Summary

The chapter presented high-resolution pressure measurements on a high-rise building model; the experiment was selected as test case for the validation of the numerical framework developed in this thesis. In particular, data acquired in in two different wind tunnels were compared.

First, we presented a comparison of the velocity statistics of the two atmospheric boundary layers. The mean velocity data recorded at WoW was within the interval defined by the spanwise variation of the PoliMi measurements over the entire building height. The turbulence intensities and integral time-scales exhibited some differences close the ground and near the top of the building. Comparison of the power spectra of the streamwise velocity component further confirmed good agreement between the ABLs generated in both experiments.

Subsequently, we compared the distributions of the mean and rms pressure coefficients on the building's lateral facade at two wind directions. The two datasets showed similar behavior; however, the negative pressure coefficient measured at WoW was slightly stronger than the one measured at PoliMi, especially in the separation region. Quantitative comparison of pressure coefficient profiles along two rows of taps indicated that the largest discrepancies in the mean and rms pressure coefficients occur near the top of the building at $0°$. The pressure power spectra for different pressure taps and at different wind directions indicated good agreement between both experiments.

Comparison of the pressure time-series recorded for the $20°$ wind direction showed frequent suction peaks in both experiments, resulting in high skewness of the PDFs of the pressure coefficients recorded at individual pressure taps. Both experiments revealed the occurrence of two types of pressure peak events: some peak events near the top corner of the building on tile A were very localized in space and time, while other events extended over a larger portion of the facade on both tile A and B. As a result, area-averaging of the pressure measurements decreased the skewness of the PDFs for the pressure coefficient, and the design pressure coefficients for panels of increasing size decreased in absolute value. These effects are similar between both experiments, but the PoliMi values for the design pressure coefficients were consistently more negative than those from WoW, with a maximum discrepancy of 10% for a $2 \times 3\text{m}^2$ panel.

In summary, the two experiments are characterized by very similar velocity and pressure data; therefore, for the remaining of the thesis, the sole PoliMi experiment will be considered for validation of the numerical framework, since it provides a more detailed characterization of the ABL.

Chapter 4

LES: optimizing inflow conditions

In this chapter, a procedure to generate turbulent inflow conditions for LES is proposed. This new inflow generation framework aims to efficiently overcome the problem of turbulence decay that affects synthetic turbulence generators [58, 54] and enable the use of LES for wind loading design. The framework employs the divergence-free turbulent inflow condition developed by Xie and Castro [60], which uses the mean velocity profile, Reynolds stress profiles and turbulence time and length scales as input parameters. This boundary condition is combined with a gradient-based optimization algorithm to find the values for these input parameters that result in the desired turbulence statistics at our downstream location of interest. The approach was designed to not require the representation of any upstream roughness elements, such that the target ABL characteristics can be achieved with minimal user intervention.

The method is tested in an empty domain and validated against the ABL measurements performed at PoliMi [4, 64]. We perform simulations of this neutral wind tunnel ABL, using the grid resolution, wall model and subgrid model that will be employed in the simulations of the high-rise building, presented in Chapter 5. A baseline simulation, using the target turbulence statistics as input parameters, is used to demonstrate the turbulence decay. Subsequently, a sensitivity analysis is performed to inform the formulation of the optimization problem. Finally, the performance of the optimization algorithm is tested, comparing the final results to the experimental data in terms of the mean velocity, Reynolds stress and length scale profiles and in terms of power spectral densities.

4.1 CFD model

The pisoFOAM solver of OpenFOAM v4.0 is used to solve the filtered incompressible Navier-Stokes equations for a neutral ABL flow with the standard Smagorinsky model ($C_s = 0.17$) [108]. The computational domain is 10m in the streamwise direction (x), 4m in the vertical direction (y) and 3m in the spanwise direction (z). It is smaller than the actual wind tunnel to limit the computational

cost, but sufficiently large to achieve our objective of testing the inflow boundary condition. The mesh counts ~ 5 million hexahedral cells, which includes refinements near the ground wall, where the minimum cell resolution is 12.5mm in the horizontal and 6.25mm in the vertical, resulting in an average y^+ of ~ 100.

The upper wall of the wind tunnel is not included in the simulations; instead we impose a slip boundary condition at the top. At the lower wall, a rough-wall logarithmic wall function is employed. The formulation is similar to the wall function commonly used in RANS simulations of the ABL [97, 87], but it is applied to the instantaneous flow field [127, 22]; it is designed to guarantee horizontal homogeneity of the ABL mean velocity profile. The left and right boundaries are periodic, and the outlet is a pressure-outlet. At the inlet we impose the logarithmic mean velocity profile from the experiment.

Synthetic turbulence is inserted just downstream of the inlet at the inflow generation plane, using the digital filter method developed by Xie and Castro [132, 60]. By imposing the turbulent velocity field on a plane inside the domain, it passes through the PISO (Pressure Implicit with Splitting of Operator) algorithm, and is adjusted to become divergence-free [60]. This eliminates non-physical pressure fluctuations that would otherwise be observed, which is especially important when estimating peak pressure loads on buildings. Figure 4.1 shows the location of the plane inside the domain, together with iso-surfaces of the second invariant of the velocity gradient tensor Q [39], colored by values of velocity magnitude.

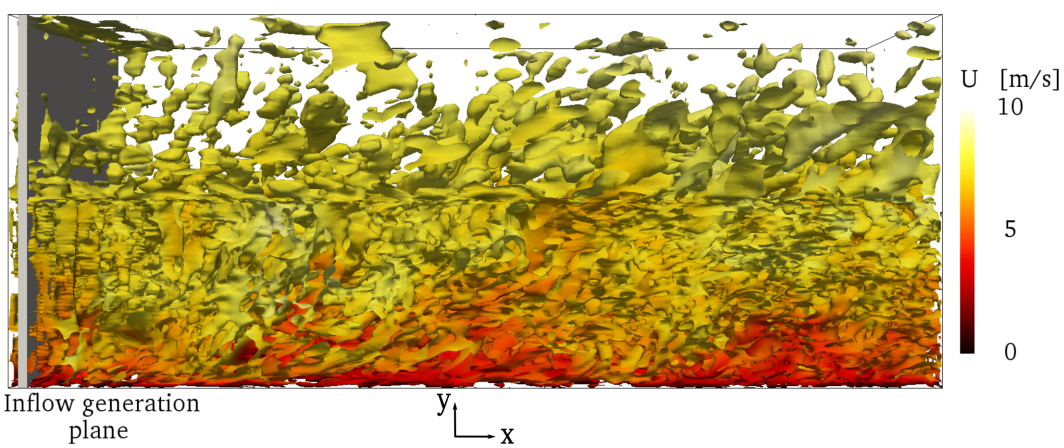

Figure 4.1: Generation of synthetic turbulence in the LES. Iso-surfaces of the second invariant of the velocity gradient tensor Q colored by values of velocity magnitude.

The turbulent velocity field imposed by the digital filter method is defined as follows:

$$u_i = U_i + a_{ij} u_{*,j}, \tag{4.1}$$

where U_i is the mean velocity, a_{ij} the Cholesky decomposition of the Reynolds stress tensor and

$u_{*,j}$ is a fluctuation with a zero-mean and an exponential spatial and temporal correlation. The matrix a_{ij} is a function of the specified Reynolds stress profiles as a function of height; since the flow is homogeneous in the spanwise direction, the relevant Reynolds stress components are the normal stresses ($\overline{u'^2}$, $\overline{v'^2}$ and $\overline{w'^2}$), and the streamwise-vertical shear stress ($\overline{u'v'}$). The fluctuation $u_{*,j}$ is the filtered random field, which introduces the coherent structures. It requires the specification of the integral length scales, which are assumed to be constant with height, and are thus obtained from averaging the experimental values along the height.

Since the spatial resolution of the hot-wire measurements is insufficient to compute 2-point correlations, we rely on Taylor's hypothesis [121] to compute the streamwise integral length-scales:

$$^{x}L_u = UT_u, \quad ^{x}L_v = UT_v, \quad ^{x}L_w = UT_w, \tag{4.2}$$

where U is the streamwise component of the mean velocity and T_u, T_v and T_w are the integral time-scales. We then approximate the vertical and spanwise length-scales as follows [3]:

$$^{y}L_u = 0.2^{x}L_u \ = \ ^{y}L_v \ = \ ^{y}L_w \tag{4.3}$$

$$^{z}L_u = 0.3^{x}L_u \ = \ ^{z}L_v \ = \ ^{z}L_w \tag{4.4}$$

In summary, the turbulent velocity field of Equation 4.1 will be a function of the mean logarithmic velocity profile, four Reynolds stress profiles and three averaged time-scales.

We differentiate the momentum equation using a central scheme and integrate in time using a backward Euler method with a time step of 0.002s. The resulting mean Courant number is less than 0.2, while the maximum varies between 1 and 2 throughout the simulation. In the baseline simulation of Section 4.2 we averaged statistics over a period of more than $40t_\star$ after an initialization period of $12.5t_\star$, where $t_\star = \delta/u_\star$ and δ is half of the domain height [60]. Subsequent simulations were initialized from the baseline result to accelerate the convergence, but the initialization period of $12.5t_\star$ was maintained. The simulations are stopped when the maximum difference in the Reynolds stresses calculated at a $4t_\star$ interval is less than 3%. The resulting simulated time is between $150 - 200$s.

4.2 Preliminary results

4.2.1 Baseline simulation

We first performed a simulation imposing the desired mean velocity profile and turbulence statistics as inflow parameters, to verify the streamwise evolution of the flow statistics. All the profiles shown represent the variation over height of the statistics of interest 5m downstream of the inlet at the mid spanwise location. Figure 4.2 shows that the mean velocity profile is maintained throughout the domain. This is a result of the formulation of the rough-wall logarithmic wall function, which is

consistent with the ABL mean velocity profile imposed at the inlet.

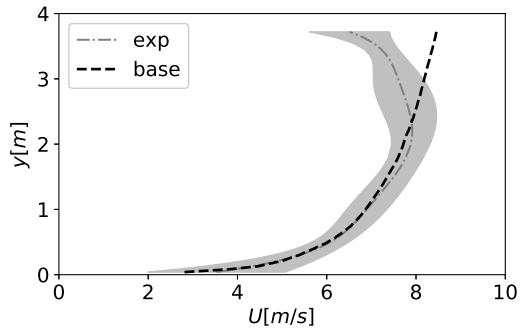

Figure 4.2: Comparison of the experimental mean velocity profile with the mean velocity profile computed by the baseline simulation 5m downstream of the inlet.

In contrast, Figure 6.2 shows that 5m downstream of the inflow generation plane (i.e. at the intended location of the building model in future LES) a decrease in turbulence kinetic energy of up to 50% is observed. This demonstrates the limitation of synthetic turbulence generators: since the imposed turbulent velocity field is not a solution of the system of equations being solved, the specified inflow statistics will develop towards an equilibrium condition that depends on the subgrid model, the wall model and the discretization used.

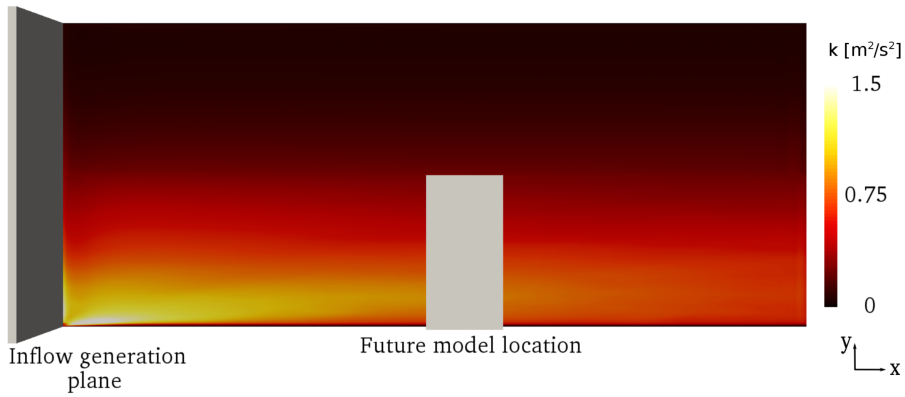

Figure 4.3: Decay of turbulence kinetic energy in the LES.

The turbulence decay can be seen in more detail in Figure 4.4, where the profiles of turbulence kinetic energy and Reynolds stresses 5m downstream of the inlet are compared with the spanwise-averaged wind tunnel profiles (i.e. the profiles imposed at the inflow). At 5m from the inlet, the streamwise velocity variance is up to ∼60% lower than the one imposed at the inflow and ∼50% lower on average. The vertical and spanwise components are decreased up to ∼60% and ∼50%

respectively; the average decay is ∼45% for the vertical component and ∼20% for the spanwise component. We note that the Reynolds stresses plotted in Figure 4.4, and in the remainder of the paper, are the resolved stresses; the subgrid components are not considered because they are negligibly small.

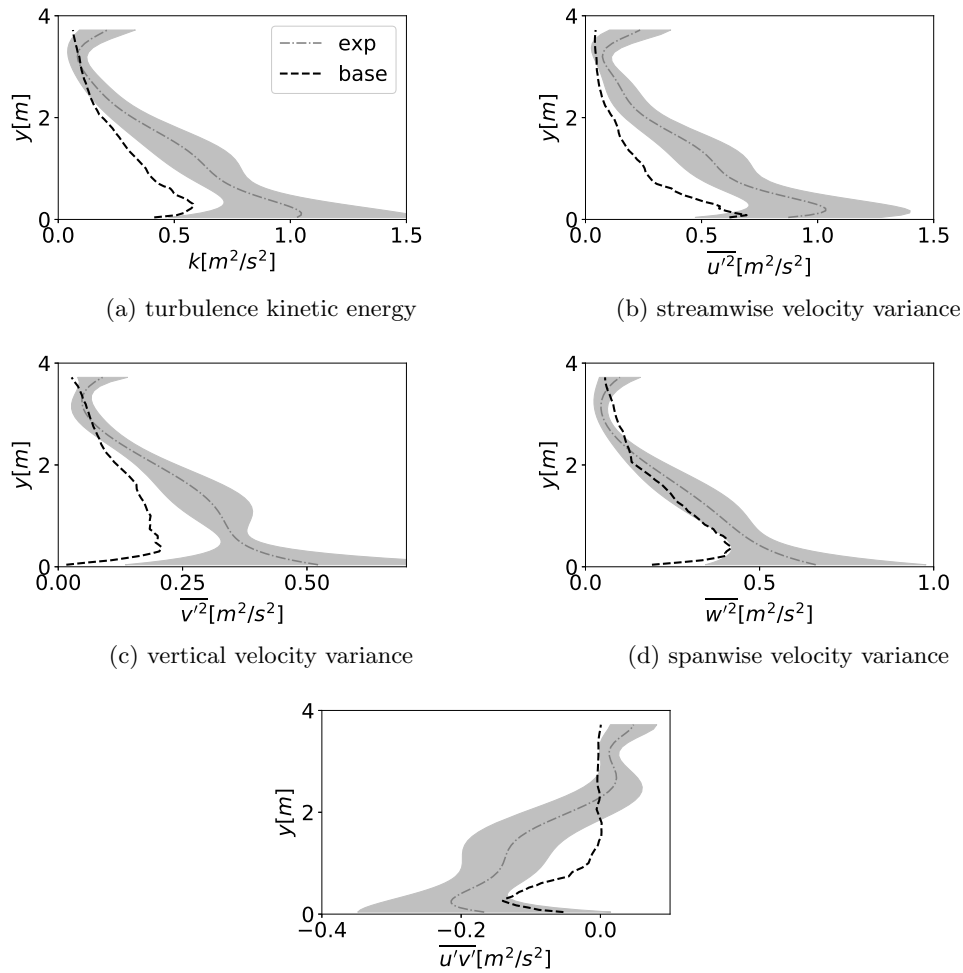

(a) turbulence kinetic energy

(b) streamwise velocity variance

(c) vertical velocity variance

(d) spanwise velocity variance

(e) streamwise-vertical shear stress

Figure 4.4: Comparison of the experimental turbulence kinetic energy and Reynolds stress profiles with the corresponding profiles computed by the baseline simulation 5m downstream of the inlet.

Figure 4.5 shows that the streamwise inhomogeneity in the integral length scales is smaller than that in the Reynolds stresses. The streamwise length scale modeled by the baseline LES is inside the gray target region up to 3m height, and quite close to the spanwise-averaged measurement. The vertical and spanwise components are overestimated, especially near to the ground. This is likely related to the fact that we specify a constant profile over height for the turbulence length-scales at

the inflow.

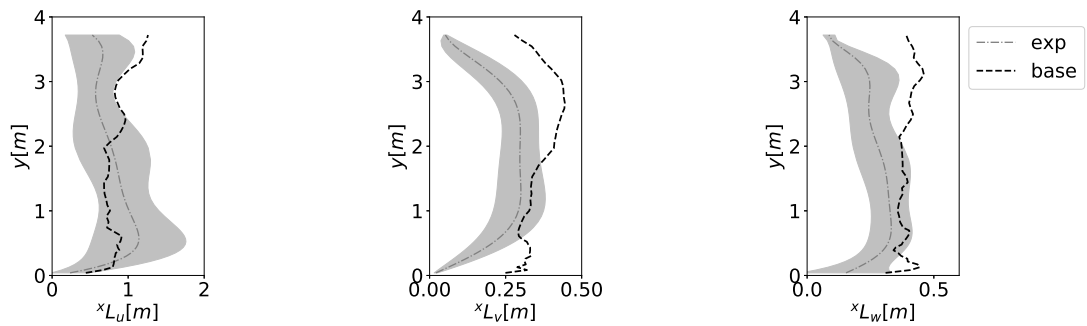

(a) streamwise length-scale (b) vertical length-scale (c) spanwise length-scale

Figure 4.5: Comparison of the experimental integral length scales with the length scales computed by the baseline simulation 5m downstream of the inlet.

4.2.2 Sensitivity analysis

To mitigate the effect of the observed turbulence decay on the quantities of interest, an optimization problem can be formulated to find the input parameters that will produce the desired turbulence statistics at the location of interest. To support the formulation of an effective objective function, we first performed a sensitivity analysis to identify the influence of the different input parameters on the quantities of interest.

The inflow algorithm is a function of the mean velocity profile, four Reynolds stress profiles and three integral time-scales. The baseline simulation confirmed that we can maintain the mean velocity profile by modifying the wall functions; hence, there is no need to change the logarithmic profile at the inflow generation plane. In addition, the shear stress $\overline{u'v'}$ will adjust automatically to changes in the normal components $\overline{u'^2}$ and $\overline{v'^2}$, following the realizability constraint $(\overline{u'v'})^2 \leq \overline{u'^2}\ \overline{v'^2}$ [103]. Based on these considerations, the input mean velocity and shear stress are not included in the sensitivity study. Hence, six additional LES simulations were performed, increasing the remaining parameters by a factor of two one at a time. For the Reynolds stresses this implies that the x-coordinate of the parametrization points of the Bezier curves was increased by a factor of two (see Section 4.3.1).

Figure 4.6 shows the mean velocity profiles resulting from the six LES simulations compared to the baseline; the legend in the plot indicates which of the input parameters has been doubled. As expected, the profiles at the building location collapse to the baseline result: the only input parameter that matters for the mean velocity is the logarithmic inlet profile.

Figure 4.7 shows that the input parameters $\overline{u'^2}$, T_v and T_w have a relatively small effect on

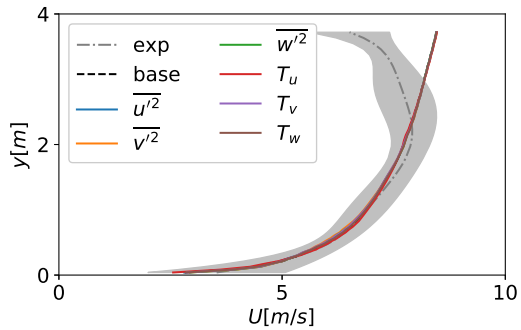

Figure 4.6: Influence of the inflow parameters on the mean velocity $5m$ downstream of the inlet. The inflow parameters are doubled one at a time; the legend indicates the doubled parameter.

the turbulence kinetic energy and Reynolds stresses at the target location. Doubling the integral time-scale T_u at the inlet causes an even stronger turbulence decay than the one experienced by the baseline simulation, but when doubling the inflow $\overline{v'^2}$ and $\overline{w'^2}$, the resulting profile of the turbulence kinetic energy falls completely inside the target region. The influence of individual spanwise and vertical Reynolds stress components is stronger on their respective values further downstream, and they have a similar effect on $\overline{u'^2}$. In particular, when doubling $\overline{v'^2}$ at the inflow, the corresponding component at the building location is on average $\sim 60\%$ higher than the baseline result, while $\overline{u'^2}$ and $\overline{w'^2}$ experience an average increase of $\sim 40\%$ and $\sim 15\%$ respectively. When doubling $\overline{w'^2}$ at the inflow, the corresponding values at the downstream building location increase by $\sim 50\%$ on average compared to the baseline simulation. The resulting values exceed the target values, indicating that the imposed perturbation might be too large. The streamwise and vertical Reynolds stress components also increase by $\sim 45\%$. As expected, the effect on the shear stress is similar to that on the streamwise and vertical velocity variance.

The downstream length-scale profiles are most sensitive to changes in their corresponding time- or length-scales at the inflow, as shown in Figure 4.8. The streamwise component increases by $\sim$50% on average when doubling T_u; increasing T_v causes a $\sim$28% mean increase in the vertical length-scale; doubling T_w produces an average $\sim$60% increase on the spanwise length-scale at the building. This trend is less consistent close to the wall, where the vertical length scale is more strongly affected by the streamwise value at the inlet, while the spanwise length scale is sensitive to both the streamwise and the vertical component.

The integral length-scales represent the size of the largest eddies, while the Reynolds stresses quantify the intensity of fluctuations. The result of the sensitivity analysis suggests an interaction between the Reynolds stresses and the turbulence length-scales. However, to perform the optimization, we modify the input Reynolds stresses that have a smaller influence on the target length-scales (i.e. $\overline{v'^2}$ and $\overline{w'^2}$), and the input length-scales that have a smaller effect on the target Reynolds

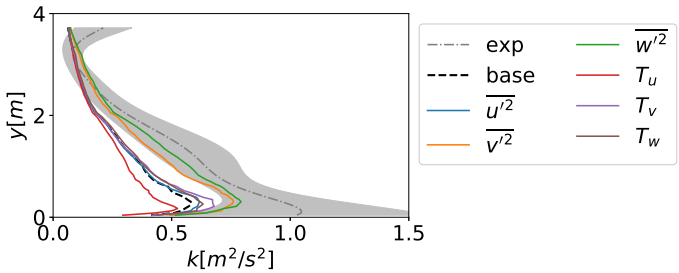

(a) turbulence kinetic energy

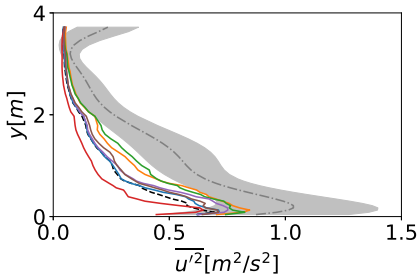

(b) streamwise velocity variance

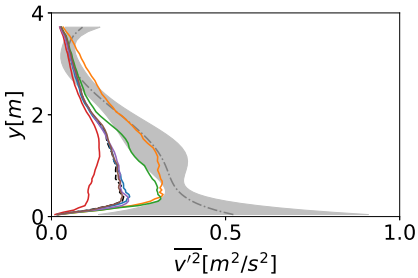

(c) vertical velocity variance

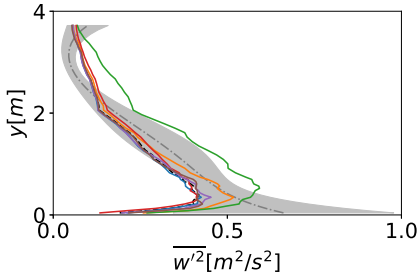

(d) spanwise velocity variance

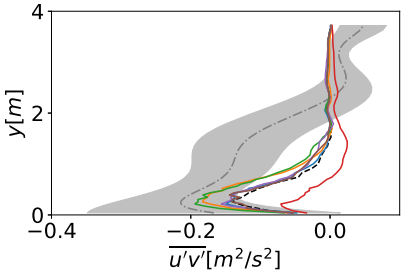

(e) streamwise-vertical shear stress

Figure 4.7: Influence of the inflow parameters on the Reynolds stresses $5m$ downstream of the inlet. The inflow parameters are doubled one at a time; the legend indicates the doubled parameter.

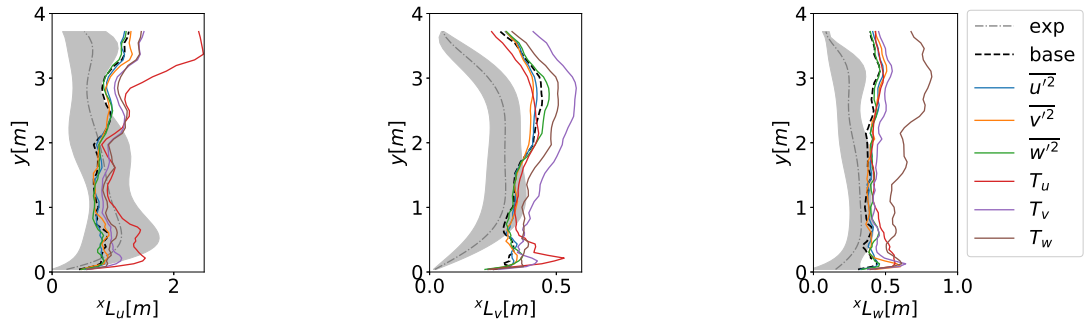

(a) streamwise length-scale (b) vertical length-scale (c) spanwise length-scale

Figure 4.8: Influence of the inflow parameters on the integral length scales $5m$ downstream of the inlet. The inflow parameters are doubled one at a time; the legend indicates the doubled parameter.

stresses (i.e. T_v and T_w). These input variables thus support performing the optimization for the Reynolds stresses and the length scales independently.

4.3 Gradient-based optimization

We implemented a gradient-based optimization algorithm because the sensitivity analysis confirmed that the turbulence statistics change monotonically: higher Reynolds stresses or integral time scales at the inflow generation plane will result in higher Reynolds stresses or integral time scales at the future building location. The algorithm dynamically adjusts the input parameters of the synthetic turbulence generator, until the statistics at the location of interest are sufficiently close to the wind tunnel measurements. In the following, we first describe the parameterization of the Reynolds stress profiles that will be used for the optimization. Subsequently we discuss the definition of the objective function.

4.3.1 Bezier parametrization

We parametrize the input Reynolds stresses using Bezier curves [112], to control the shape of the profiles throughout the optimization steps. A Bezier curve is defined by a number of control points; the curve passes through the first and last point, while it gets attracted by the intermediate points. Figure 4.9 shows the input Reynolds stresses $\overline{v'^2}$ and $\overline{w'^2}$ resulting from the parametrization with 8 control points; the control points are more concentrated in the region below $0.5m$, where the profiles experience the highest variation.

The optimization algorithm acts on the x-coordinate of the control points, except for the first and last one, which are fixed: the points are moved back and forth along the x-axis depending on

the gradient of the objective function.

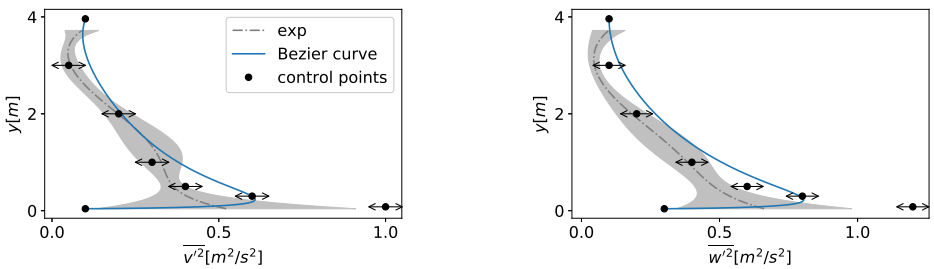

(a) vertical velocity variance (b) spanwise velocity variance

Figure 4.9: Parametrization of the input Reynolds stresses with Bezier curves.

4.3.2 Objective functions

The sensitivity study showed that the Reynolds stresses at the building can be increased by increasing $\overline{v'^2}$ and $\overline{w'^2}$ at the inflow. Therefore, we opt for a multi-objective optimization procedure, in which the decision variables are the profiles of $\overline{v'^2}$ and $\overline{w'^2}$ at the inflow generation plane. This should enable higher turbulence intensities at the downstream location, while maintaining integral length scales similar to the baseline result. Going one step further, we can also try to obtain better integral length scales by selecting the input T_v and T_w as additional decision variables. The input T_u was not included because it also affects the Reynolds stresses; we choose to separate the optimization of the integral length-scales from the optimization of the Reynolds stresses.

To solve the resulting multi-objective algorithm we rely on the scalarization technique, which is the simplest way of solving a multi-objective problem [13]. In the scalarization technique the objective functions are weighted and combined into a single objective function. The resulting function is a linear combination of the least-squares differences between the statistics obtained by the LES, and the corresponding target experimental values. Considering the Reynolds stresses as our quantities of interest, the objective function assumes the following form:

$$\begin{aligned} f_p\Big((\overline{v'(y_p)^2})_i, (\overline{w'(y_p)^2})_i\Big) =& \frac{1}{2}\gamma_u\Big((\overline{u'(y_p)^2})_b - (\overline{u'(y_p)^2})_{exp}\Big)^2 \\ &+\frac{1}{2}\gamma_v\Big((\overline{v'(y_p)^2})_b - (\overline{v'(y_p)^2})_{exp}\Big)^2 \\ &+\frac{1}{2}\gamma_w\Big((\overline{w'(y_p)^2})_b - (\overline{w'(y_p)^2})_{exp}\Big)^2, \end{aligned} \tag{4.5}$$

where y_p is the height of the pth Bezier point, and γ_u, γ_v and γ_w are the weights. The subscripts $()_i$, $()_b$ and $()_{exp}$ indicate the Reynolds stresses at the inflow generation plane, at the future building location, or the target values from the experiment respectively. The weights need to sum to 1 and

be strictly positive [13]; we chose them depending on the importance of each normal Reynolds stress relative to the turbulence kinetic energy, thus $\gamma_u = 0.5$, $\gamma_v = 0.2$ and $\gamma_w = 0.3$. We treat the 6 intermediate control points as independent; hence, we solve 6 optimization problems in parallel (i.e. one for each y_p value).

When we add the integral time-scales as quantities of interest, the objective function is completely analogous, but there is no vertical variation in this case:

$$f_T\Big(T_{v,i}, T_{w,i}\Big) = \frac{1}{2}\gamma_u\Big(T_{u,b} - T_{u,exp}\Big)^2 + \frac{1}{2}\gamma_v\Big(T_{v,b} - T_{v,exp}\Big)^2 + \frac{1}{2}\gamma_w\Big(T_{w,b} - T_{w,exp}\Big)^2, \tag{4.6}$$

where the weights are the same as before.

4.4 Results

In the following section we present the results of the two approaches described above, i.e. we solve two different optimization problems: one that minimizes the objective function of Equation 4.5 and another that minimizes both the objective functions of Equations 4.5 and 4.6.

4.4.1 Optimization of input Reynolds stresses

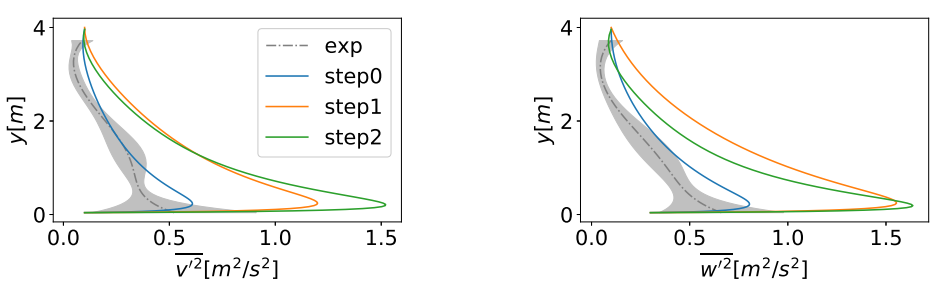

(a) vertical velocity variance (b) spanwise velocity variance

Figure 4.10: Input Reynolds stresses modified by the optimization.

To compute the gradient from two non-trivial solutions at the start of the optimization, we employ the baseline result and perform an additional simulation doubling the input parameters that are decision variables, i.e. $\overline{v'^2}$ and $\overline{w'^2}$. We will refer to the baseline simulation as *step0* of the optimization and to the additional simulation as *step1*. The input profiles of mean velocity, streamwise velocity variance and shear stress are obtained from the measurements and never modified by the code. The same holds for the input integral time-scales, which are specified as the average

of the corresponding measurement over height. We ran one step of the optimization, which will be referred to as *step2*; the resulting input profiles for all three steps are plotted in Figure 4.10.

The analysis of the results at the location of interest focuses on the Reynolds stresses and length scales; similarly to the sensitivity analysis, the mean velocity profile was not affected by the Reynolds stresses at the inflow.

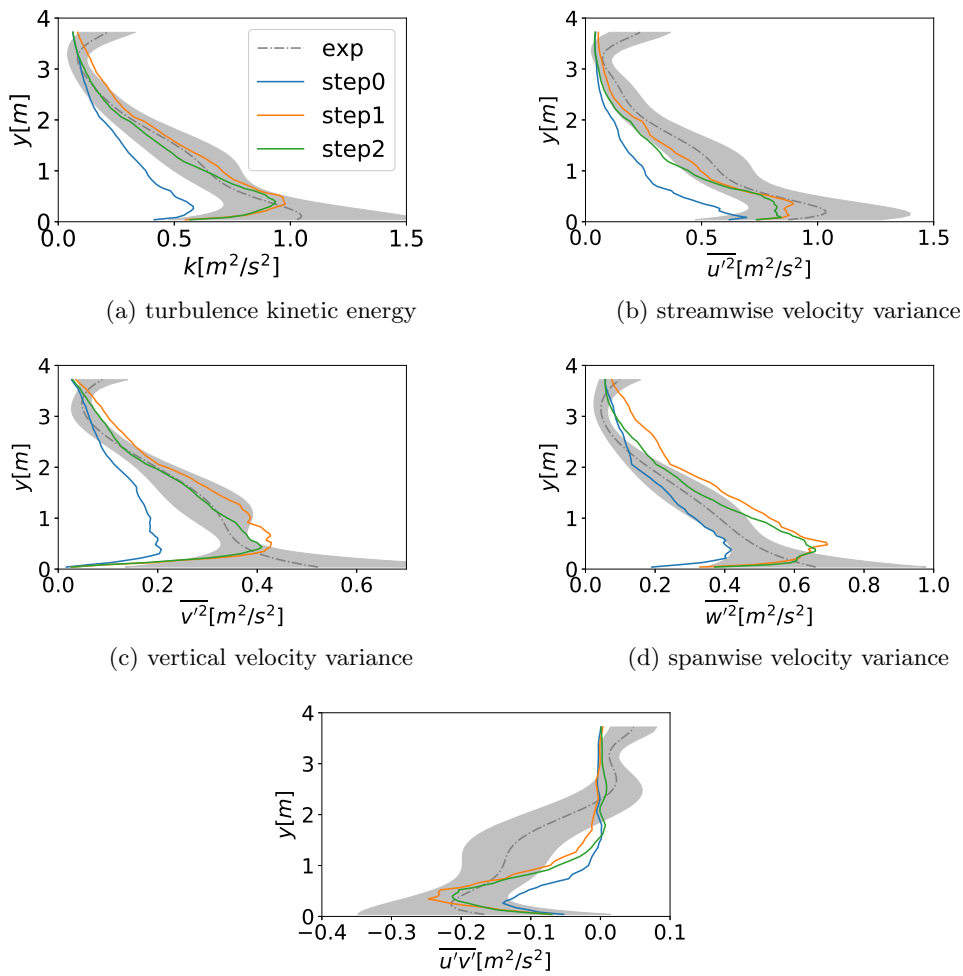

(a) turbulence kinetic energy

(b) streamwise velocity variance

(c) vertical velocity variance

(d) spanwise velocity variance

(e) streamwise-vertical shear stress

Figure 4.11: Reynolds stresses 5m downstream of the inlet as a result of the optimization.

Figure 4.11 shows the turbulence kinetic energy and Reynolds stresses at the future building location for the different steps. The results for *step0* are those from the baseline simulation. For *step1* the turbulence kinetic energy and Reynolds stresses $\overline{u'^2}$ and $\overline{v'^2}$ at the location of interest are already within the gray zone representing the spanwise variation of the measurements over most of the domain height. The values for $\overline{w'^2}$ become too high at the building location, the maximum

discrepancy from the upper bound of the target region is $\sim 28\%$ and the average is $\sim 14\%$. This explains why in *step2*, the input profile of $\overline{v'^2}$ remains basically unchanged above $1m$ height, while $\overline{w'^2}$ is decreased to a value in between *step0* and *step1*. Near the ground, the optimization algorithm results in the strongest increase for both input Reynolds stresses, since the turbulence decay is stronger in this region.

The results show that only one step in the optimization is required to reach a level of turbulence kinetic energy at the building location that is very close to the spanwise-averaged profile of the experiment. $\overline{v'^2}$ is now entirely inside the gray region that represents the spanwise variation of the experiment, while $\overline{u'^2}$ satisfies the requirement below $1m$ and above $1.8m$. In the region in between, the discrepancy from the lower bound of the target region is $\sim 7\%$ on average. The wall-normal stress ($\overline{w'^2}$) remains slightly too high around $y = 0.5m$; here the maximum discrepancy from the upper bound of the target region is $\sim 12\%$. The result for the shear stress is similar to that for the streamwise component: it falls inside the target region below $1m$ and above $1.8m$ height.

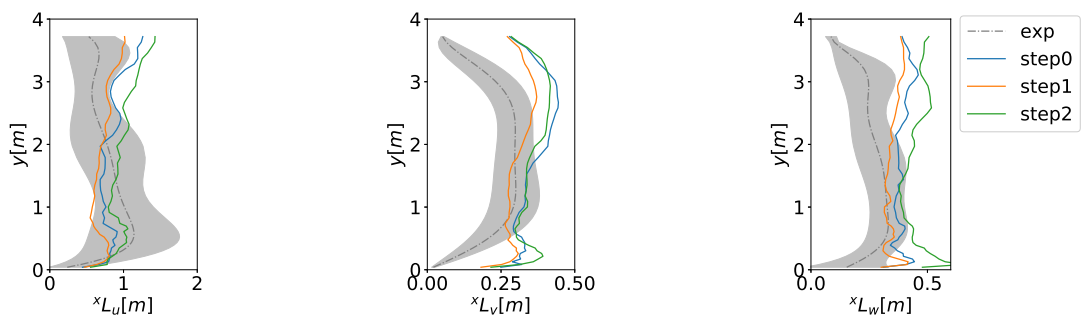

(a) streamwise length-scale (b) vertical length-scale (c) spanwise length-scale

Figure 4.12: Modeled integral length-scales 5m downstream of the inlet as a result of the optimization.

Figure 4.12 shows the effect of the optimization on the integral length scales. For the streamwise component the profile modeled by the simulation of *step2* is very close to the spanwise-averaged measurement below $y = 2.5m$, which is the region of interest for the future simulation with the high-rise building. Above this height the average deviation between the simulated profile and the upper bound of the gray region is $\sim 8\%$. The vertical component is within the gray region that represents the spanwise variation of the experiment between $y = 0.5m$ and $y = 2m$, but deviates more significantly close to the ground and above $2m$, where the average discrepancy is more than 50%. The spanwise integral length-scale is characterized by a similar behavior. The discrepancy close to the ground is most likely caused by the fact that the inflow generation algorithm requires specifying a constant value for the integral length-scales over height. As a result, the integral length-scales imposed near the ground at the inflow are larger than the length-scales obtained in the wind

tunnel, and the optimization process can not compensate for this difference. For the vertical and spanwise length scales, the agreement with the measurement deteriorates between step 1 and step 2, which motivates including the length scales in the objective function for the optimization.

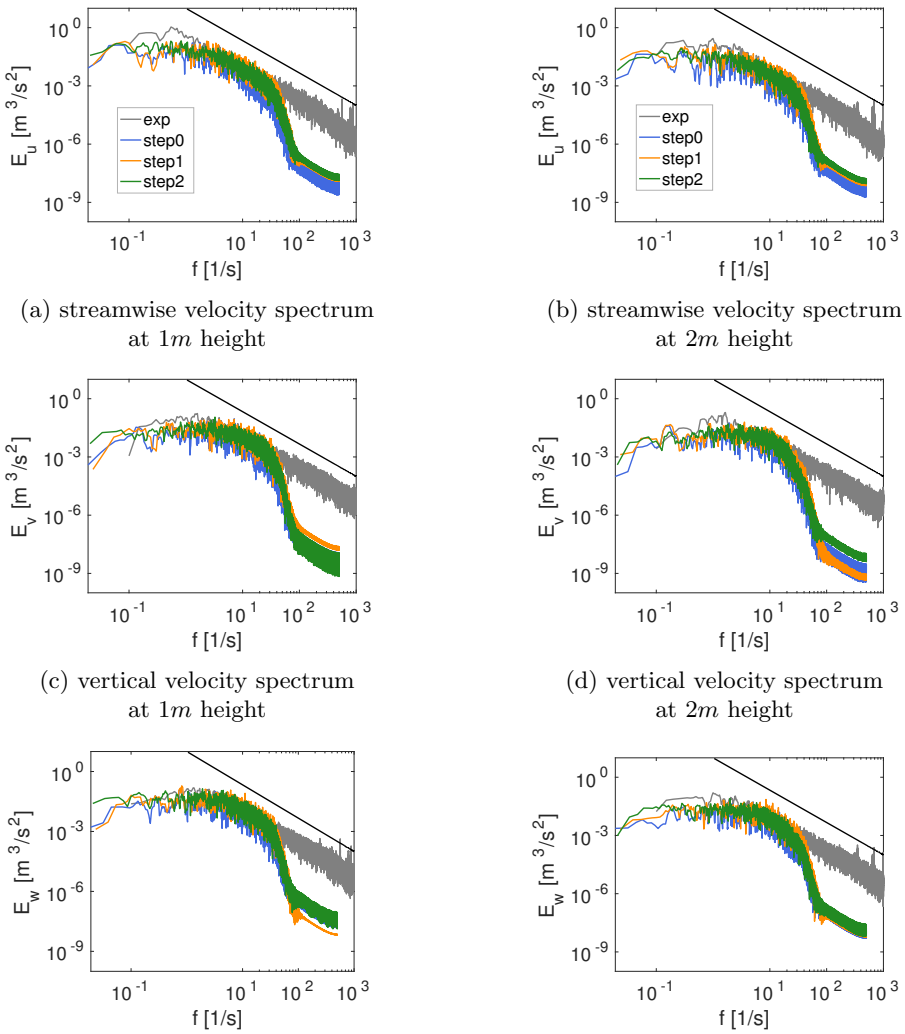

(a) streamwise velocity spectrum at $1m$ height

(b) streamwise velocity spectrum at $2m$ height

(c) vertical velocity spectrum at $1m$ height

(d) vertical velocity spectrum at $2m$ height

(e) spanwise velocity spectrum at $1m$ height

(f) spanwise velocity spectrum at $2m$ height

Figure 4.13: Modeled power spectrum, $5m$ downstream of the inlet, as a result of the optimization.

Figures 4.13 presents the spectra of the three velocity components at the downstream location of interest at $1m$ and $2m$ height. At both heights, the highest frequency captured by the hot-wires is $1000Hz$, while the LES resolves scales below $50Hz$, as evident from the energy decay above this frequency. In the range of resolved scales, the LES spectra agree well with the experiment, and the turbulence is resolved into the inertial sub-range. The optimization process is shown to improve

the energy content in the LES, in particular in the inertial sub-range. The observations for the large-scale portion of the spectra are consistent with the results for the Reynolds stresses: the power spectrum of the spanwise velocity fluctuations reaches a higher energy content compared to the experiment, while the streamwise and vertical components are slightly underestimated.

4.4.2 Optimization of input Reynolds stresses and time scales

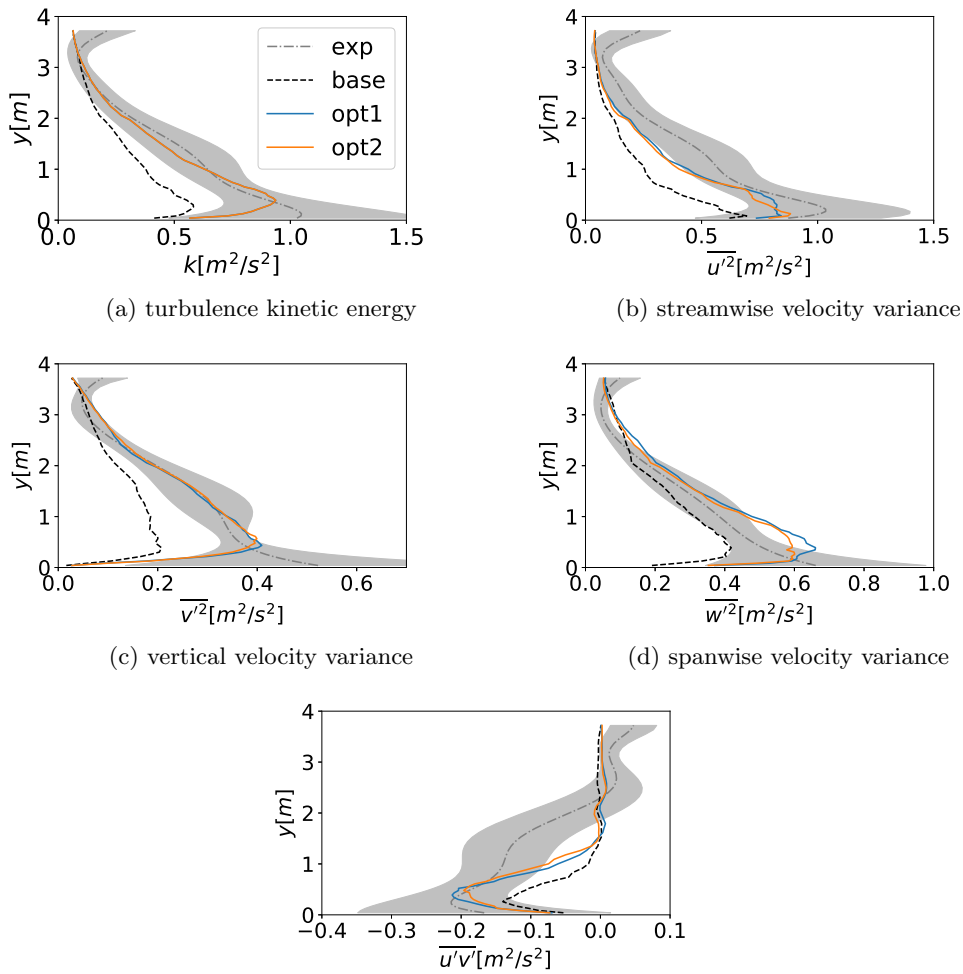

(a) turbulence kinetic energy

(b) streamwise velocity variance

(c) vertical velocity variance

(d) spanwise velocity variance

(e) streamwise-vertical shear stress

Figure 4.14: Modeled Reynolds stresses 5m downstream of the inlet as a result of the second optimization problem.

When solving the optimization problem that minimizes both the objective functions of Equations 4.5 and 4.6, the input Reynolds stresses of the optimization step are exactly the same as before,

while the input time scales are different. In this case we relied on the results of the sensitivity analysis to compute the gradients of the integral time scales; by combining the information from the baseline and the two simulations in which we doubled T_v or T_w we can compute the new input integral time-scales using Equation 4.6.

Figure 4.14 compares the results of the two optimization problems for the Reynolds stresses, showing that the results are very similar. This is as expected, since the sensitivity analysis showed a small influence of the parameters T_v or T_w on the Reynolds stresses.

Figure 4.15 presents the turbulence length-scales at the building location, showing that the second optimization problem performs slightly better. The streamwise length scale is improved on the top part of the domain: it is outside the gray region just above $3m$ and the error is very small. The spanwise length-scale is closer to the spanwise-averaged measurement and almost everywhere inside the target region. The vertical component of the integral length scale is very similar, but shows a slight improvement close to the wall. The results demonstrate that including the length scales in the objective function can improve the comparison with the experimental data. However, the fact that the input value for the length scale is constant with height limits the control in terms of reproducing the shape of the profile obtained from the experiment.

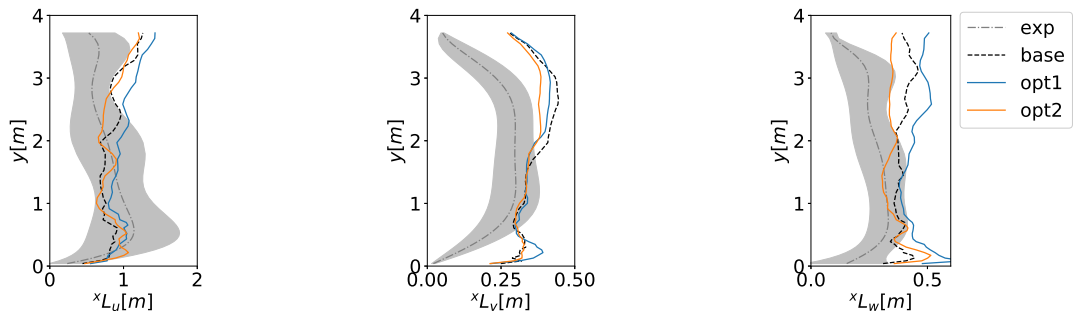

(a) streamwise length-scale (b) vertical length-scale (c) spanwise length-scale

Figure 4.15: Modeled integral length-scales 5m downstream of the inlet as a result of the second optimization problem.

4.5 Summary

The chapter proposed an efficient inflow generation framework to overcome the problem of turbulence decay that affects synthetic turbulence generators; the framework was based on the divergence-free inflow condition developed in [60] and incorporated a gradient-based optimization procedure to calibrate the input parameters. The procedure was formulated to obtain user-specified Reynolds stresses and turbulence length scales at a downstream location of interest in the computational

domain; it did not attempt to solve the complex problem of horizontal homogeneity that affects LES of ABL flows.

As part of a first optimization strategy, we solved a multi-objective optimization problem to seek the inlet values of $\overline{v'^2}$ and $\overline{w'^2}$ that produce the target Reynolds stresses at the location of interest. The results showed that the mean velocity profile downstream of the inflow is not affected by the change in the input Reynolds stresses and turbulence length scales. For the Reynolds stress profiles the optimized result compared considerably better to the measurements than the baseline simulation. The effect of the input $\overline{v'^2}$ and $\overline{w'^2}$ on the integral length-scales was relatively small.

A second approach attempted to further improve the length scales values; thus, the optimization problem for the Reynolds stresses was identical as before, but an additional objective function was incorporated to obtain the target length scales at the location of interest by adjusting the input values for T_v and T_w. The results showed a slight improvement in the predicted turbulence length scales at the building location, but the vertical and spanwise length scales continued to be over predicted below 0.5m height. This was likely related to the uniform profiles of length scales imposed at the inflow, thereby not allowing to reproduce the shape of the experimental profiles.

In summary, the proposed method represents an efficient way to design LES simulations of ABL flows that provide user-specified turbulence statistics at a downstream location of interest in the domain. The method will be employed in the next chapter to simulate the flow around the high-rise building model.

Chapter 5

LES: inflow sensitivity analysis

In this chapter, the inflow generation method proposed in Chapter 4 is employed to simulate the flow around the high-rise building model. Furthermore, we investigate the effect of uncertainty in the definition of the input parameters of the method, on the pressure distribution around the building. Specifically, three uncertain parameters that define the incoming surface layer are identified: the roughness length of the terrain, the turbulence kinetic energy and the integral time scale of the streamwise velocity component. These parameters are characterized using the available wind tunnel measurements, and the inflow optimization is performed to identify 27 realizations of digital filter input parameters that represent the variability in the wind tunnel flow conditions. The ensemble of the 27 LES results is then analyzed to assess uncertainty in the predicted mean, rms and peak pressure coefficients. We consider both local peak pressure coefficients and design pressure coefficients averaged over different panel sizes, which are the quantities of interest for cladding design. The results are compared to the wind tunnel data for validation and additional analysis is performed to provide insight on the relative importance of the different uncertain inflow parameters.

The remainder of this chapter is organized as follows: Section 5.1 introduces the LES setup and the details of the inflow sensitivity analysis, while Section 5.2 presents the results.

5.1 Methods

5.1.1 CFD model

All LES simulations are performed using the pisoFOAM solver of OpenFOAM v4.0. The computational domain is 20×5m in the streamwise and spanwise directions; the height of the domain is equal to the wind tunnel height, i.e. 4m (see Chapter 3). The high-rise building is located at a distance of 5m from the inlet boundary and 14m from the outlet [24]. The blockage ratio, i.e. the ratio between the area of the windward face of the building and the domain cross section, is

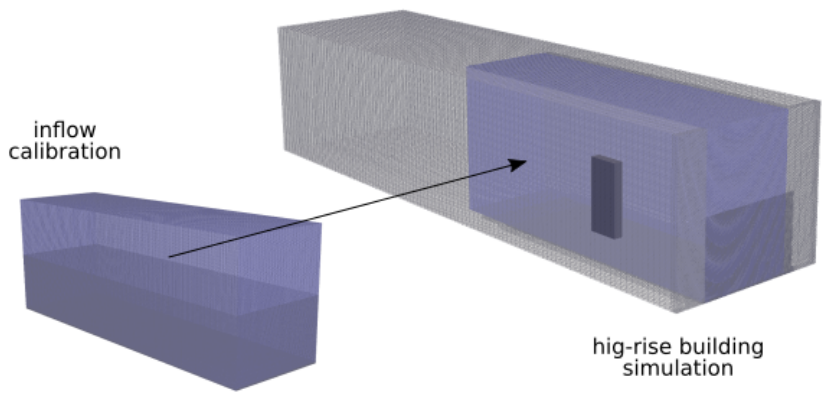

Figure 5.1: Domain and mesh

2.8% [31]. The mesh includes refinement regions close to the ground and to the building model, for a total of 7.5 million hexahedral cells. The refinement regions aim to reproduce exactly the mesh resolution of the empty domain used to calibrate the inflow parameters, as sketched in Figure 5.1. The highest spatial resolution is achieved next to the corners of the building, similar to the pressure tap distribution in the wind tunnel experiment. In these regions, the resolution is 3.2mm, 1.6mm and 0.8mm in the streamwise, spanwise and vertical directions, respectively; the resulting y^+ is 100 on average. Subgrid-scale turbulence is modeled using the standard Smagorinsky model [108]. As part of a grid dependency analysis, the mean and rms pressure coefficients computed from the present mesh were compared to the ones computed from a coarser mesh, with 4 times lower spatial resolution next to the corners and edges of the building; the comparison resulted in $R^2 = 0.97$ and $R^2 = 0.83$, respectively.

To generate a turbulent flow field at the inflow, we employ the framework presented in Chapter 4. On the side boundaries periodic boundary conditions are imposed, while on the top boundary we impose a slip boundary condition. The outlet is treated as a pressure-outlet with constant relative pressure equal to zero and a zero-gradient boundary condition for the other flow variables. The momentum and turbulence model equations are discretized using second order numerical schemes and iteratively solved using a linear solver with a symmetric Gauss-Seidel smoother. The Poisson equation is approximated with second order schemes and solved using the generalised geometric-algebraic multi-grid (GAMG) solver with Gauss-Seidel smoother. To monitor convergence of the time-statistics, we select 4 pressure taps around the building (i.e. one per pressure tile of the PoliMi experiment, see Figure 3.2) and run the simulations until the corresponding mean and rms pressure coefficients stopped varying. After this burn-in period, we further run the simulations for $50 - 60$s to obtain the pressure time-series, with a 0.0001s time-step.

5.1.2 Characterization of the inflow uncertainty

The objective is to quantify the effect of inflow uncertainty in the experiment by performing an ensemble of LES simulations. Specifically, the uncertainty in the experiment will have an effect on the definition of the target profiles of the optimization procedure, which will result in uncertainty in the pressure distribution around the building. We characterize the inflow uncertainty by considering the spanwise variation in the measured profiles for mean velocity, turbulence kinetic energy and streamwise integral time scales, as shown by the grey shaded areas in Figure 5.2. Subsequently, three different profiles are defined for each of these quantities, covering the range of the measured values.

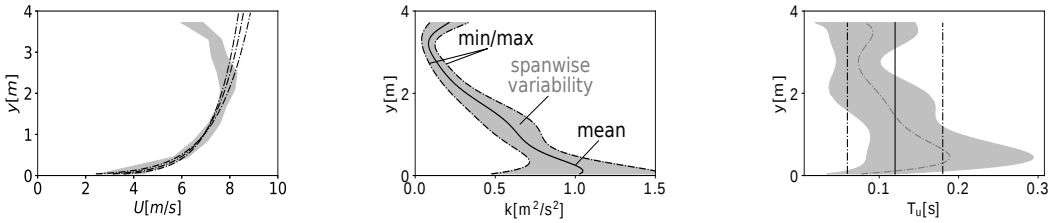

(a) Mean streamwise velocity (b) Turbulence kinetic energy (c) Streamwise integral time scale

Figure 5.2: ABL profiles for the inflow sensitivity analysis.

The mean velocity profile is prescribed using the log-law, which is determined by two independent parameters: a reference velocity and the roughness length of the terrain z_0. Since we can expect the pressure coefficients to be Reynolds number independent, we select z_0 as the uncertain parameter. By fitting a logarithmic profile to the measurements at each spanwise location, we define an upper and lower limit and a mean value for z_0; the resulting mean velocity profiles are shown in Figure 5.2a. These profiles are used to define U_i in Equation 4.1; by using a wall function that represents the effect of the roughness length of the terrain [97, 87] we ensure that the shape of the inlet profile is maintained throughout the domain [65].

The three profiles for the turbulence kinetic energy are defined by considering the minimum, mean and maximum values from the measurements. To compensate for the turbulence decay commonly observed when using digital filter methods, we first perform simulations for an empty domain with the optimization algorithm proposed in Chapter 4 [65]. The optimization procedure adjusts the input parameters for the inflow generator until the desired statistics are obtained at the location of interest. In particular, to achieve turbulence intensities at the building location that closely represent the experimental values, the algorithm modifies the spanwise ($\overline{w'^2}$) and vertical ($\overline{v'^2}$) components of the Reynolds stress tensor imposed at the inflow. The optimization was performed for the mean values of z_0 and the integral time scale (discussed next), providing three sets of inputs for a_{ij} in Equation 4.1 that can represent the three profiles plotted in 5.2b.

The last term in Equation 4.1 is the fluctuation term $u_{*,j}$, which is a function of the turbulence integral length and time scales. Since the spatial resolution of the hot-wire measurements is insufficient to compute 2-point correlations, we used Taylor's hypothesis [121] to compute the integral length scales [65]. The streamwise integral time scale T_u was then selected as the third uncertain parameter. Upper and lower bounds, and the mean value for the parameter are shown in Figure 5.2c; in this case the inflow algorithm requires a constant value over height [65]. The resulting values for T_u are directly used to specify the temporal correlation of $u_{*,j}$ at the inlet. It is noted that some streamwise inhomogeneity in the time scales has been observed. This variation is more challenging to control using the optimization, in part because the value specified at the input can also affect the downstream level of turbulence kinetic energy. This interaction will be quantified in section 5.2.2, and it will be taken into account when interpreting the results for the pressure coefficients.

In summary, we represent the uncertainty in the inflow conditions using three parameters: the roughness length of the terrain z_0, the turbulence kinetic energy k and streamwise integral time scale T_u. The spanwise variation of the experiment was used to characterize these uncertain parameters, defining upper and lower bounds and mean values. All possible combinations of the selected parameter values define 27 inflow conditions; therefore, we perform the corresponding 27 LES simulations to study the effect of the inflow uncertainty on the results.

5.2 Results

In this section, we first present an initial analysis of the LES simulation with the mean inflow parameters. This analysis focuses on comparing the spectra and characteristics of the time series and peak events of the pressure coefficients to the wind tunnel data to confirm that the energy-containing turbulence scales are sufficiently resolved by the LES. Subsequently, we analyze the ABL velocity statistics at the building location in all 27 LES, to confirm that the ensemble of simulations can represent the uncertainty in the inflow conditions of the wind tunnel experiment. Finally, we present the results for the pressure coefficients obtained from the ensemble of LES. Predictions for the mean, rms, peak and design pressure coefficients are compared to the wind tunnel data for validation, and analyzed to identify the relative importance of the uncertain inflow parameters.

5.2.1 Baseline LES

Figure 5.3 shows an instantaneous snapshot of the velocity field obtained from the baseline LES simulation with the mean inflow parameters. Turbulent structures are produced at the inflow generation plane and advected downstream to the building model. A stagnation region is formed just upstream of the windward facade; there is separation on the lateral facades and a wake forms behind the building. The top view of Figure 5.3 indicates the presence of vortex shedding, but the high turbulence intensity of the inflow prevents pronounced periodic behavior. The remainder of this

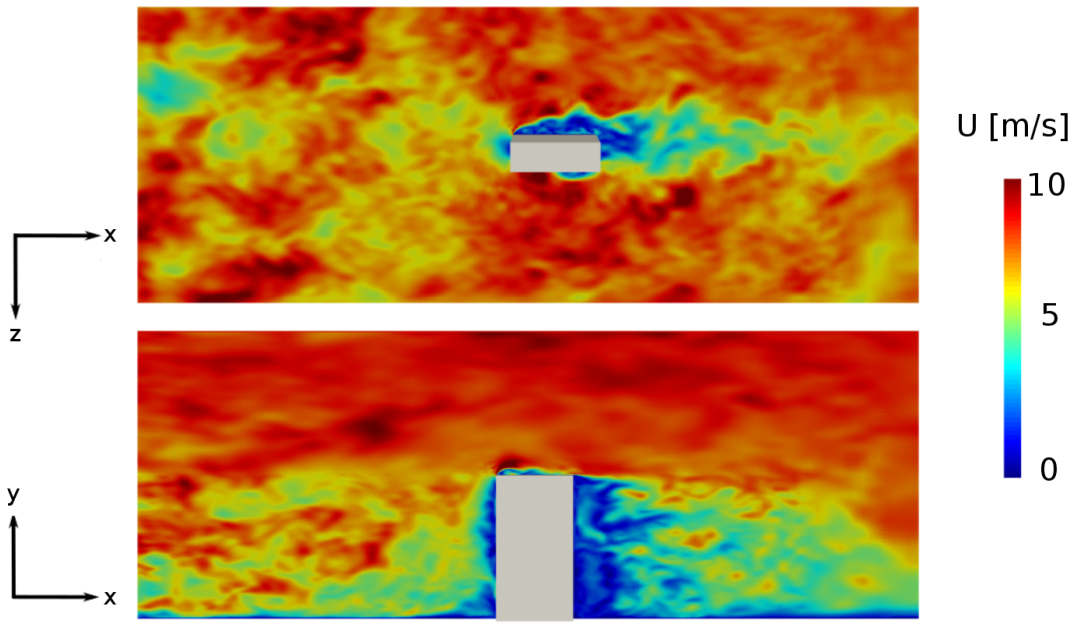

Figure 5.3: Instantaneous velocity field from the baseline LES simulation.

section analyzes the predictions for the pressure coefficients on the building lateral facade, to verify that the LES can adequately resolve the turbulent wind pressure field. First, we present pressure spectra and time-series of pressure coefficients, measured at pressure taps in locations where strong negative pressure peaks occur. Subsequently, contours of instantaneous C_p over a panel next to the top corner of the building during a pressure peak event are plotted, and related to the presence of coherent turbulence structures in the flow.

Figure 5.4 shows the non-dimensional power spectra of the pressure coefficient measured at four pressure taps near the corners of the building, computed using Welch method [128]. The result of the baseline LES is compared to the wind tunnel measurements. The spectra compare well in the energy-containing range and in the first part of the inertial subrange. At non-dimensional frequencies $\frac{fB}{U} > 1$ (where f is the dimensional frequency, B the width of the building and U the reference velocity at roof height), the energy in the LES simulation drops, indicating that these higher frequencies cannot be resolved. The pressure tap at mid-height near the downwind corner of the model (Figure 5.4f), exhibits a peak in the power spectrum of both the experiment and the LES, at $\frac{fB}{U} \sim 0.15$; this is likely related to vortex shedding.

Figure 5.5 plots a 50s time-series of the pressure coefficient recorded at a pressure tap next to the windward top corner of the building; this is where the strongest suction peaks occur for the wind direction under consideration. The two time-series exhibit very similar behavior, characterized by the occurrence of several negative peaks of pressure coefficient. Specifically, 6 and 3 peaks lower than

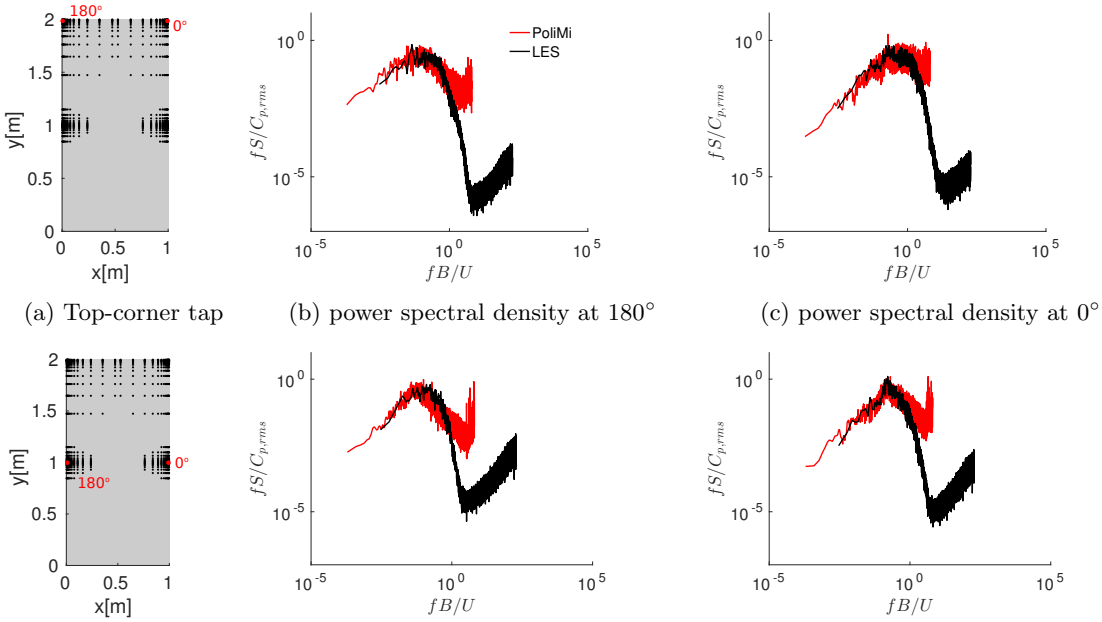

(a) Top-corner tap (b) power spectral density at 180° (c) power spectral density at 0°

(d) Mid-edge tap (e) power spectral density at 180° (f) power spectral density at 0°

Figure 5.4: Power spectral density on top-corner and mid-edge taps.

$C_p = -2$ are experienced in the LES and the experiment respectively. The strongest negative peak recorded by the selected pressure tap is ~ -2.8 in the LES and ~ -2.7 in the experiment. When considering the full 300s duration of the experiment, the largest negative peak measured at the same pressure tap is ~ -3.5. In section 5.2.3, the peak values for a 22% probability of exceedance will be calculated using the Cook and Maine method to enable a statistically meaningful comparison of the peak values.

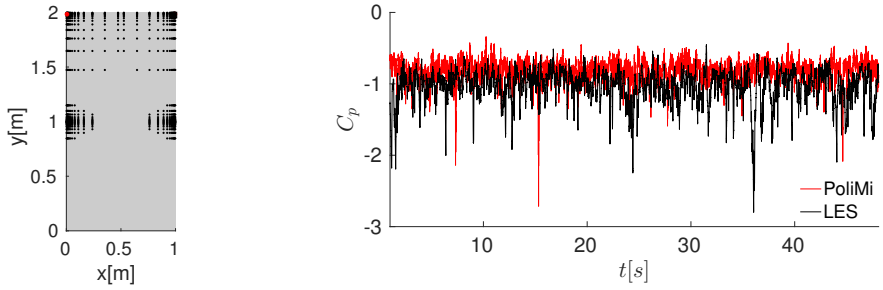

(a) Top-corner tap (b) Time-series of C_p

Figure 5.5: Time-series of pressure coefficient on top-corner tap.

To visualize the nature of the pressure peak events, Figure 5.6 shows the distribution of the

instantaneous C_p near the windward upper corner of the building during a peak event. The time-series of C_p measured by two taps near the location of the peak event are also plotted and compared to the area-averaged C_p of a $2 \times 3\text{m}^2$ panel. The plots demonstrate the similar nature of the pressure peak events in the wind tunnel experiment and the LES simulation. A region of pressure coefficients lower than -2.5 appears next to upper corner of the windward edge of the building, around the same pressure tap (*tap1*). The time-series of C_p measured by *tap1* reaches a negative value of ~ -2.8, in both the LES and the experiment (Figures 5.6b and 5.6e). The duration of the peak event is ~ 395ms in the LES simulation, while it is $\sim 188ms$ in the experiment. The LES signal is smoother than the experimental one, which confirms the observation from the spectra (Figure 5.4) that the LES cannot resolve the smallest turbulent scales observed in the experiment. When calculating the area-averaged values of C_p, the peak values drop from ~ -1 to ~ -1.6 in both the LES and the experiment; this indicates the importance of considering the pressure loads averaged over an area of interest in addition to the local peak values.

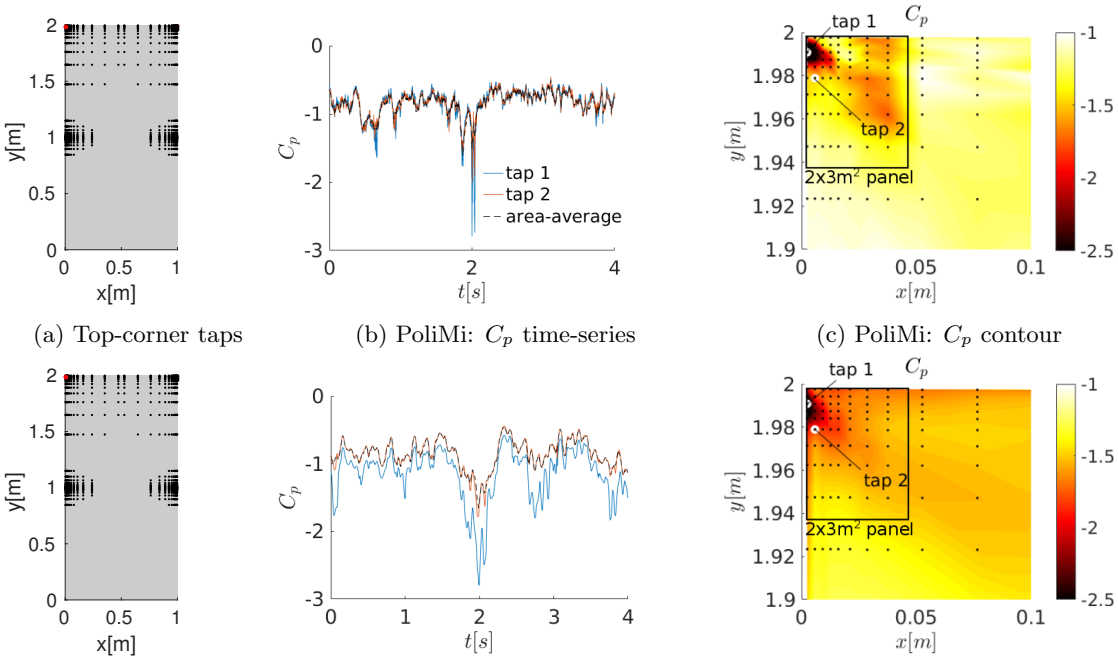

(a) Top-corner taps (b) PoliMi: C_p time-series (c) PoliMi: C_p contour

(d) Top-corner taps (e) LES: C_p time-series (f) LES: C_p contour

Figure 5.6: Time-series of pressure coefficient on top-corner tap and pressure coefficient distribution on the tile at the time instant of the negative peak.

Lastly, Figure 5.7 relates the peak pressure events to the flow features by plotting the instantaneous C_p distribution on the entire side wall together with the simultaneous contour of the second invariant of the velocity gradient tensor Q [39]. Coherent structures corresponding to $Q = 2,000\text{s}^{-2}$ are presented and colored by the instantaneous C_p. They visualize how the shear layer, formed

near the upwind corner of the model, separates and rolls up into large vortices, which cause regions of relatively strong suction further downstream [100]. This effect is strongest near the top of the building, where the interaction between shear layers originating from the upwind and top edges generates the highest suctions.

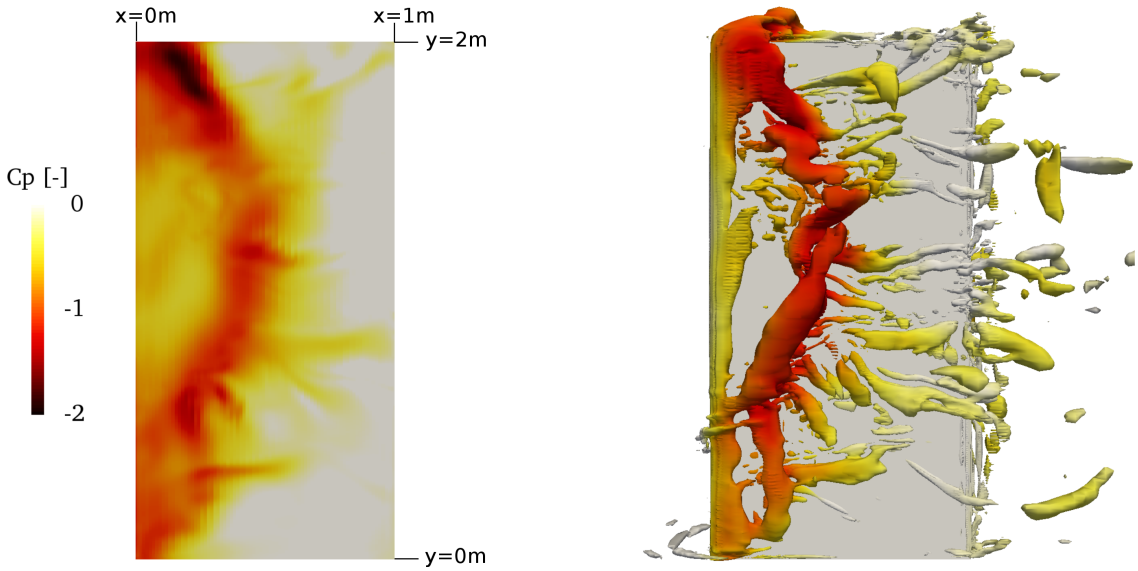

Figure 5.7: Contours of instantaneous pressure coefficient and iso-surface of the second invariant of the velocity gradient tensor $Q = 2,000\text{s}^{-2}$, colored by the instantaneous pressure coefficient.

5.2.2 Velocity statistics

In Figure 5.8, we compare the 27 LES results for the turbulent velocity statistics at the building location to the wind tunnel measurements. The spread of the profiles is significant, especially in terms of the turbulence kinetic energy and integral time scale (Figures 5.8b and 5.8c). The ensemble of LES profiles provides a good representation of the spanwise variation in the wind tunnel experiment above 0.25m height. Closer to the ground, the turbulence kinetic energy is underpredicted, while the integral time scales are overpredicted. The former can be explained by the fact that the experimental uncertainty in the turbulence kinetic energy significantly increases next to the ground, while the latter by the fact that the inflow generation method assumes profiles of integral time scales that are constant over height. The behavior is similar to the one observed in [65]

To identify the main effect associated with each input parameter, Figure 5.9 shows the profiles obtained by averaging the results of the simulations that have a fixed value for one of the uncertain inflow parameters. For example, in the top row of Figure 5.9, the blue profiles are obtained by averaging the results of the 9 simulations that use the minimum value for the roughness length;

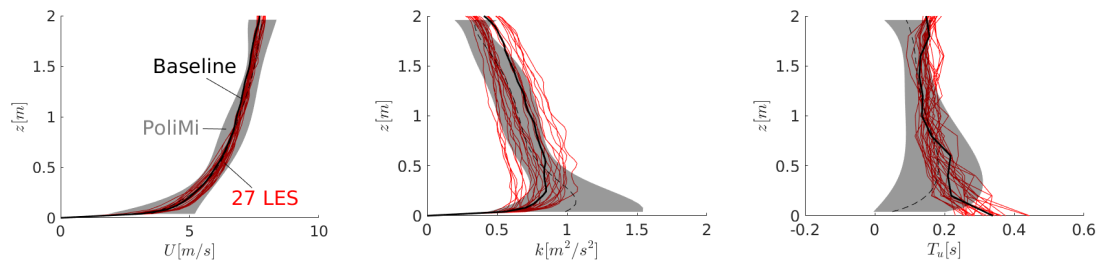

(a) Mean streamwise velocity (b) Turbulence kinetic energy (c) Streamwise integral time scale

Figure 5.8: Turbulence statistics at the building location from the ensemble of LES.

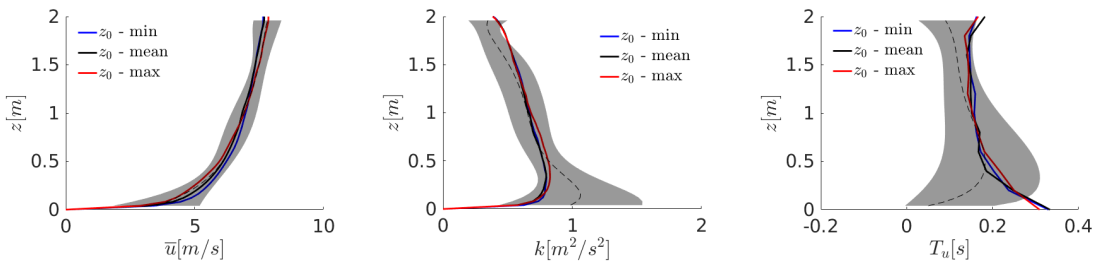

(a) Mean streamwise velocity: effect of z_0 (b) Turbulence kinetic energy: effect of z_0 (c) Streamwise integral time scale: effect of z_0

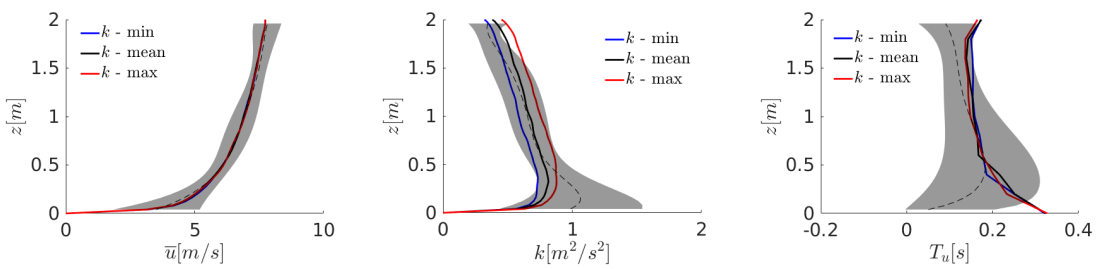

(d) Mean streamwise velocity: effect of k (e) Turbulence kinetic energy: effect of k (f) Streamwise integral time scale: effect of k

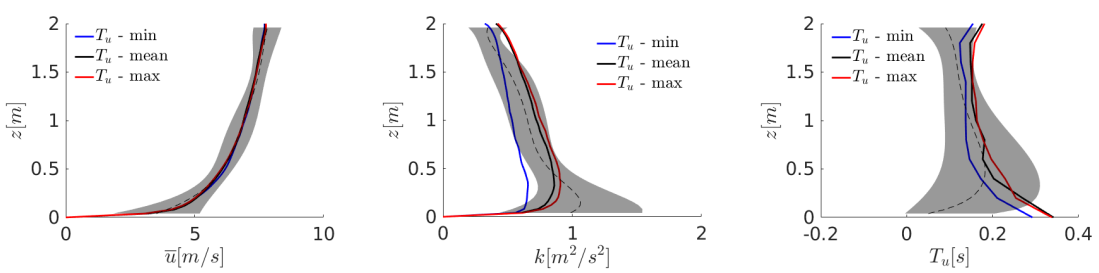

(g) Mean streamwise velocity: effect of T_u (h) Turbulence kinetic energy: effect of T_u (i) Streamwise integral time scale: effect of T_u

Figure 5.9: Effect of the different uncertain inflow parameters on the turbulence statistics at the building location. The profiles are obtained by averaging the results of the simulations with a fixed value for one of the parameters, reported in the corresponding label in the legend.

similarly, the black and red profiles represent the average of the velocity statistics across the 9 simulations with the mean and maximum values for z_0, respectively. In the mid and bottom rows of Figures 5.9, analogous plots are obtained for different inflow values of the turbulence kinetic energy and the integral time scale.

The roughness length of the terrain produces the expected effect on the mean velocity profiles (Figure 5.9a): lower roughness corresponds to higher velocity next to the ground. The terrain roughness has almost no effect on the velocity fluctuations at the building location, as evident from the almost overlapping profiles of Figures 5.9b and 5.9c. In contrast, the turbulence kinetic energy and integral time scale specified at the inflow have a negligible effect on the mean velocity profiles (Figures 5.9d and 5.9g), but they affect the turbulence characteristics at the building. Figures 5.9e and 5.9f indicate that the level of turbulence kinetic energy can be modified without affecting the integral time scales, while Figures 5.9f and 5.9i show that the integral time scale has a strong interaction effect. This interaction effect should be taken into account when analyzing the results; any variation in the results between the simulations with different time scales is likely to be strongly affected by the corresponding variation in turbulence kinetic energy at the building location. All observed effects are monotonic: a higher turbulence kinetic energy or time scale at the inflow results in higher values further downstream. For the integral time scale there appears to be an upper limit, since an inflow value higher than the experimental mean has little effect on the turbulence statistics further downstream.

5.2.3 Pressure statistics

Mean pressure coefficient

Figure 5.10 shows the mean pressure coefficient distribution on the building's lateral facade from the wind tunnel experiment and the baseline LES. To quantify the sensitivity to the inflow conditions, the discrepancy between the minimum and maximum values recorded across the 27 LES simulations is shown. The wind tunnel and LES data exhibit the same qualitative features: the flow separates at the windward edge of the building, generating a region of relatively strong suction in the separated flow region (red region of Figures 5.10a and 5.10b); further downstream, the flow reattaches, reducing the strength of the suction (yellow region of Figures 5.10a and 5.10b). The maximum difference in the C_P values predicted from the ensemble of LES simulations occurs in the separation region, next to the top edge, where it reaches ~ 0.16 (Figure 5.10c). This corresponds to a $\sim 20\%$ difference in the predicted mean C_p in this region, indicating that the uncertainty in the inflow conditions has a non-negligible effect on the mean pressure distribution in regions of flow separation

To provide a more quantitative comparison, profiles of the mean pressure coefficient along two rows of taps on the top portion of the model are plotted in Figure 5.11. The baseline LES result and the sensitivity interval, i.e. the minimum and maximum values across the 27 LES simulations, are compared to the wind tunnel measurements. The ensemble of LES simulations seems to slightly

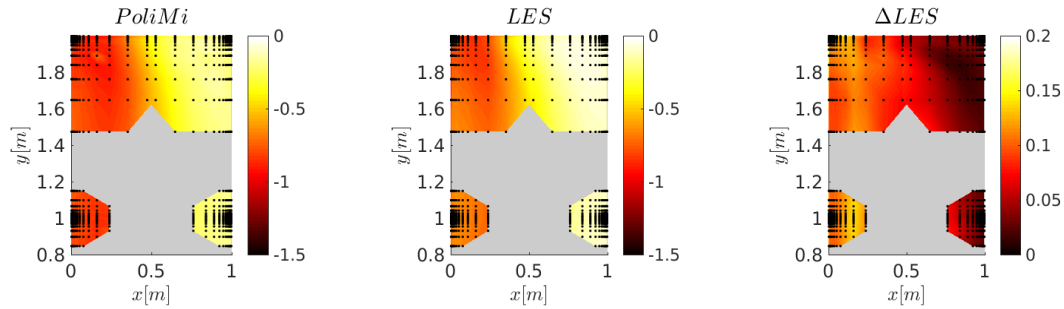

(a) Wind tunnel (b) Baseline LES (c) Maximum discrepancy

Figure 5.10: Mean pressure coefficient distribution on the building's lateral facade.

under-predict the magnitude of the mean C_p (Figure 5.11); the maximum discrepancy between the minimum value of the sensitivity interval and the measurements along the rows of taps considered, is 0.09 on tile A (Figure 5.11a) and 0.12 on tile B (Figure 5.11b). The size of the sensitivity intervals confirms that the mean C_p is more sensitive to the inflow uncertainty in the regions of flow separation; in the rear portion of the model, where the flow is attached, the inflow uncertainty has a negligible effect on the quantity of interest.

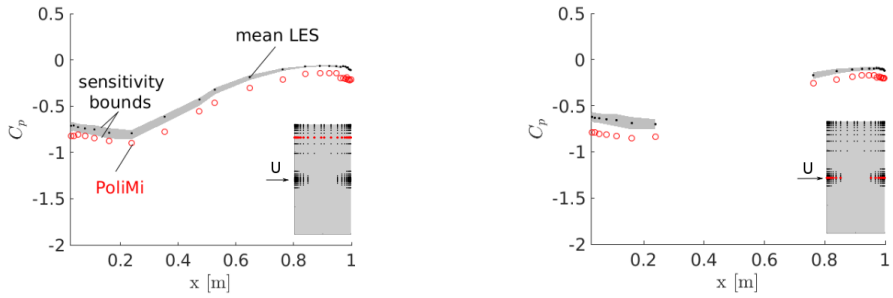

(a) Profiles of C_P (b) Profiles of C_P

Figure 5.11: Mean pressure coefficient profiles: baseline LES (black dots) and sensitivity intervals (gray area) compared to the wind tunnel data (red circles).

To identify the main effect associated with each uncertain inflow parameter, Figure 5.12 shows the profiles of the mean pressure coefficients obtained by averaging across simulations that have a fixed value for one of the uncertain inflow parameters. Figures 5.12a and 5.12b compare profiles of C_P averaged across the simulations with the same values of z_0. The largest effect of the roughness length occurs inside the separation region, where C_P experiences a maximum variation of ~ 0.06 (i.e. $\sim 8\%$), in both rows of taps considered. In general, lower values of z_0 are associated with higher negative values of mean C_p. The sensitivity of the mean C_p on the turbulence kinetic energy and integral time scale appears negligible.

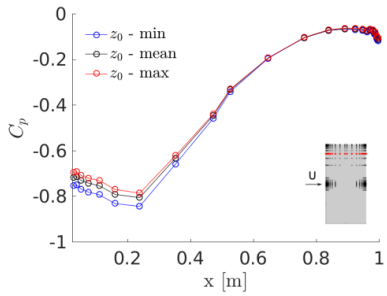

(a) Effect of z_0 on tile A

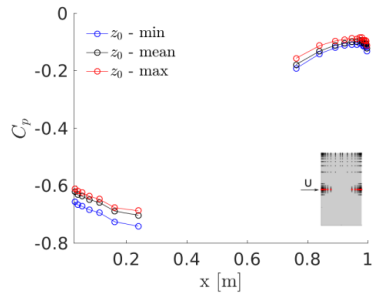

(b) Effect of z_0 on tile B

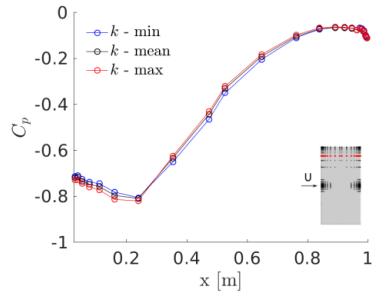

(c) Effect of k on tile A

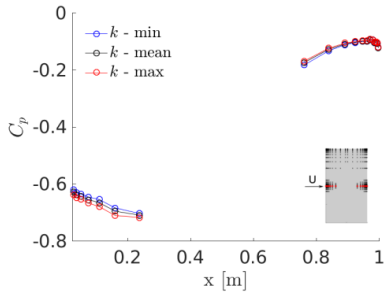

(d) Effect of k on tile B

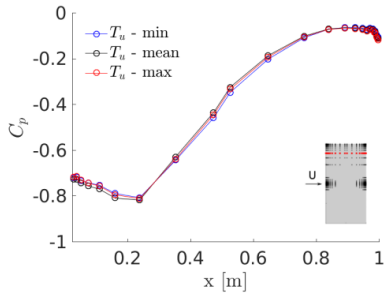

(e) Effect of T_u on tile A

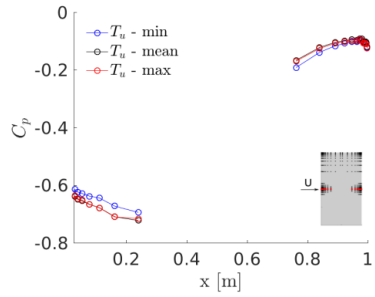

(f) Effect of T_u on tile B

Figure 5.12: Effect of the different uncertain inflow parameters on the mean pressure coefficient profiles. The profiles are obtained by averaging the results of the simulations with a fixed value for one of the parameters, reported in the corresponding label in the legend.

Rms pressure coefficient

Figure 5.13 plots the distribution of the rms pressure coefficient. Both the experiment and the baseline LES manifest an increase in C_p' where reattachment occurs in the mid portion of the model (Figures 5.13a and 5.13b). The highest value of C_p' occurs near the upper edge of the model, where a maximum value of ~ 0.29 and ~ 0.31 are computed by the experiment and baseline LES, respectively. The maximum discrepancy across the ensemble of 27 LES, shown in Figure 5.13c, is again largest inside the separation region. The plots indicate that the inflow parameters have stronger influence on C_p', compared to the mean C_p: the maximum variation of ~ 0.16 across the 27 LES simulations corresponds to $\sim 50\%$ difference.

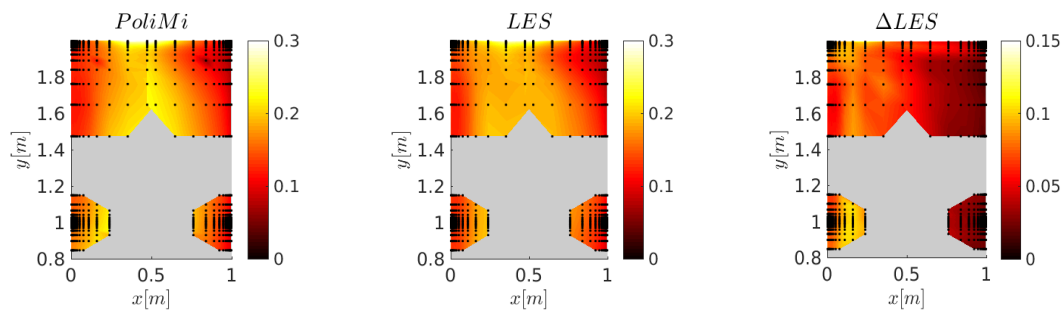

(a) Wind tunnel (b) Baseline LES (c) Maximum discrepancy

Figure 5.13: Rms pressure coefficient distribution on the building's lateral facade.

Figure 5.14 further quantifies the results, showing rms pressure coefficient profiles along the two rows of taps on tiles A and B. The baseline LES and the sensitivity intervals are compared to the wind tunnel measurements. The C_p' obtained in the PoliMi experiment is fully encompassed by the LES sensitivity intervals in both rows of taps considered. The size of the intervals confirms the high sensitivity of the rms pressure coefficients to the inflow uncertainty. The effect is larger inside the separation and reattachment regions of the flow, compared to the rear portion of the model, where the flow is attached. However, differently from the mean C_p, the effect of the inflow uncertainty on the rms C_p appears non-negligible in all locations.

To identify the main effect associated with each uncertain inflow parameter, Figure 5.15 again shows the profiles obtained by averaging across simulations that have a fixed value for one of the uncertain inflow parameters. Figures 5.15a and 5.15b compare profiles of C_p' averaged across the simulations with identical values of z_0. The profiles on tile A mostly overlap; the maximum variation is ~ 0.01 and occurs in the region of flow reattachment. On tile B, the the maximum difference is slightly higher (~ 0.02), and it arises in the rear portion of the model. Figures 5.15c and 5.15d show that the uncertainty in the turbulence kinetic energy primarily influences the C_p' in the front portion of the model, i.e. inside the separation region. Higher values of C_p' are associated with higher values of k, and the maximum variation across the profiles is ~ 0.03. The effect of k is negligible in the rear

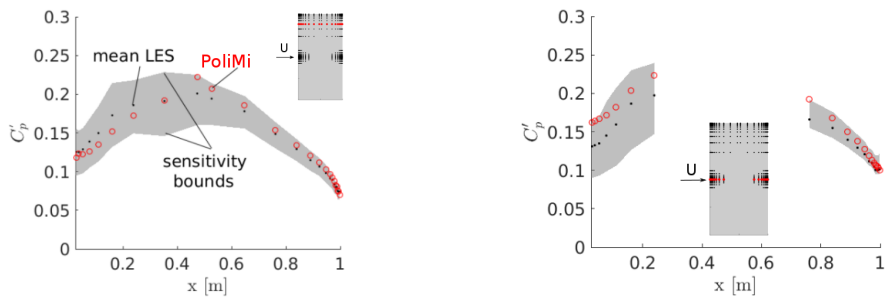

(a) Profiles of C'_p (b) Profiles of C'_p

Figure 5.14: Rms pressure coefficient profiles: baseline LES (black dots) and sensitivity intervals (gray area) compared to the wind tunnel data (red circles).

portion of the model, where the flow is attached. Lastly, Figures 5.15e and 5.15f indicate that the integral time scale imposed at the inflow causes the largest uncertainty in the C'_p, especially inside the separation region. This result has to be interpreted with care: Figures 5.9h and 5.9i indicate that the difference in C'_p is a result of the combination of the increased turbulence kinetic energy and the increased integral time scale at the location of the building. This combined effect indicates the importance of accurately quantifying the turbulence statistics at the building location in LES of wind loading.

Peak pressure coefficient

Figure 5.16 shows the distribution of the peak pressure coefficients relative to a 22% probability of exceedance. Figures 5.16a and 5.16b indicate qualitative good agreement between the experiment and the LES: the largest negative $\check{C}_p$ values are experienced inside the separation region and near the upper edge of the building. Quantitatively, the baseline LES under-predicts the magnitude of the peak pressure coefficients: the minimum $\check{C}_p$ is -2.5, compared to ~ -2.7 measured in the wind tunnel experiment. However, the minimum values of $\check{C}_p$ across the 27 LES simulations, shown in Figure 5.16c, reaches as negative values as the experiment, with a minimum $\check{C}_p$ of ~ -3.1. Figure 5.16d plots the local difference between the minimum and maximum values recorded across the 27 LES simulations. The largest uncertainty occurs inside the separation region and next to the upper edge of the building, i.e. in the regions that experience the highest pressure peaks. Here, the inflow uncertainty can cause variations in $\check{C}_p$ of up to ~ 1.14.

Figure 5.17 further quantifies these results by comparing $\check{C}_p$ profiles along two rows of taps on the building's side wall. The baseline result and the sensitivity intervals are compared to the wind tunnel measurements. The width of the sensitivity intervals indicates that the uncertainty in the inflow conditions significantly affects the $\check{C}_p$ prediction in all locations on the building's lateral facade. Overall, $\sim 60\%$ and $\sim 5\%$ of the data along the profiles on tiles A and B are encompassed by

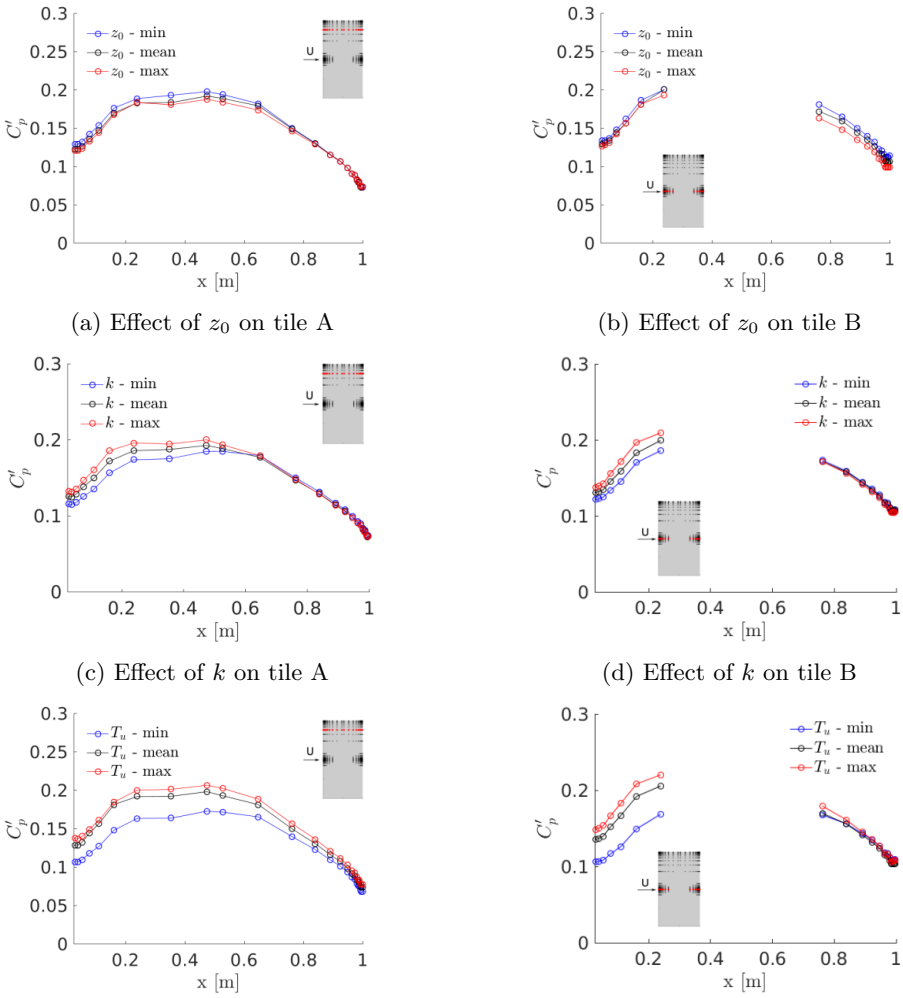

(a) Effect of z_0 on tile A

(b) Effect of z_0 on tile B

(c) Effect of k on tile A

(d) Effect of k on tile B

(e) Effect of T_u on tile A

(f) Effect of T_u on tile B

Figure 5.15: Effect of the different inflow parameters on the rms pressure coefficient profiles. The profiles are obtained by averaging the results of the simulations with a fixed value for one of the parameters, reported in the corresponding label in the legend.

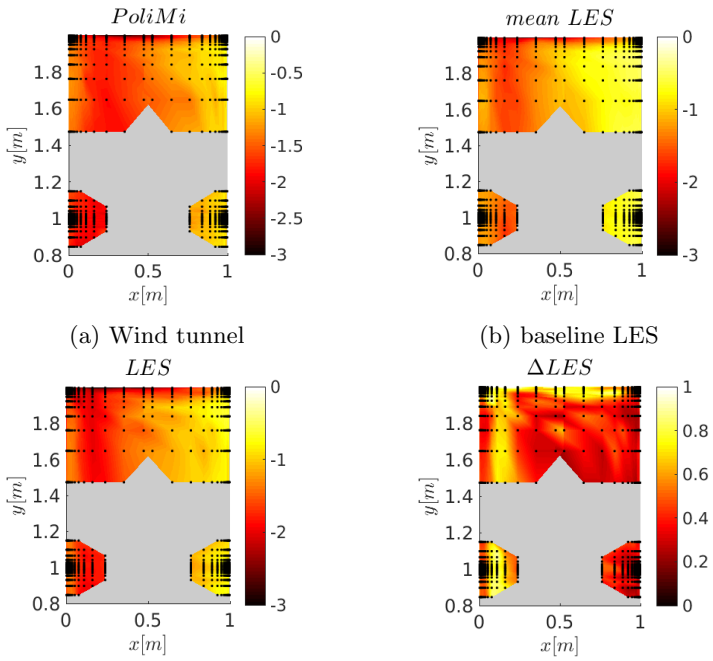

(a) Wind tunnel (b) baseline LES

(c) Minimum (d) Maximum discrepancy

Figure 5.16: Distribution of peak pressure coefficient relative to a 22% probability of exceedance on the building's lateral facade.

the sensitivity intervals, respectively. The highest discrepancy between the most negative interval bound and the experimental data is ~ 0.18 along the top row and ~ 0.35 along the mid row, which correspond to $\sim 15\%$ and $\sim 20\%$ of $\check{C}_p$, respectively. This under-prediction of the magnitude of local peak values should be expected, the combination of the filtering operation and numerical dissipation will decrease the peak values calculated from the resolved turbulent pressure signal.

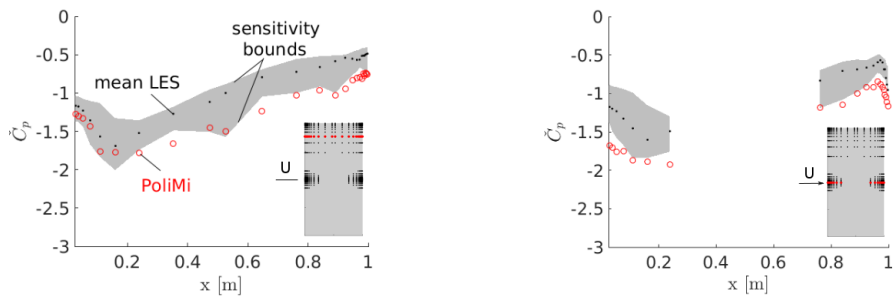

(a) Profiles of $\check{C}_p$ (b) Profiles of $\check{C}_p$

Figure 5.17: Profiles of peak pressure coefficient relative to a 22% probability of exceedance: baseline LES (black dots) and sensitivity intervals (gray area) compared to the wind tunnel data (red circles).

To identify the main effect associated with each uncertain inflow parameter, Figure 5.18 compares profiles of $\check{C}_p$ averaged across simulations that have a fixed value for one of the uncertain inflow parameters. The effect of the roughness length, shown in Figures 5.18a and 5.18b, is analogous to its effect on the mean pressure coefficient. Variations in z_0 can cause up to ~ 0.14 (i.e. $\sim 10\%$) variations in the $\check{C}_p$, inside the separation region of the flow. In general, lower z_0 values are associated with more negative values of $\check{C}_p$. Figures 5.18c, 5.18d, 5.18e and 5.18f indicate that the turbulence kinetic energy k and integral time scale T_u cause a maximum variation of ~ 0.18 and ~ 0.26, respectively. As for the rms C_p, higher values of k or T_u are associated with higher absolute values of peak pressure coefficient. Again, the effect of T_u has to interpreted with care: Figures 5.9h and 5.9i indicate that the difference in $\check{C}_p$ is a result of the combination of the increased turbulence kinetic energy and the increased integral time scale at the location of the building.

Design pressure coefficient

The point-wise values for $\check{C}_p$ are not the most relevant quantity of interest for cladding design; instead, the main quantity interest is the design pressure coefficient $\check{C}_{p,d}$ of the panels. $\check{C}_{p,d}$ can be calculated by applying the Cook and Mayne method [21] to the pressure coefficient averaged over the panel area. Figure 5.19 plots the resulting extreme value distributions of C_p averaged over a typical $2 \times 3\text{m}^2$ panel, at the top-windward corner of the model, i.e. the most critical region for the considered wind direction. The spread of the cumulative density functions (CDFs) of Figure 5.19, highlights the importance of the uncertainty in the inflow conditions. The resulting horsetail plot,

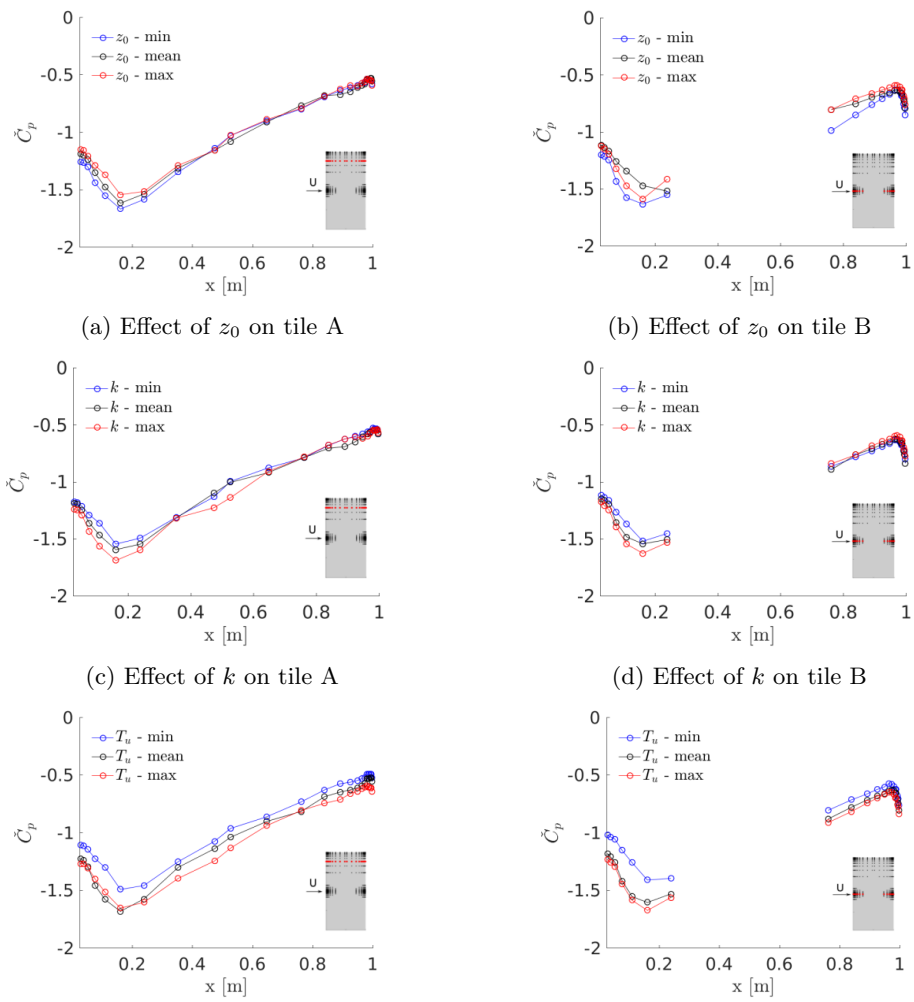

(a) Effect of z_0 on tile A

(b) Effect of z_0 on tile B

(c) Effect of k on tile A

(d) Effect of k on tile B

(e) Effect of T_u on tile A

(f) Effect of T_u on tile B

Figure 5.18: Effect of the different inflow parameters on the peak pressure coefficient profiles. The profiles are obtained by averaging the results of the simulations with a fixed value for one of the parameters, reported in the corresponding label in the legend.

formed by the ensemble of LES distributions, fully encompasses the experimental distribution. This means that the ensemble of LES can provide an upper and lower bound on the measurement result for any desired probability of exceedance.

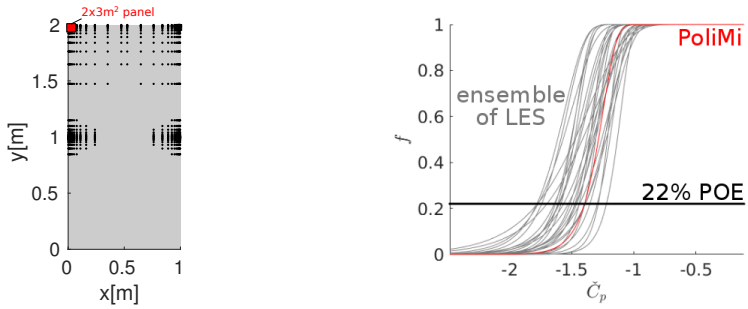

(a) $2 \times 3\text{m}^2$ panel on top corner (b) Extreme value distributions of $C_{p,AA}$

Figure 5.19: Cumulative density functions of the extreme values of the pressure coefficient averaged over a $2 \times 3\text{m}^2$ panel.

Lastly, Figure 5.20b shows the design pressure coefficient relative to a 22% probability of exceedance for panels of increasing dimension, located at the top-windward corner of the building (Figure 5.20a). For all panel sizes considered, the design pressure coefficient is within the sensitivity intervals predicted by the LES. The magnitude of $\check{C}_{p,d}$ decreases with increasing panel area, meaning that the area-averaging procedure is increasingly filtering out strong and localized pressure peaks. These results for $\check{C}_{p,d}$ demonstrate that the effects of the filtering operation and any numerical dissipation in the LES do not deteriorate the prediction of the main quantity of interest for cladding design.

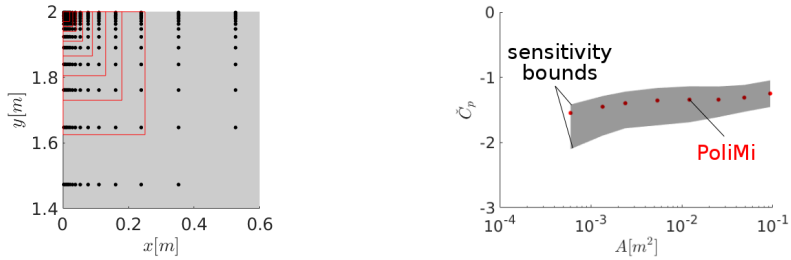

(a) Panels on tile A (b) Profiles of design C_p

Figure 5.20: Design pressure coefficients as a function of panel size.

To identify the main effect of each individual uncertain inflow parameter, Figure 5.21 compares the values for $\check{C}_{p,d}$ as a function of panel size, computed by averaging the results across the simulations that have a fixed value for one of the inflow parameters. The uncertainty in the roughness length z_0 can cause up to ~ 0.27 variation in $\check{C}_{p,d}$. The trend is similar to that observed for the

peak pressure coefficient: lower terrain roughness is associated with higher absolute values of $\check{C}_{p,d}$. Variations in turbulence kinetic energy produce a maximum variation of ~ 0.16 for the selected panel sizes, while the effect of changing the turbulence integral time scale at the inflow causes a maximum variation of ~ 0.22. As before, higher values of the turbulence kinetic energy and integral time scale at the inflow result in higher absolute values of $\check{C}_{p,d}$; once again, the difference in $\check{C}_{p,d}$ due to a change in the inflow value of T_u is the result of a combination of the increased turbulence kinetic energy and the increased integral time scale at the location of the building.

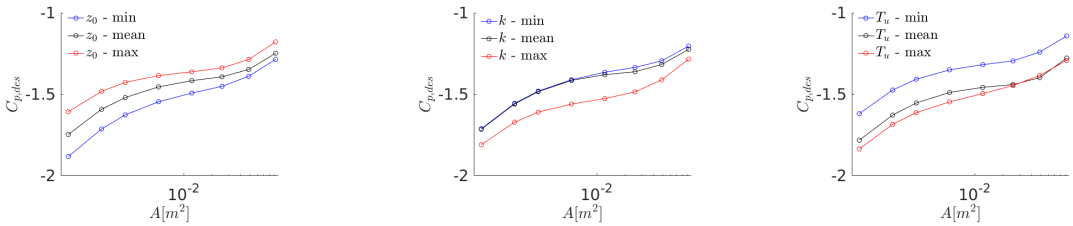

(a) Effect of z_0 (b) Effect of k (c) Effect of T_u

Figure 5.21: Effect of the different inflow parameters on the design pressure coefficient profiles. The profiles are obtained by averaging the results of the simulations with a fixed value for one of the parameters, reported in the corresponding label in the legend.

5.3 Summary

The chapter investigated the effect of uncertainty in the inflow boundary conditions on the pressure distribution on a high-rise building. We identified three uncertain parameters: the roughness length of the terrain, the turbulence kinetic energy and the streamwise integral time scale. By analyzing measurements performed at different spanwise locations, we defined minimum, mean and maximum values for these three parameters, resulting in 27 different inflow conditions.

Initial analysis of the baseline LES indicated that the LES did not capture as small scales as the experiment, but produced strong negative pressure peaks with a similar magnitude and spatial characteristic. Simultaneous visualizations of the instantaneous pressure coefficient distribution and coherent structures in the flow showed a correlation between peak events and the presence of turbulent structures.

Subsequently, we analyzed the effect of the inflow conditions on the turbulence statistics at the building location. It was shown that the 27 simulations were representative of the uncertainty in the wind tunnel measurements. The terrain roughness length primarily affected the mean velocity at the building location, while the turbulence kinetic energy and integral time scale at the inflow, primarily affected the velocity fluctuations. Importantly, changes in the integral time scale at the inflow were shown to affect both the value of the turbulence kinetic energy and the integral time scale at the building location.

The comparison of the mean and rms pressure coefficients showed good agreement between the experiment and numerical simulations, despite a slight under-estimation of the magnitude of the mean pressure coefficient. Within the uncertain parameters, the roughness length primarily affected the mean pressure coefficients, while the turbulence kinetic energy and integral time scale primarily affected the rms pressure coefficients. In particular, lower terrain roughness was associated with more negative mean C_p, while larger turbulence kinetic energy and integral time scale produced higher rms C_p. In both cases, the effects were stronger in the separation region and near the point of reattachment. It was noted that the effect of the integral time scale on the rms pressure coefficients was a result of the combination of the increased turbulence kinetic energy and the increased integral time scale at the location of the building. This combined effect indicated the importance of accurately quantifying the turbulence statistics at the building location, rather than at the inflow, in LES of wind loading.

Lastly, we performed extreme value analysis to compute the distribution of the peak pressure coefficient on the building's facade, and the design pressure coefficients for cladding panels of different size. By accounting for the uncertainty in the inflow conditions, the LES predicted as negative values of the peak C_p as the experiment, although the magnitude of the local peak pressure coefficients was on average under-predicted by 12%. This under-prediction can be explained by the effect of the filtering operation and numerical dissipation in the LES. When considering design pressure coefficients on cladding panels of different sizes located at the upper-windward corner of the building, these effects became less important: the LES sensitivity analysis provided intervals that encompassed the experimental result. All inflow parameters significantly contributed to the uncertainty in the peak and design pressure coefficients. The importance of the roughness length can be explained by its effect on the mean pressure coefficient, while the effect of the turbulence kinetic energy and the integral time scale was analogous to their effect on the rms C_p.

In summary, uncertainties in the ABL statistics, such as those occurring during well controlled wind tunnel experiments, can cause significant uncertainty in the pressure distribution on high-rise buildings. By accurately characterizing the ABL at the building location and accounting for these uncertainties, the confidence in LES for wind loading could drastically increase.

Chapter 6

RANS: inflow and turbulence model UQ

The previous chapters demonstrated that, by properly generating the inflow conditions and by accounting for the inherent uncertainty in the definition of the inflow parameters, LES can provide accurate prediction of the QoIs for cladding design. Nonetheless, we only considered one wind direction, while wind loading design usually requires to resolve the full wind rose with a 10° resolution [51], making the LES framework extremely expensive, especially for the early design phases. For this reason, RANS simulations still represent an attractive tool, despite their limitations.

In order to improve the confidence in the RANS prediction of the mean pressure coefficient around the building, this chapter presents a framework to quantify the combined effect of inflow and turbulence model uncertainties. To characterize the uncertainty in the inflow conditions, two uncertain parameters are defined: the roughness length of the terrain and the model orientation. Probability distributions for these parameters are determined using information from the wind tunnel experiment, and propagated to the QoIs using a polynomial chaos expansion (PCE) approach [129]. The uncertainty in the turbulence model is quantified by introducing perturbations in the eigenvalues of the normalized Reynolds stress anisotropy tensor [30, 50, 37]. To combine these methods and propagate both the stochastic inflow uncertainty and the turbulence model-form uncertainty to the QoIs, we use a second-order probability framework [118].

The remainder of this chapter is organized as follows. The methodology is introduced in Section 6.1, discussing the CFD simulation set-up, the inflow and turbulence model UQ methods and the second-order probability method. Section 6.2, presents results for two wind directions, namely 0° and 20° (see Figure 3.2). These wind directions were selected as starting point, following the conclusions of previous studies [4]; the next chapters will extend the framework to include the entire wind rose.

6.1 Methods

In this section, the set-up of the RANS simulations is described. Subsequently, we introduce the methodology used to quantify the inflow uncertainty, focusing on the definition of the uncertain inflow parameters, and on the propagation method. Finally, the method used to quantify the turbulence model uncertainty is summarized.

6.1.1 CFD model

The simulations are performed using the simpleFOAM solver of OpenFOAM v4.0. The computational domain has the same dimensions as the test section of the PoliMi wind tunnel (see Chapter 3). The mesh includes refinement regions close to the building model, resulting in a total number of 3.7 million hexahedral cells. The resolution on the building's surface is 25mm, 12.5mm and 6.25mm in the streamwise, spanwise and vertical directions, respectively; the resulting y^+ is 500 on average. A grid dependency study was performed against a finer mesh composed by 6.2 million cells. The coefficient of determination R^2 between the mean pressure coefficient computed with the two meshes in all pressure taps was 0.98, confirming the quality of the selected mesh size and resolution.

We employ the RNG $k-\epsilon$ model together with a standard log-law wall function on the building surface. To properly represent the neutral ABL, the inlet boundary condition specifies a logarithmic velocity profile [97]:

$$U = \frac{u_\star}{\kappa} \ln\Big(\frac{z+z_0}{z_0}\Big), \tag{6.1}$$

where U is the mean velocity, $u_\star$ the friction velocity, κ the von Karman constant, z the height above the ground, and z_0 the roughness length. $u_\star$ and z_0 are found by fitting the logarithmic profile to the measurements. The corresponding inlet boundary condition for the turbulence kinetic energy is constant with height and the turbulence dissipation profile is defined to balance production of turbulence kinetic energy [97]:

$$k = \frac{u_\star^2}{\sqrt{C_\mu}}, \qquad \epsilon = \frac{u_\star^3}{\kappa\,(z+z_0)}. \tag{6.2}$$

To ensure horizontal homogeneity of these profiles throughout the domain, we use a modified wall function on the ground wall to represent the effect of the roughness length of the terrain [97, 87]. On the side boundaries we impose the same neutral ABL velocity and turbulence profiles as at the inflow, while on the top boundary we impose a slip boundary condition. The outlet is treated as a pressure-outlet with constant relative pressure equal to zero and a zero-gradient boundary condition for the other flow variables. To perform RANS simulations at different wind directions, we simply modify the velocity components imposed at the inflow, while maintaining the same computational domain and mesh. The momentum and turbulence model equations are discretized using second order numerical schemes and iteratively solved using a linear solver with a symmetric Gauss-Seidel smoother. The Poisson equation is approximated with second order schems and solved using the

generalised geometric-algebraic multi-grid (GAMG) solver with Gauss-Seidel smoother. To monitor convergence, we select 40 pressure taps (i.e. 10 per pressure tile of the PoliMi experiment) and run the simulations until the corresponding mean pressure coefficients stopped varying; specifically most simulations converged in $3,000$ to $5,000$ iterations.

6.1.2 Inflow UQ

Characterization of the inflow uncertainty

In order to characterize the uncertainty in the inflow conditions, we consider the spanwise variation of the profiles of mean velocity and turbulence kinetic energy, similarly to what was done in Section 5.1.2. Therefore, we identify the roughness length z_0 as the first uncertain parameter; by fitting a logarithmic profile to the measurements at each spanwise location, we can define upper and lower limit and assume that the roughness length is uniformly distributed within these bounds.

In addition to defining uncertainty in the roughness length, we account for potential misalignment between the intended and actual model orientation in the wind tunnel. To represent this uncertainty, we introduce a second parameter representing the angle of misalignment, α, assumed to be following a uniform distribution between -2° and 2°. The resulting uncertain parameters and their minimum, mean and maximum values are summarized in Table 6.1.

	Min.	Mean	Max.
z_0 [mm]	1.3	4.2	7.1
α [°]	-2	0	2

Table 6.1: Inflow uncertain parameters.

Propagation method

To propagate the inflow uncertainties to the QoIs, we employ the open-source software Dakota v6.6 [10], developed at Sandia National Laboratories. Specifically, we use a non-intrusive polynomial chaos expansion (PCE) approach [129], to approximate the mean pressure coefficient, as follows:

$$C_P^K(z_0, \alpha) = \sum_{k=0}^{K} a_k \Psi_k(z_0, \alpha) \tag{6.3}$$

where K is the number of terms in the polynomial expansion [110], a_k are constant coefficients and Ψ_k are basis functions of the uncertain parameters (z_0, α). Since the input parameters are uniformly distributed, the PCE is constructed using Legendre polynomials as basis. The coefficients a_k are calculated using a collocation strategy over an anisotropic tensor grid [110], with three points for z_0 and five points for α; this implies that 15 CFD simulations (for each wind direction angle, i.e. 0° and 20°) are performed. The coefficients of the PCE can be combined to obtain estimates for

the mean and variance of the QoIs, while probability distributions can be obtained by sampling the PCE response surface. In the present study, we compute probability distributions and 95% credible intervals from $10,000$ realizations of the PCE.

6.1.3 Turbulence model UQ

The turbulence model UQ approach used in this study was first proposed by [30], and further developed in [50, 37]. The methodology consists of first performing a baseline RANS simulation, and subsequently introducing perturbations in the Reynolds stresses. The perturbations are defined in terms of a decomposition of the Reynolds stress tensor, i.e. based on the tensor magnitude and the eigenvalues and eigenvectors of the normalized anisotropy tensor. The perturbed Reynolds stresses R^*_{ij} can then be written in terms of the perturbed turbulence kinetic energy k^*, eigenvectors v^*_{ik} and eigenvalues Λ^*_{kl}:

$$R^*_{ij} = 2k^* \left(\frac{1}{3}\delta_{ij} + v^*_{ik}\Lambda^*_{kl}v^*_{jl} \right). \tag{6.4}$$

In the present study, we first perturb the anisotropy tensor eigenvalues, to introduce a bias in the Reynolds stress prediction, making the turbulence more 1-, 2-, or 3-component. The perturbations are defined as a change in the barycentric map coordinates of the original model prediction for the Reynolds stress tensor. The barycentric map, shown in Figure 6.1, provides a representation for all realizable Reynolds stress tensors [5]. Its corners represent the different limiting states of turbulence

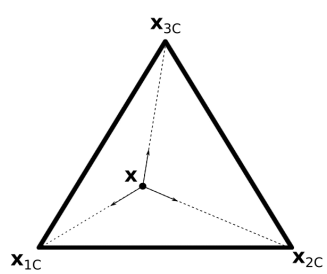

Figure 6.1: Barycentric map.

anisotropy, e.g. isotropic turbulence corresponds to the three-component ($\mathbf{x}_{3C}$) corner. The map coordinates for any Reynolds stress tensor are a linear combination of the corner coordinates; the coefficients are a function of the anisotropy tensor eigenvalues, $\lambda_1 \geq \lambda_2 \geq \lambda_3$:

$$\mathbf{x} = (\lambda_1 - \lambda_2)\mathbf{x}_{1C} + (2\lambda_2 - 2\lambda_3)\mathbf{x}_{2C} + (3\lambda_3 + 1)\mathbf{x}_{3C}. \tag{6.5}$$

Hence, the intended bias can be introduced by first determining the barycentric map coordinates of the Reynolds stress computed by the baseline turbulence model ($\mathbf{x}$ in Figure 6.1), and subsequently

injecting uncertainty by moving towards one of the corners of the map. Because the extreme limiting states are not likely to occur, the bias introduced in the turbulent state is limited using a factor ΔB_i:

$$\mathbf{x_i^*} = \mathbf{x} + \Delta B_i(\mathbf{x_{iC}} - \mathbf{x}), \tag{6.6}$$

where i is the corner index. We selected $\Delta B_1 = 0.5$, $\Delta B_2 = 0.5$, $\Delta B_3 = 0.25$ based on previous studies [37, 133]. The sensitivity of the results to these values is investigated in Section 6.2.2.

Once the perturbed eigenvalues are determined, a perturbed anisotropy tensor is calculated, retaining the eigenvectors predicted by the linear-eddy viscosity model. Next, this perturbed anisotropy tensor is used to calculate the turbulence kinetic energy production term in the transport equation for k, thereby indirectly perturbing the magnitude of the tensor. It has been shown that the eigenvalues corresponding to 1-component turbulence maximize the production of k, while 3-component turbulence reduces the production term to 0 [50, 37]. The eigenvalues corresponding to 2-component turbulence will result in values for turbulent production in between these two limits.

6.1.4 Second order probability

To propagate both the epistemic and aleatory uncertainties to the QoIs, we use a second-order probability framework [118], in which an outer loop specifies a set of epistemic variables and an inner loop samples the probability distribution of the aleatory variables. In our case, the outer loop will define the direction of perturbation of the eigenvalues of the Reynolds stress tensor, namely no perturbation or a perturbation to 1-, 2-, or 3-component turbulence. For each given perturbation, the inner loop will use the procedure described in section 6.1.2 to compute a probability distribution for the QoIs given the uncertainty in the inflow parameters. Since we selected 15 aleatory samples and the epistemic variable can assume 4 values, we performed 15×4 CFD simulations for each wind direction angle (i.e. 0° and 20°). The resulting ensemble of cumulative distribution functions (CDFs) will form a so called horsetail plot, from which we can compute a lower and upper bound on the prediction. These are defined as the minimum and maximum of the ensemble of 95% credible intervals.

6.2 Results

This section presents the comparison between computational predictions and measurements of the time-averaged pressure coefficients; for the remaining of the chapter, this will be referred to as simply the pressure coefficient. In the following subsections, we first consider the results of the inflow UQ study and the turbulence model UQ study separately. Subsequently, the results of the second-order probability framework are presented. In all cases, results are obtained for two wind directions (i.e. 0° and 20°).

6.2.1 Inflow UQ

0° wind direction

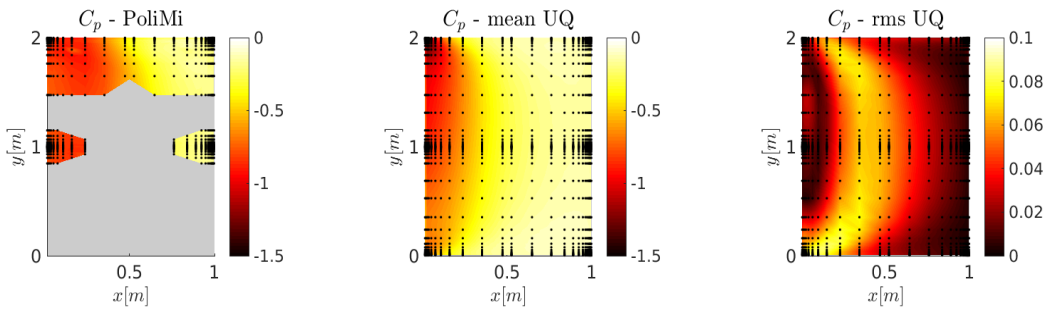

(a) PoliMi (b) Mean from UQ (c) Std from UQ

Figure 6.2: Mean pressure coefficient on building's lateral facade at 0°.

Figure 6.2 shows the distribution of the pressure coefficient on the building's lateral facade at 0° wind directions; the mean and standard deviation (std) outcome of the inflow UQ study are compared to the wind tunnel measurements. Similar qualitative features can be appreciated between the experiment and the numerical result: the flow separates at the windward edge of the building producing a region of relatively strong suction (red region of Figures 6.2a and 6.2b) and subsequently reattaches towards the rear part of the model (yellow region of Figures 6.2a and 6.2b). Nevertheless, from the plot it appears that the RANS UQ analysis predicts a stronger negative pressure peak at the edge of the building and a more rapid recovery, compared to the experiment. By looking at Figure 6.2c, we can conclude that the uncertainty in the inflow parameters is mainly significant in determining the reattachment point of the flow, where the standard deviation of the pressure coefficient is above 0.05.

To provide a more quantitative comparison, Figure 6.3 shows profiles of the pressure coefficient along two rows of taps on tiles A and B. Here, the mean and 95% credible interval resulting from the UQ analysis are compared to the measurements. The 95% credible intervals encompass only $\sim 13\%$ and $\sim 15\%$ of the experimental data on tiles A and B respectively. The highest deviation appears at reattachment, where the discrepancy between the measurements and the bounds of the predicted 95% credible intervals is 0.27 on tile A and 0.17 on tile B. In general, good agreement is obtained near the leeward edge of the model, where the flow is attached. The comparison deteriorates significantly inside the separation region and around the location of reattachment, suggesting that the uncertainty in the turbulence model might be dominant in this region. By looking at the width of the 95% credible interval plotted in Figure 6.3, we can again conclude that the uncertainty in the inflow condition is more relevant in the mid-portion of the model.

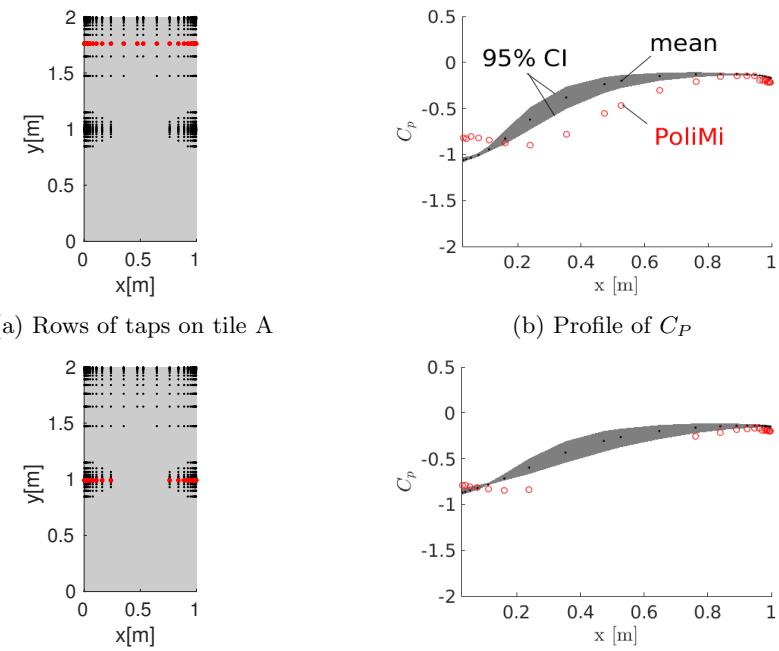

(a) Rows of taps on tile A

(b) Profile of C_P

(c) Rows of taps on tile B

(d) Profile of C_P

Figure 6.3: Profiles of mean and 95% credible interval (black dots and gray region respectively) of pressure coefficient compared to the measurements (red circles) at 0°.

20° wind direction

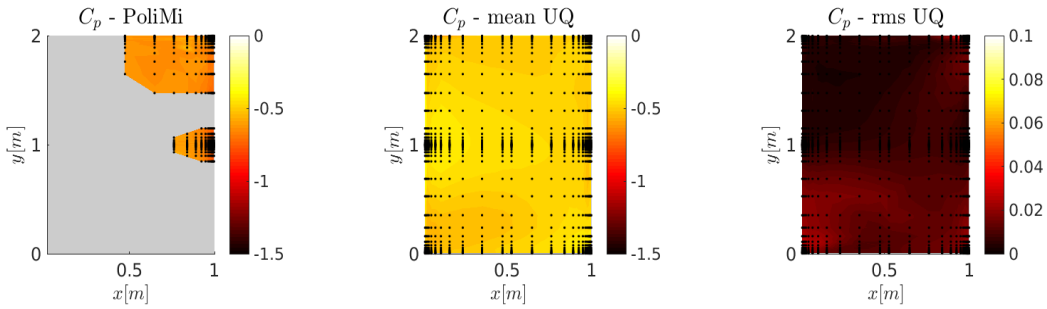

(a) PoliMi (b) Mean value from UQ. (c) Standard deviation from UQ.

Figure 6.4: Mean pressure coefficient on building's lateral facade at 20°.

Figure 6.4 shows the distribution of the pressure coefficient on the building's lateral facade, for the 20° wind direction. For this wind direction the flow on the lateral facade is fully separated and the measurements are concentrated in the downstream half of the facade only. The mean value resulting from the UQ study is compared to the wind tunnel experiment, showing good qualitative agreement: the flow is also fully separated and the pressure distribution is nearly uniform. However, the RANS UQ underestimates the strength of the negative pressure. The standard deviation of the pressure coefficient, shown in Figure 6.4c, is negligible everywhere, meaning that the inflow uncertainty has no influence on the QoIs in this case.

Figure 6.5 shows the pressure coefficient profiles along two rows of taps on tiles A and B; the mean and 95% credible intervals computed from the UQ study are compared to the measurements. The trend is similar in both tiles A and B, but there seems to be an offset in the prediction. The maximum discrepancy between numerical prediction and experiment is 0.20 and 0.31 on tiles A and B respectively.

6.2.2 Turbulence model UQ

This section investigates the performance of the turbulence model UQ method by presenting results from the simulations with the different perturbations. The results were obtained with $\Delta B_1 = 0.5$, $\Delta B_2 = 0.5$, $\Delta B_3 = 0.25$. In section 6.2.2, the influence of the choice for the perturbation sizes is investigated for the 20° wind direction.

0° wind direction

Figure 6.6 shows a top view of the flow field around the building at half the building height, obtained for the simulations with mean inflow parameters at 0° wind direction; the result of the baseline simulation is compared to the corresponding perturbations. The perturbation towards maximum

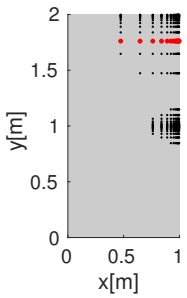

(a) Rows of taps on tile A

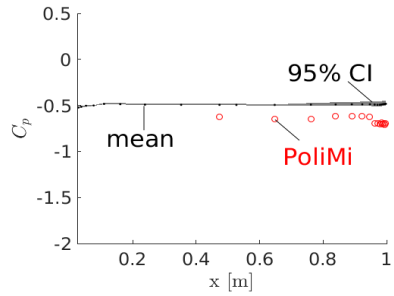

(b) Profile of mean C_P

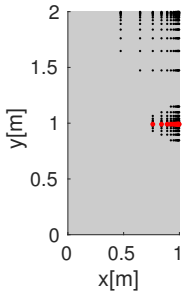

(c) Rows of taps on tile B

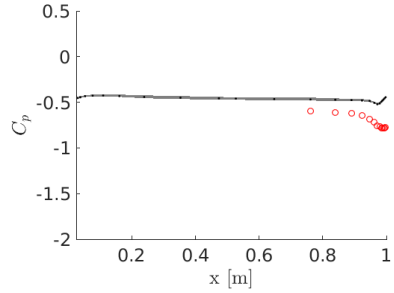

(d) Profile of mean C_P

Figure 6.5: Profiles of mean and 95% credible interval (black dots and gray region respectively) of pressure coefficient compared to the measurements (red circles) at 20°.

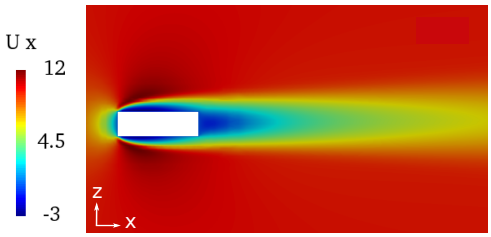

(a) Baseline

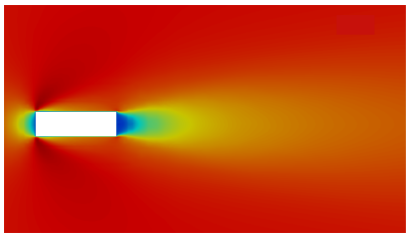

(b) 1-component perturbation

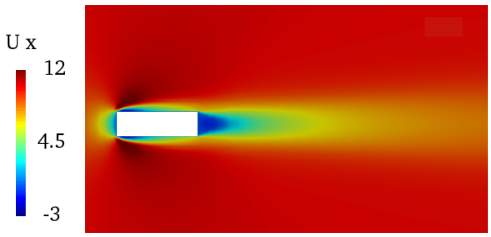

(c) 2-component perturbation

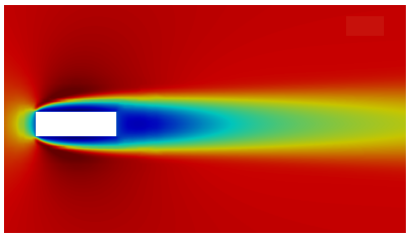

(d) 3-component perturbation

Figure 6.6: Mean velocity contours at half the building height. Baseline simulation with mean inflow parameters and simulations with 1-, 2-, and 3-component perturbations, at 0° wind direction.

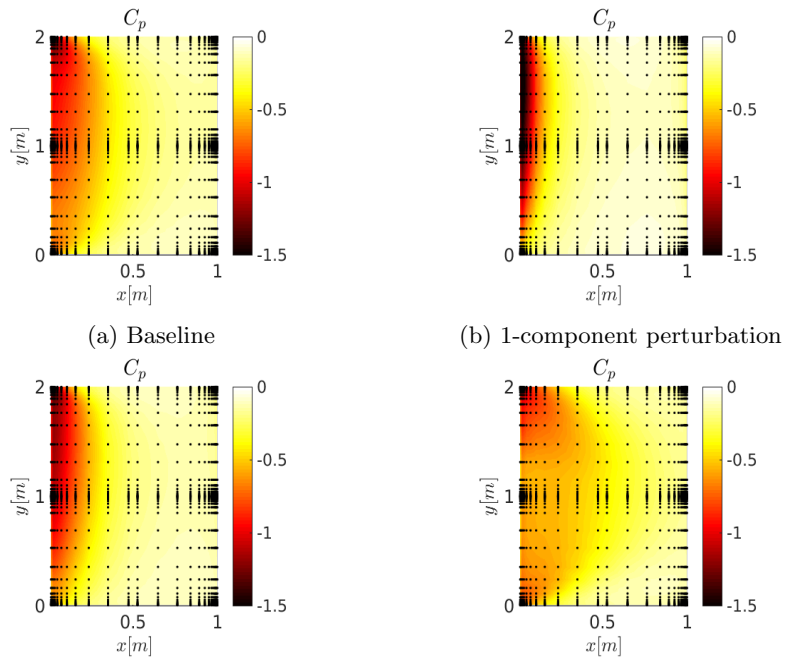

(a) Baseline

(b) 1-component perturbation

(c) 2-component perturbation

(d) 3-component perturbation

Figure 6.7: Pressure coefficient contours on the lateral facade. Baseline simulation with mean inflow parameters and simulations with 1-, 2-, and 3-component perturbations, at 0° wind direction.

production of turbulence kinetic energy (at $\mathbf{x}_{1C}$) tends to minimize the size of the separation region and the building wake, while the perturbation towards zero production (at $\mathbf{x}_{3C}$) as the opposite effect. The result of the 2-component perturbation and the baseline falls between the 1- and 3-component perturbations (Figure 6.6).

As a result, the 1-component perturbation minimizes the size of the suction area on the building's lateral facade, but produces a stronger negative pressure peak at the windward edge (Figure 6.7b). Conversely, the 3-component perturbation maximizes the size of the suction area, but produces a more gentle recovery (Figure 6.7d). As expected, the baseline and 2-component perturbations are somewhere in between (Figures 6.7a and 6.7c). In the rear portion of the model, the flow is attached and the behavior of the 3 perturbations and baseline simulation is similar, indicating that the uncertainty in the turbulence model is less significant.

20° wind direction

Figure 6.8 compares the velocity fields obtained from the baseline simulation and the simulations with the different perturbations for the 20° wind direction. The results show a similar behavior as in the 0° case. The 1- and 3-component perturbations respectively minimize and maximize the size of the separation region around the building, encompassing the baseline and 2-component results. As a consequence, extreme but localized suction is produced by the 1-component perturbation at the windward edge, while weaker but more diffused negative pressure is generated by the 3-component perturbation (Figure 6.9).

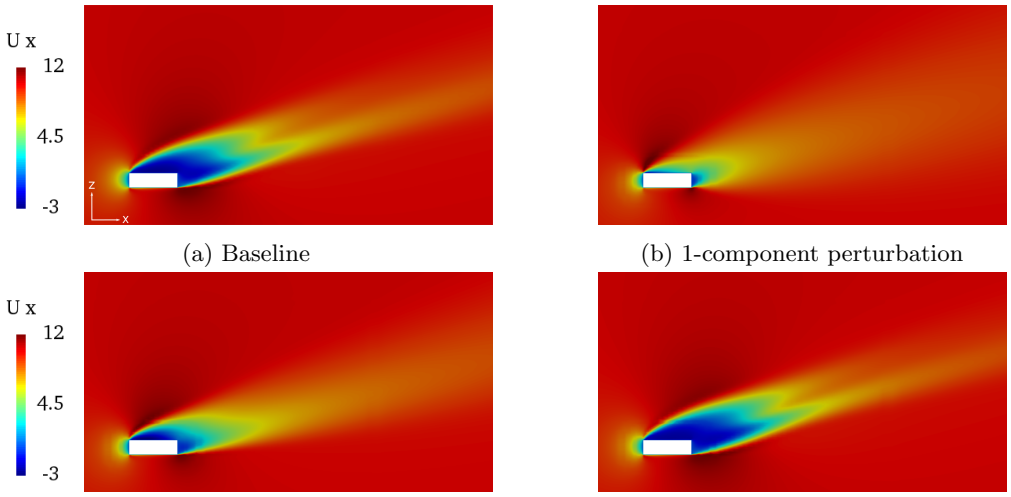

(a) Baseline (b) 1-component perturbation

(c) 2-component perturbation (d) 3-component perturbation

Figure 6.8: Mean velocity contours at half the building height. Baseline simulation with mean inflow parameters and simulations with 1-, 2-, and 3-component perturbations, at 20° wind direction.

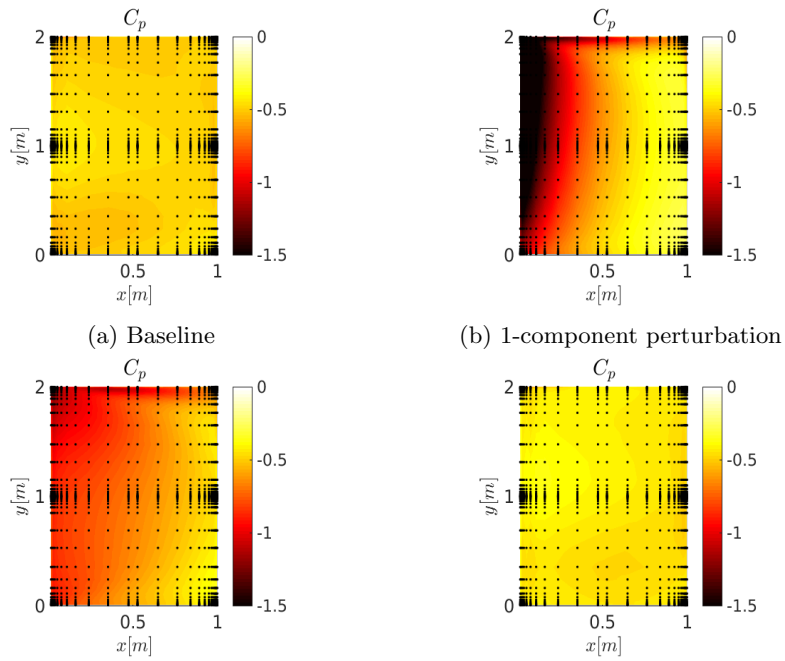

(a) Baseline

(b) 1-component perturbation

(c) 2-component perturbation

(d) 3-component perturbation

Figure 6.9: Pressure coefficient contours on the lateral facade. Baseline simulation with mean inflow parameters and simulations with 1-, 2-, and 3-component perturbations, at 20° wind direction.

Sensitivity on the perturbation size

The sensitivity of the pressure coefficient to the perturbation size Δ_B is investigated for the 20° wind direction; this wind direction showed the strongest influence of the perturbation size and direction. Figure 6.10 shows the pressure coefficient along a row of taps on tile A, as computed by the three perturbations with three different values of Δ_B. The behavior seems monotonic for both 1- and 2-component perturbations, meaning that by arbitrarily increasing or decreasing Δ_B, we can be more or less conservative in the prediction. The influence of the perturbation size seems negligible for the 3-component perturbation; however, in this case Δ_B could not be increased above 0.25 without encountering convergence issues.

As evident from Figure 6.10, the effect of the perturbation size is more significant at the windward edge than in the rear portion of the model; hence, possible areas of future research could be the extension of the approach to non-uniform perturbation sizes and directions.

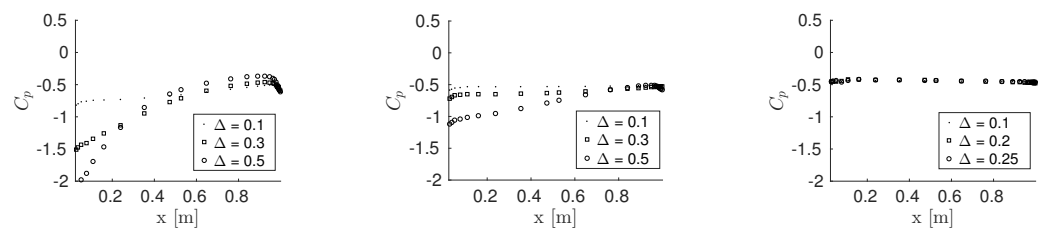

(a) 1-component perturbation (b) 2-component perturbation (c) 3-component perturbation

Figure 6.10: Sensitivity of the pressure coefficient to the size of the perturbation, at 20° wind direction.

6.2.3 Second order probability

Following the method highlighted in Section 6.1.2, the combined effect of inflow and turbulence model uncertainties is quantified. In the following, we present the resulting ensemble of CDFs at a select number of pressure taps, and the overall credible interval along a row of taps on each tile for both wind directions.

0° wind direction

Figure 6.11 shows the CDFs of C_P for the baseline simulations and the three perturbations. The results are presented for one tap per pressure tile (red dots in Figures 6.11a and 6.11d), and compared to the wind tunnel data. The taps were selected to be representative of the behavior of all taps in different flow regions, such as separation (tap 1 in Figure 6.11d), reattachment (tap 1 in Figure 6.11a), and fully-reattached flow (tap 2 in Figures 6.11a and 6.11d). Focusing on the selected pressure taps, the 1- and 3-component perturbations generally predict upper and lower bounds for

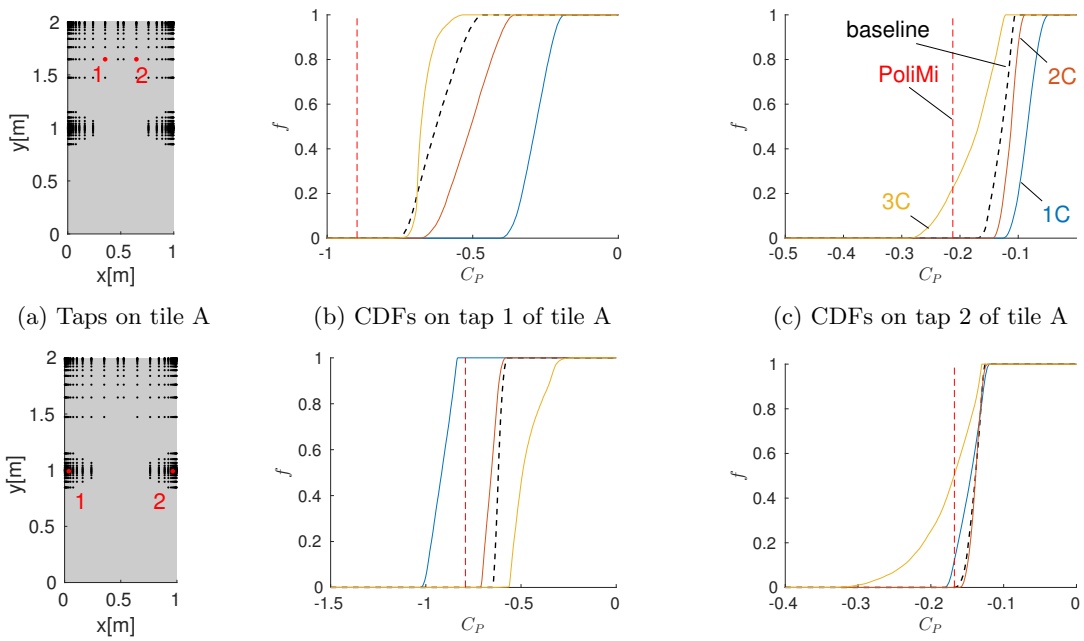

(a) Taps on tile A (b) CDFs on tap 1 of tile A (c) CDFs on tap 2 of tile A

(d) Taps on tile B (e) CDFs on tap 1 of tile B (f) CDFs on tap 2 of tile B

Figure 6.11: Cumulative density functions of pressure coefficients on four taps at 0°; the result from the inflow UQ (black) is compared to the 1-component perturbation (blue), the 2-component perturbation (orange), the 3-component perturbation (yellow) and the wind tunnel data (red).

the baseline result. The only exceptions happen on the bottom portion of the CDF on tap 1 of tile A (Figure 6.11b) and tap 2 of tile B (Figure 6.11f). The experimental values of C_P measured by the selected pressure taps are within the range predicted by the horsetail plots in most regions, except near tap 1 of tile A (Figure 6.11b). In this case, the tap is located in the reattachment region and the strength of the negative pressure coefficient is underpredicted by 0.14. The spread of the CDFs on tap 1 is very pronounced for both tiles A and B, indicating that the uncertainty in the turbulence model is significant inside the separation region. The opposite happens on tap 2 of tile B (Figure 6.11f), where the flow is attached; here, the results from the simulations with perturbations seem to approach the baseline prediction.

From each CDF, we can compute mean and 95% credible intervals for the pressure coefficient predictions. Figure 6.12 compares the corresponding profiles along two rows of taps on tiles A and B, to the wind tunnel data. The 1-component perturbation causes a stronger negative peak of pressure coefficient at the windward edge and a faster recovery (blue area in Figure 6.12), compared to the baseline result. In contrast, the 3-component perturbation is characterized by slower recovery than the baseline (yellow area in Figure 6.12). The result of the 2-component perturbation is largely between the results of the 1- and 3-component perturbations, except around the location of flow reattachment (green area in Figure 6.12). This is also the region of highest discrepancy with the measurements. The large difference between the results obtained with the different perturbations close to the windward edge indicates that the uncertainty related to the turbulence model is dominant when separation occurs; further downstream, where the flow is attached, all the perturbed results converge towards the baseline result.

Figure 6.13 combines the 95% credible intervals corresponding to each of the perturbations to provide a single bound on the prediction of C_P along two rows of taps on tiles A and B. The prediction intervals encompass the wind tunnel data along the most upstream 20% and most downstream 40% of the facade. The main limitations of the approach appears to be in the separation and reattachment regions. At the windward edge, the prediction for the lower bound on the negative pressure peak is overly conservative. This could likely be attenuated by reducing the size of the perturbation in the direction of maximum production, which causes the strong suction. Moving downstream, the 1- and 2-component perturbations exhibit a too fast pressure recovery compared to the experimental data. The more constant value obtained with the 3-component perturbation provides a better qualitative representation of the experimental observations, but the absolute value is too low to correctly capture the uncertainty in the prediction. As a result, the maximum discrepancy between the measurements and the predicted credible bounds occurs in the separated flow region near the reattachment location; on the rows of taps considered here, this discrepancy is 0.22 and 0.17 on tiles A and B respectively.

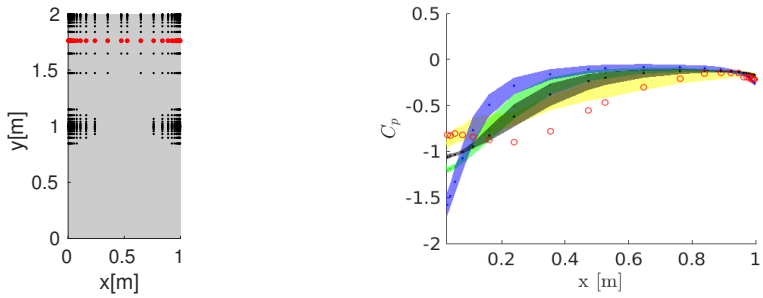

(a) Rows of taps on tile A

(b) Profile of mean C_P

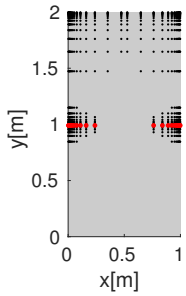

(c) Rows of taps on tile B

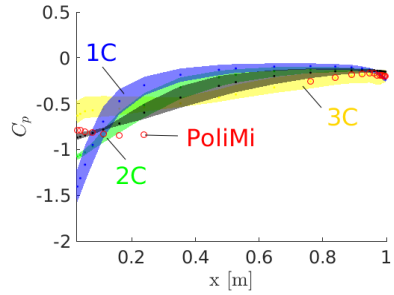

(d) Profile of mean C_P

Figure 6.12: Profiles of pressure coefficient at 0° wind direction. Mean and 95% credible interval computed from the inflow UQ (gray), the 1-component perturbation (blue), the 2-component perturbation (green) and the 3-component perturbation (yellow), compared to the measurements (red circles).

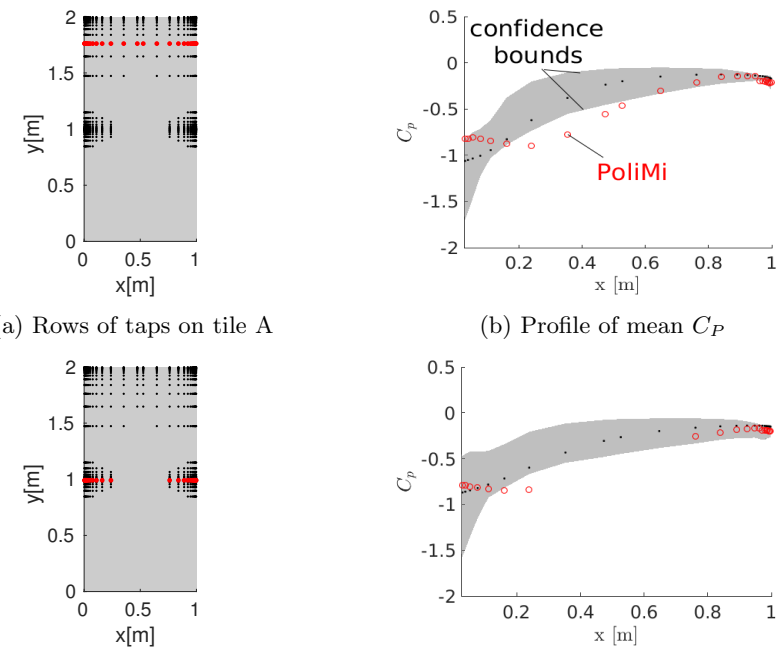

(a) Rows of taps on tile A

(b) Profile of mean C_P

(c) Rows of taps on tile B

(d) Profile of mean C_P

Figure 6.13: Profiles of pressure coefficient at 0°. Mean and credible interval computed from the combination of inflow and turbulence model UQ (gray), compared to the measurements (red circles).

20° wind directions

Figure 6.14 shows the ensemble of the cumulative density functions of C_P at two different pressure taps at 20° wind direction. Considering the selected tap on tile A, the 1− and 2−component perturbations provide bounds on the baseline prediction. In addition, the measurement value is encompassed by the tail of the CDF corresponding to the 2−component perturbation. Considering tile B, the CDF for the simulations with the three-component perturbations differs only slightly from the baseline result, but generally the baseline result is only bounded by the perturbed simulation results in the lower portion of the CDF. In this case, the experimental value does not fall within the 95% credible bounds of the ensemble of CDFs.

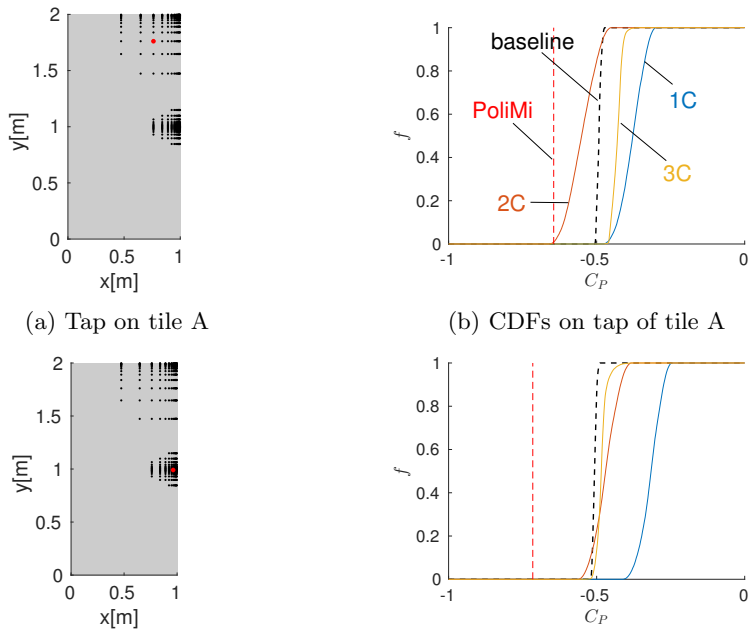

(a) Tap on tile A

(b) CDFs on tap of tile A

(c) Tap on tile B

(d) CDFs on tap of tile B

Figure 6.14: Probability distributions of pressure coefficients computed on top-corner tap at 20°; the result from the inflow UQ (black) is compared to the 1-component perturbation (blue), 2-component perturbation (orange), 3-component perturbation (yellow) and wind tunnel data (red).

Figure 6.15 shows the profiles of mean and 95% credible intervals obtained from the CDFs for the pressure coefficient predictions at 20° wind direction along two rows of taps on tiles A and B. For this wind direction, the 1- and 3-component perturbations provide lower and upper bounds for the baseline prediction at the windward edge, while in the rear portion of the model the bounds are obtained from the 1- and 2-component perturbations. At the windward edge, the 1-component perturbation produces a negative pressure peak that is even stronger than in the 0° case. As a consequence, the predicted combined uncertainty in the C_P values, shown in Figure 6.16, is very

large in this region. As mentioned before, this issue could be attenuated by reducing the size of the 1-component perturbation in the stagnation region. In the rear portion of the model, the method predicts a more reasonable trend, although the experimental value is not withing the predicted bounds in the most downstream locations. The maximum discrepancy between the measurements and the credible bounds in this region is 0.13 and 0.31 on tiles A and B respectively.

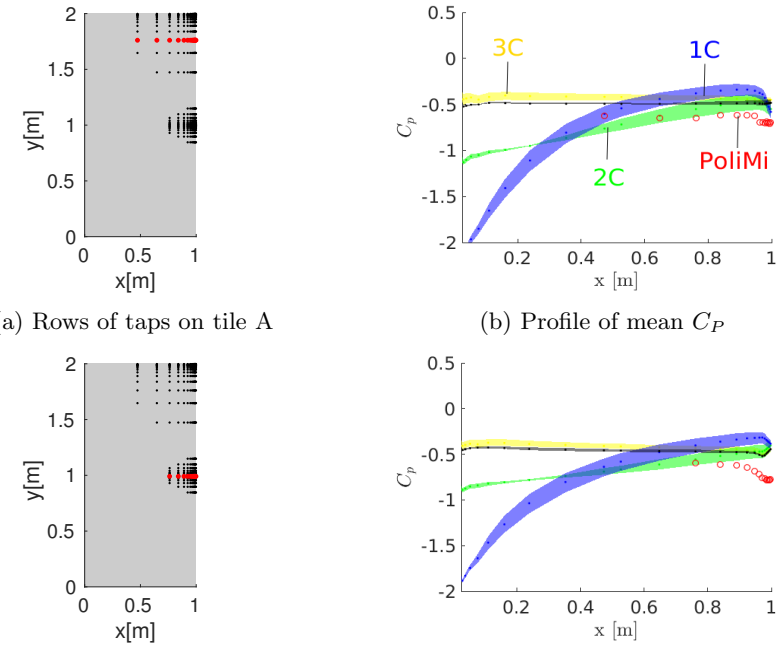

(a) Rows of taps on tile A

(b) Profile of mean C_P

(c) Rows of taps on tile B

(d) Profile of mean C_P

Figure 6.15: Profiles of pressure coefficient at 20°. Mean and 95% credible intervals computed from the inflow UQ (gray), the 1-component perturbation (blue), the 2-component perturbation (green) and the 3-component perturbation (yellow), compared to the measurements (red circles).

6.3 Summary

The chapter has presented a method to quantify the combined effect of inflow and turbulence model uncertainties in RANS predictions of the mean pressure distribution on high-rise buildings.

First, we quantified the uncertainty related to the inflow boundary conditions using two uncertain parameters: the roughness length and the model orientation. Probability distributions for these parameters were defined using wind tunnel data and propagated to the QoIs using a PCE approach. The resulting credible intervals were narrow and did not account for the difference between the simulations and the experiments. The reattachment region was the only portion of the model that was significantly impacted by the uncertainty in the inflow parameters.

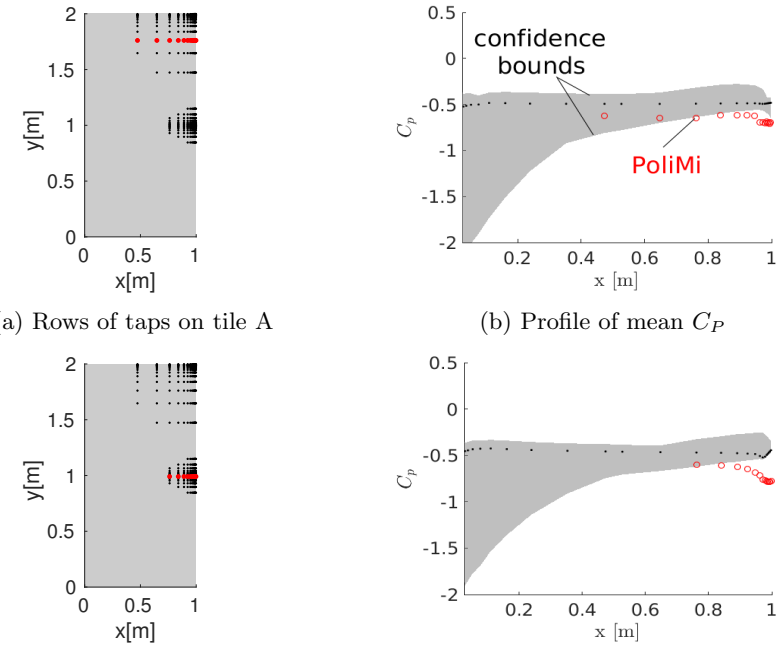

(a) Rows of taps on tile A

(b) Profile of mean C_P

(c) Rows of taps on tile B

(d) Profile of mean C_P

Figure 6.16: Profiles of pressure coefficient at 20°. Mean and credible interval computed from the combination of inflow and turbulence model UQ (gray), compared to the measurements (red circles).

To quantify the turbulence model uncertainty, we introduced perturbations into the eigenvalues of the Reynolds stress tensor of the baseline simulations [35, 30]. The resulting interval for the C_P values was largest in the upstream portion of the model, i.e. in the separated flow region. Towards the leeward edge of the building the results of the three perturbations converged to the baseline result. The effect of different perturbation sizes revealed a monotonic behavior of the solution, meaning that that the perturbation size can be increased or decreased to provide a more or less conservative prediction.

Finally, the two methods were combined in a second-order probability framework [118], to provide a single interval for the prediction of C_P. The prediction intervals encompassed the wind tunnel data along the most upstream $\sim 20\%$ and most downstream $\sim 40\%$ of the facade at 0° wind direction. On the $\sim 40\%$ of the facade that surrounds the reattachment location, the experimental pressure coefficient was up to ~ 0.22 lower than the lowest bound predicted by the method. At 20° wind direction, the measurements were concentrated on the downstream half of the building only, and the flow on the lateral facade was fully separated. On the downstream $\sim 20\%$ of the facade, the measured pressure coefficients were up to ~ 0.31 lower than the lowest bound predicted by the method.

The results indicate that the uncertainty due to the turbulence model is dominant. This conclusion is likely to be specific to cases that consider validation with wind tunnel experiments; when comparing results to field measurements, in which the atmospheric boundary layer flow would exhibit larger variability, the inflow uncertainty could be more important. The current approach towards predicting turbulence model form uncertainty was shown to have some limitations in terms of predicting the uncertainty in the pressure coefficient in the regions of flow separation. This could be related to the spatial uniformity of the directions and magnitudes of the Reynolds stress eigenvalue perturbations.

Chapter 7

Multi-fidelity framework

The UQ study of Chapter 6 confirmed the limitations of RANS turbulence models in dealing with flow separation and reattachment, resulting in low accuracy and significant uncertainty in the mean pressure prediction in these regions. On the other side, the uncertainty in the inflow conditions, i.e. roughness length and model orientation, had a small effect on the prediction. Nonetheless, for a comprehensive wind loading design, the complete wind rose has to be considered [51], with the potential to overturn the relative importance between turbulence model and inflow contributions. For example, preliminary results at two wind directions, i.e. 0° and 20°, demonstrated great difference in the mean pressure distribution between the two cases (see Figures 6.2b and 6.4b).

To improve the accuracy of RANS simulations, while considering the entire wind rose, a multi-fidelity approach is explored in this chapter. The method aims to take advantage of the low computational cost of RANS and the accuracy and great details of LES. For simplicity, the wind direction is the sole uncertain parameter of the method. The framework employs non-intrusive PCE [129] to approximate the stochastic models of both the low-fidelity model and discrepancy function between low- and high-fidelity models [84]. The two stochastic models are finally combined to produce an updated prediction of the mean pressure distribution around the building.

The mean pressure is not the main QoI for wind loading design; therefore, we also extend the framework to enable the computation of the rms pressure coefficient. To achieve this goal, an empirical model [89] is used in combination with RANS, as low-fidelity model; the rest of the framework is the same as before. Once predictions of mean and rms pressure coefficients are available, one could estimate the peak pressure coefficient at any wind direction, using the peak factor method [27].

In the remaining of the chapter, first the multi-fidelity method is presented. Subsequently, results in terms of mean and rms pressure coefficients at different wind directions, are compared to the LES database.

7.1 CFD models

7.1.1 RANS

To perform RANS simulations at different wind directions, we simply modify the velocity components imposed at the inflow, while maintaining the same computational grid and setup presented in Section 6.1.1; importantly, the grid includes $\sim 42,000$ cells on the building's surface.

The solution of the RANS equations provides a prediction of the mean pressure distribution around the building and an additional model is needed to retrieve the pressure fluctuations. Empirical models have been formulated in the past for this task; they relate the rms pressure coefficient C'_p to the local mean pressure coefficient C_P and turbulence kinetic energy k [88, 105, 89, 97, 56]. Within the empirical models, the one developed by Paterson and Holmes [89] achieves the highest accuracy in our test case; therefore, it's selected as part of the multi-fidelity framework:

$$C'_p = \frac{k/3 + 0.816|C_P|U_0\sqrt{k_0}}{0.5U_H^2} \tag{7.1}$$

where k_0 and U_0 are the turbulence kinetic energy and mean velocity magnitude of the incoming ABL, while U_H is the reference wind velocity at roof height.

7.1.2 LES

Since the LES turbulent inflow generator requires the inlet to be perpendicular to the incoming ABL flow turbulence, each wind direction requires its own rotated mesh. For each of these meshes, the computational domain is 35m in the streamwise direction and 20m in the spanwise one; the height of the domain is 4m. The high-rise building is located at a distance of 5m to the inlet boundary and 30m to the outlet [24]. The blockage ratio, i.e. the ratio between the area of the windward face of the building and the domain cross section, is always below 2.8% [31]. The meshes include refinement regions close to the building model, resulting in a total number of $\sim 120,000$ cells on the building's surface. Subrid-scale turbulence is modeled using the dynamic k-equation model, while the rest of the setup is maintained as in Section 5.1.1.

7.2 Multi-fidelity method

When performing UQ, usually many model evaluations are necessary to precisely estimate the statistics of the QoIs, with respect to the uncertain input parameters. When a hierarchy of models, characterized by increasing computational cost and fidelity, is available, one can leverage the low-fidelity model to possibly reduce the number of high-fidelity model evaluations. Specifically, in a multi-fidelity framework, the low-fidelity model is evaluated at a fine grid of realizations of the input parameters, while the high-fidelity model is evaluated only at a small subset of points. Then, the

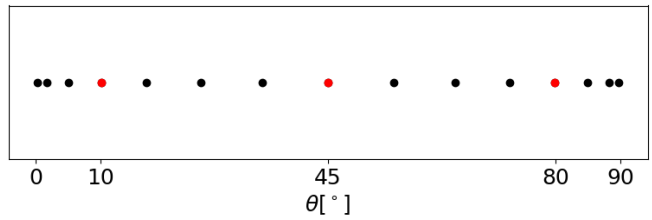

Figure 7.1: Quadrature points of polynomial expansions.

results of the low-fidelity model are corrected to match the ones of the high-fidelity model at the high-fidelity grid points [84].

In the present case, the wind direction θ is the only uncertain parameter. Given the symmetry of the building model, the range of wind directions between 0° and 90° is representative of the entire wind rose. Therefore, we assume that θ is uniformly distributed within these bounds and generate an anisotropic tensor grid, with 15 points (Figure 7.1). These points identify the wind directions at which the RANS simulations should be performed, in order to construct the low-fidelity surrogate model. LES simulations are performed only at a subset of wind directions, namely 3 (red dots of Figure 7.1), and used to build the surrogate model for the discrepancy function.

As in Section 6.1.2, PCE is used to approximate the mean pressure coefficient outcome of RANS, i.e. the low-fidelity model of the multi-fidelity framework, but now as a function of the wind direction:

$$C^{R}_{P,RANS}(\theta) = \sum_{k=0}^{R} a_{k,RANS}\Psi_k(\theta) \tag{7.2}$$

where $a_{k,RANS}$ are the coefficients of the polynomial expansion relative to the low-fidelity model and Ψ_k the basis functions; R is the number of terms of the high-order expansion. Since the wind direction is characterized by uniform probability distribution, the Legendre polynomials are used as basis; in particular, the high-order expansion includes polynomials up to 11th order. The coefficients of the expansion are computed using a collocation strategy on the fine tensor grid [110].

Similarly, the surrogate model for the discrepancy function $\Delta(\theta) = C_{P,LES}(\theta) - C_{P,RANS}(\theta)$, is constructed as follows:

$$\Delta^{L}(\theta) = C^{L}_{P,LES}(\theta) - C^{L}_{P,RANS}(\theta) = \sum_{k=0}^{L} a_{k,\Delta}\Psi_k(\theta) \tag{7.3}$$

where $a_{k,\Delta}$ are the corresponding coefficients, now computed using a collocation strategy on the coarse grid, while L is the number of terms of the low-order expansion ($L < R$); the low-order expansion includes polynomials up to 2nd order. Finally, the stochastic expansion of the high-fidelity model based on the fine grid, is approximated as:

$$C^R_{P,LES}(\theta) = \sum_{k=0}^{R} a_{k,LES}\Psi_k(\theta) \approx \sum_{k=0}^{L} \left(a_{k,RANS} + a_{k,\Delta}\right)\Psi_k(\theta) + \sum_{k=L+1}^{R} a_{k,RANS}\Psi_k(\theta) \tag{7.4}$$

where $a_{k,LES}$ are the coefficient of the polynomial expansion relative to the high-fidelity model [84]. The coefficients of the final PCE expansion are combined to obtain estimates for the mean and variance of the mean pressure coefficient, while 95% credible intervals are computed from $10,000$ realizations of the expansion.

The procedure to approximate the high-fidelity rms pressure coefficient $C'^R_{p,LES}$ on the fine grid, is completely analogous; the only difference is that now the role of low-fidelity model is played by the Paterson-Holmes model evaluated on the RANS flow field.

7.3 Results

This section presents the results of the multi-fidelity (MF) framework in terms of mean and rms pressure coefficients. In particular, the ability of the model to extrapolate to wind directions not included in the quadrature points is investigated.

7.3.1 Mean pressure coefficient

Table 7.1 summarizes the performance of the multi-fidelity method across the wind directions; the procedure is compared to a 2nd order PCE, built from the LES results on the 3-point grid, and a 11th order PCE, built from the RANS results on the 15-point grid. The table reports the root mean square error (RMSE) at the 3 quadrature points that the methods have in common (i.e. 10°, 45° and 80°) and at some wind directions, which are not quadrature points. Furthermore, the RMSE achieved by simply running a RANS simulation per wind direction is also reported in the table. The advantage of the multi-fidelity procedure is evident, having an average RMSE that is $\sim 69\%$ smaller than the RMSE achieved by the LES-based PCE. The 2nd order PCE, built from the LES results at 10°, 45° and 80°, achieves the lowest RMSE only at these wind directions, meaning that the model is likely overfitted to the quadrature points. The simple RANS simulation achieves the lowest RMSE at 0°, while the RANS-based 11th order PCE at 90°, i.e. the wind directions characterized by symmetric flow field; nonetheless, the RMSE of the MF framework is only slightly higher at these wind directions.

The rest of the section further investigates the ability of the multi-fidelity method to extrapolate to different wind directions. The C_P predicted by the method is compared to the results of LES and RANS simulations at different wind directions.

	RANS	LES: 2nd order PCE	RANS: 11th order PCE	MF
0°	**0.100**	0.237	0.103	0.117
10°	0.134	**0.003**	0.125	0.007
20°	0.125	0.087	0.123	**0.071**
40°	0.108	0.061	0.097	**0.056**
45°	0.092	**0.000**	0.108	0.012
60°	0.096	0.211	0.109	**0.073**
80°	0.131	**0.003**	0.133	0.010
90°	0.116	0.227	**0.087**	0.143
tot.	0.113	0.103	0.124	**0.061**

Table 7.1: Root mean square error (RMSE) of C_P prediction.

0° wind direction

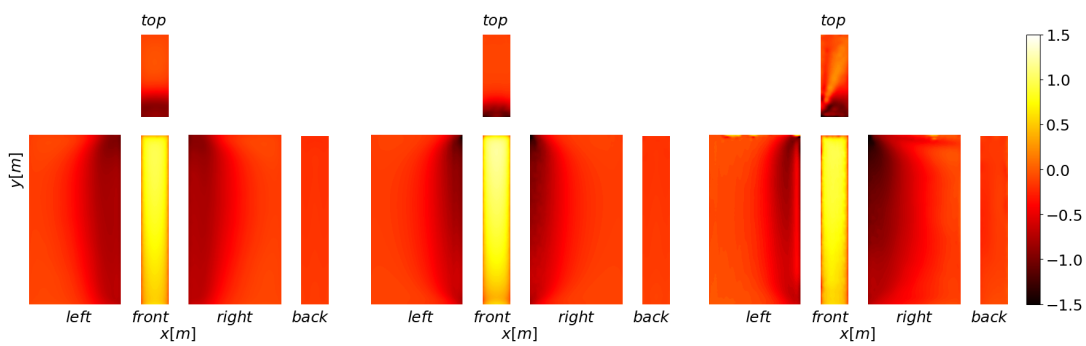

(a) LES (b) RANS (c) Multi-fidelity

Figure 7.2: Contours of mean pressure coefficient at 0°.

Figure 7.2 shows the contours of C_P around the unfolded building: the results of the LES (Figure 7.2a) and RANS (Figure 7.2b) simulations at 0° wind direction, are compared to the MF surrogate model evaluated at $\theta = 0°$ (Figure 7.2c). At this wind direction, the simple RANS simulation better captures the trend of C_P around the building, with respect to the MF framework. Nonetheless, the RANS under-predicts the size of the separation region and over-predicts the strength of the suction at the windward edge of the building, when compared to the LES result. The C_P field predicted by the MF framework is not symmetric, as a consequence of the wind directions chosen as quadrature points. The main discrepancies occur on the roof and side walls, where separation and reattachment occur.

Figure 7.3 plots profiles of C_P along different perimeters of the building. The C_P predicted by the RANS simulation better reproduces the LES behavior everywhere around the building, besides the *front* face, where the MF framework achieves higher accuracy. As a result, the RMSE of the RANS is 0.0100, which is 15% lower than the one achieved by the multi-fidelity model. Limited to

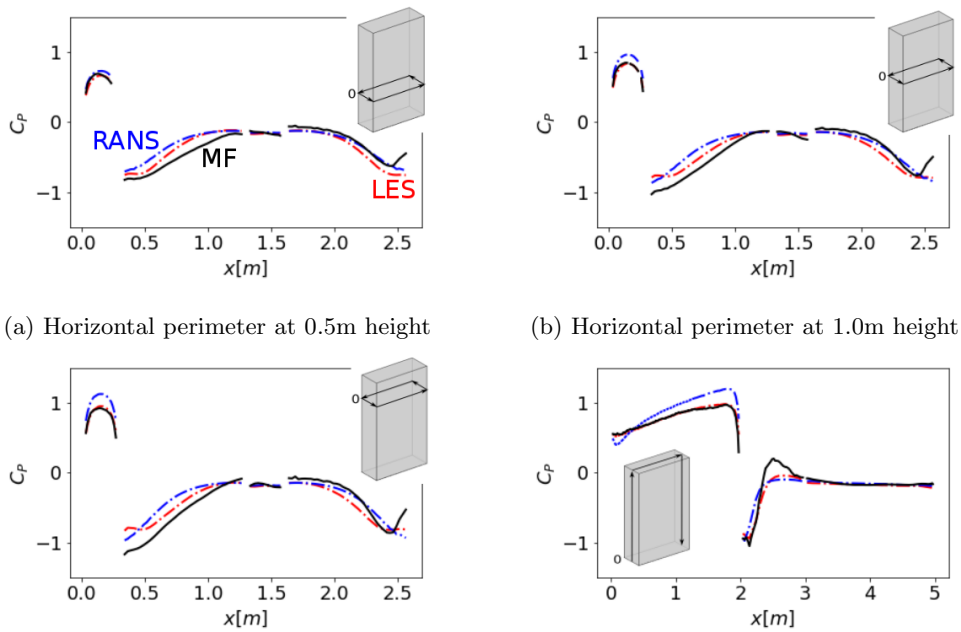

(a) Horizontal perimeter at 0.5m height

(b) Horizontal perimeter at 1.0m height

(c) Horizontal perimeter at 1.5m height

(d) Vertical perimeter

Figure 7.3: Profiles of mean pressure coefficient at 0°.

Figure 7.3, the maximum absolute error between RANS and LES is ~ 0.22 and occurs on the *front* face, while the maximum discrepancy between MF and LES is ~ 0.77, which occurs at the windward edge of the *top* face.

20° wind direction

Figure 7.4 shows the contours of C_P on the building's surface at 20° wind direction. In this case, the multi-fidelity procedure represents an improvement over the RANS simulation, especially on the *front* and *right* faces. The better performance of the MF model is also reflected in the RMSE, which is 70% lower than the one achieved by the RANS simulation.

Figure 7.5 shows profiles of C_P along different perimeters of the building. The good agreement between MF and LES is confirmed everywhere around the building. Furthermore, in those regions where the agreement gets worse, the MF model seems to converge to the RANS result, meaning that at 20°, the multi-fidelity procedure is always at least as good as the RANS, and often better. As a consequence, a maximum absolute error of ~ 0.25 is experienced by both models, along the selected perimeters.

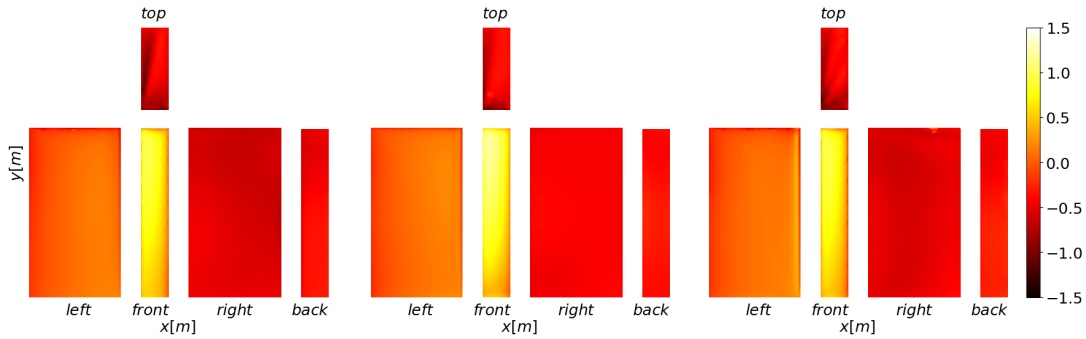

(a) LES (b) RANS (c) Multi-fidelity

Figure 7.4: Contours of mean pressure coefficient at 20°.

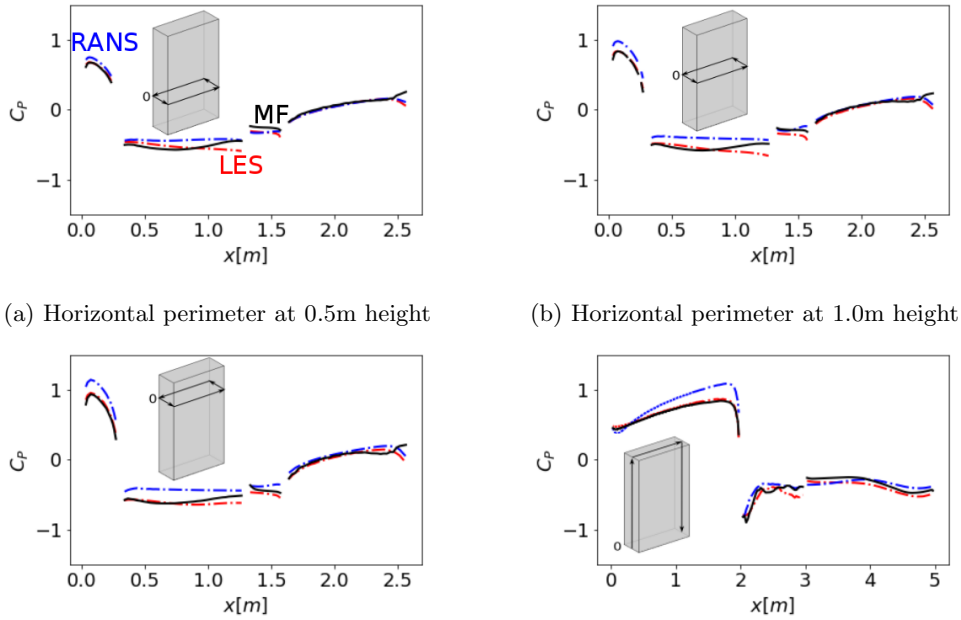

(a) Horizontal perimeter at 0.5m height

(b) Horizontal perimeter at 1.0m height

(c) Horizontal perimeter at 1.5m height

(d) Vertical perimeter

Figure 7.5: Profiles of mean pressure coefficient at 20°.

40° wind direction

Similar results are obtained at 40°, as shown in Figure 7.6. Once again, the multi-fidelity framework represents an improvement over the RANS simulation, especially on the *front*, *right* and *top* faces, resulting in a RMSE, that is almost half the one achieved by the RANS simulation.

This is more evident from Figure 7.7: the MF model is not only capable of correcting the bias that affects the RANS in some locations, such as the *right* face, but also to improve the C_P prediction in those locations where the correct trend is not captured by the RANS, such as the *back* face (Figure 7.7d). Along the selected perimeters, the maximum absolute error experienced by the RANS is ~ 0.58 and occurs at the windward edge of the roof (Figure 7.7d); here the RANS, unlike the LES and MF models, predicts extreme suction. The maximum discrepancy between MF and LES results is ~ 0.23 and occurs on the *top* face, where the MF procedure predicts a conical vortex that is slightly larger than the LES one.

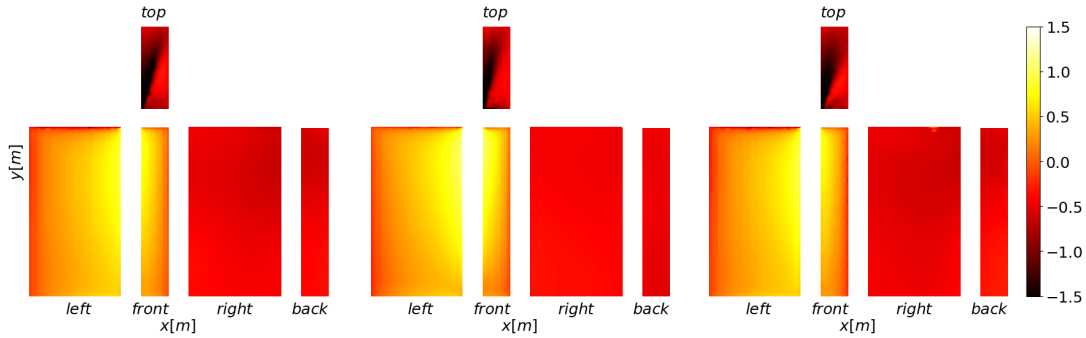

(a) LES (b) RANS (c) Multi-fidelity

Figure 7.6: Contours of mean pressure coefficient at 40°.

60° wind direction

Figure 7.8c shows the result of the multi-fidelity surrogate model evaluated at $\theta = 60°$, while Figures 7.8a and 7.8b, show the contours of C_P outcome of the LES and RANS simulations at 60°, respectively. At this wind direction, the multi-fidelity framework seems to better perform on the lateral facades of the building, i.e. *left* and *right* faces, when compared to the RANS result. Nonetheless, the RANS slightly outperforms the MF model around the *top* face.

The MF model is able to correct the bias of the RANS simulation along the lateral facades, but predicts a conical vortex on the roof, that has different shape than the LES one (Figure 7.9). The maximum discrepancy between MF and LES results is now ~ 0.38 and occurs on the roof, while the maximum absolute error experienced by the RANS is ~ 0.27 and occurs on the *right* face.

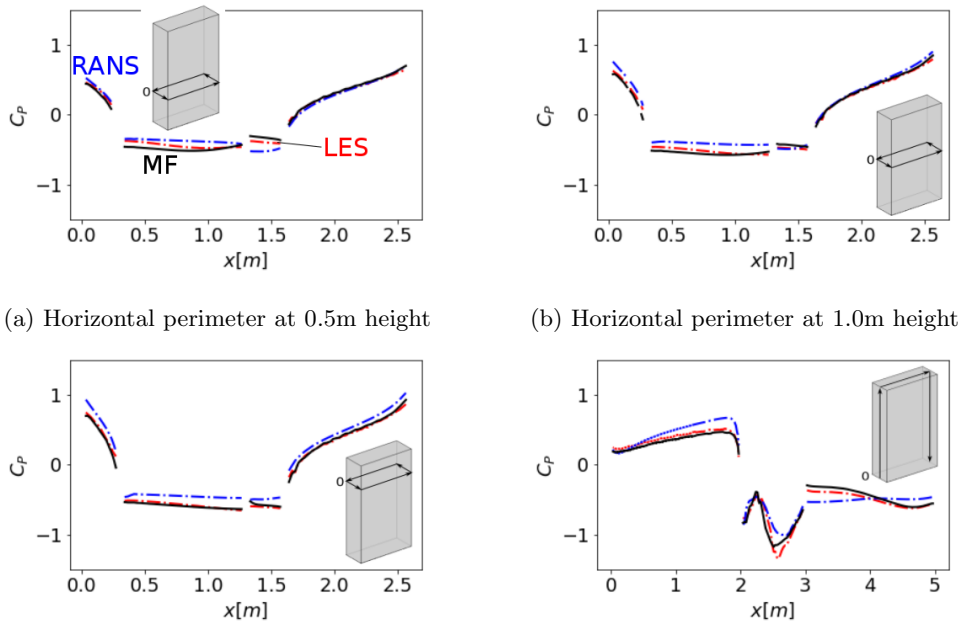

(a) Horizontal perimeter at 0.5m height

(b) Horizontal perimeter at 1.0m height

(c) Horizontal perimeter at 1.5m height

(d) Vertical perimeter

Figure 7.7: Profiles of mean pressure coefficient at 40°.

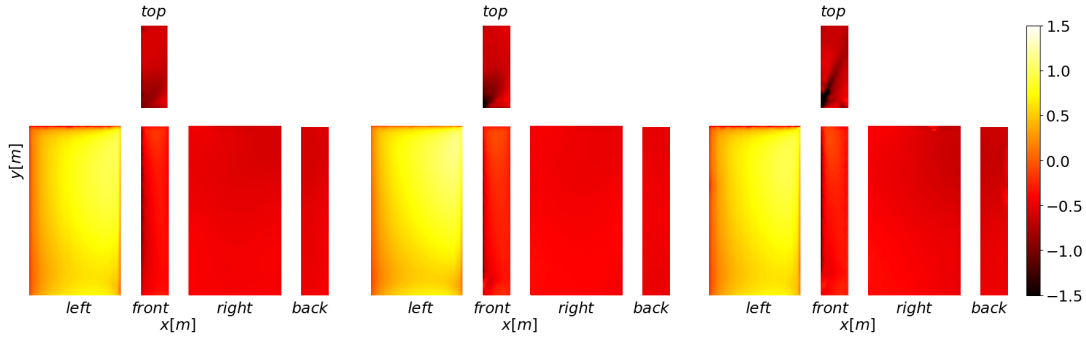

(a) LES

(b) RANS

(c) Multi-fidelity

Figure 7.8: Contours of mean pressure coefficient at 60°.

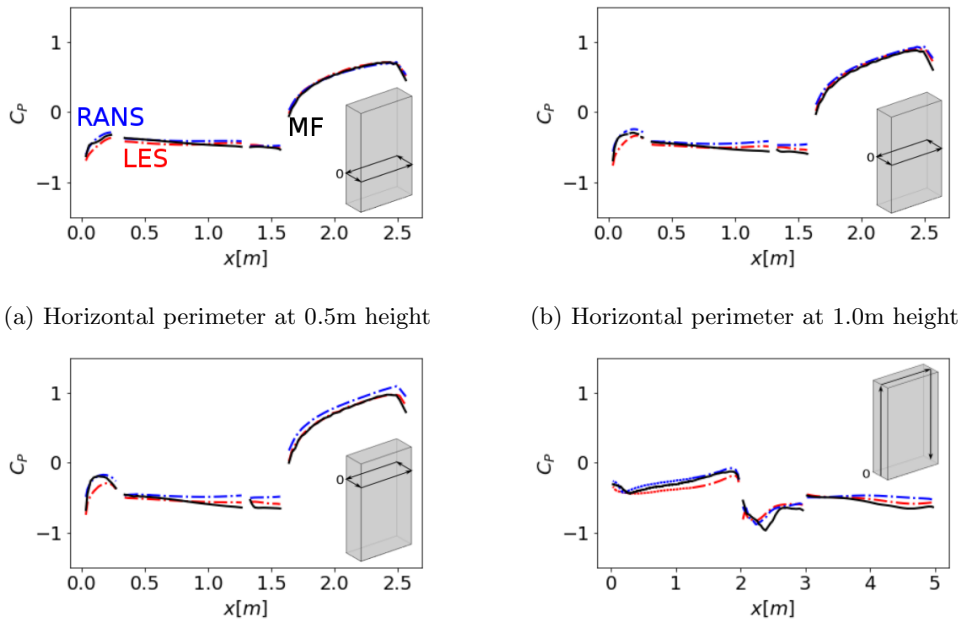

(a) Horizontal perimeter at 0.5m height

(b) Horizontal perimeter at 1.0m height

(c) Horizontal perimeter at 1.5m height

(d) Vertical perimeter

Figure 7.9: Profiles of mean pressure coefficient at 60°.

7.3.2 Rms pressure coefficient

	RANS+PH	LES: 2nd order PCE	RANS+PH: 11th order PCE	MF
0°	0.0903	0.0662	0.0860	0.0622
10°	0.0769	**0.0005**	0.0722	0.0023
20°	0.0645	**0.0276**	0.0618	0.0339
40°	0.0480	0.0185	0.0463	0.0199
45°	0.0480	**0.0000**	0.0470	0.0035
60°	0.0571	**0.0314**	0.0602	0.0388
80°	0.0537	**0.0004**	0.0538	0.0025
90°	0.0509	0.0461	0.0483	**0.0392**
tot.	0.0612	**0.0238**	0.0596	0.0253

Table 7.2: Root mean square error (RMSE) of C'_p prediction.

When considering C'_p as the QoI, the role of the low-fidelity model is played by the RANS simulation in combination with the Paterson-Holmes model. Table 7.2 reports the performance of the MF method compared to the LES- and RANS-based PCEs, and to the simple empirical model, across the wind directions. The LES-based PCE and MF models achieve similar accuracy, having a RMSE of 0.0238 and 0.0253, respectively. Conversely, the Paterson-Holmes model is characterized by a RMSE that is 2-3 higher on average. At 10°, 45° and 80° (i.e. the high-fidelity quadrature

points), both the 2nd order PCE built from the LES and the MF model are characterized by RMSE that is more than one order of magnitude lower, than at other wind directions; this means that both model manifest great degree of overfitting.

The rest of the section presents a comprehensive comparison of the C_p' outcome of the MF model, evaluated at unseen wind directions, and the corresponding LES and Paterson-Holmes results.

0° wind direction

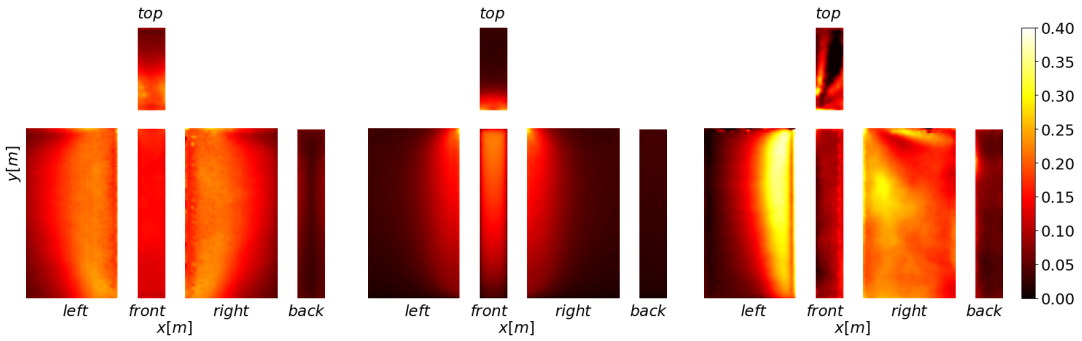

(a) LES (b) RANS + Paterson-Holmes (c) Multi-fidelity

Figure 7.10: Contours of rms pressure coefficient at 0°.

Figure 7.10 shows the contours of C_p' on the building's surface at 0° wind direction; the results of the LES (Figure 7.10a) and Paterson-Holmes model evaluated on the RANS variables (Figure 7.10b), are compared to the MF result (Figure 7.10c). In this case, neither the empirical model nor the multi-fidelity framework are able to reproduce the correct trend of C_p' around the building. The RANS is characterized by abrupt separation at the windward edge of the model, and fast recovery; the MF is able to improve the magnitude of C_p' across the lateral facades, but the correct trend is missed on the *right* and *top* faces. As for the mean pressure coefficient, the C_p' field predicted by the MF framework is not symmetric, as a consequence of the wind directions chosen as quadrature points.

Figure 7.11 plots profiles of C_p' along different perimeters of the building; the MF model provides an improvement over the empirical model, especially when considering the *left*, *right* and *back* walls. The resulting RMSE is 0.0622, which is 45% lower than the one achieved by the Paterson-Holmes model. The maximum absolute error between RANS and LES along the selected profiles, is ~ 0.14 and occurs on the lateral facades, while the maximum discrepancy between MF and LES is ~ 0.16, which occurs on the roof.

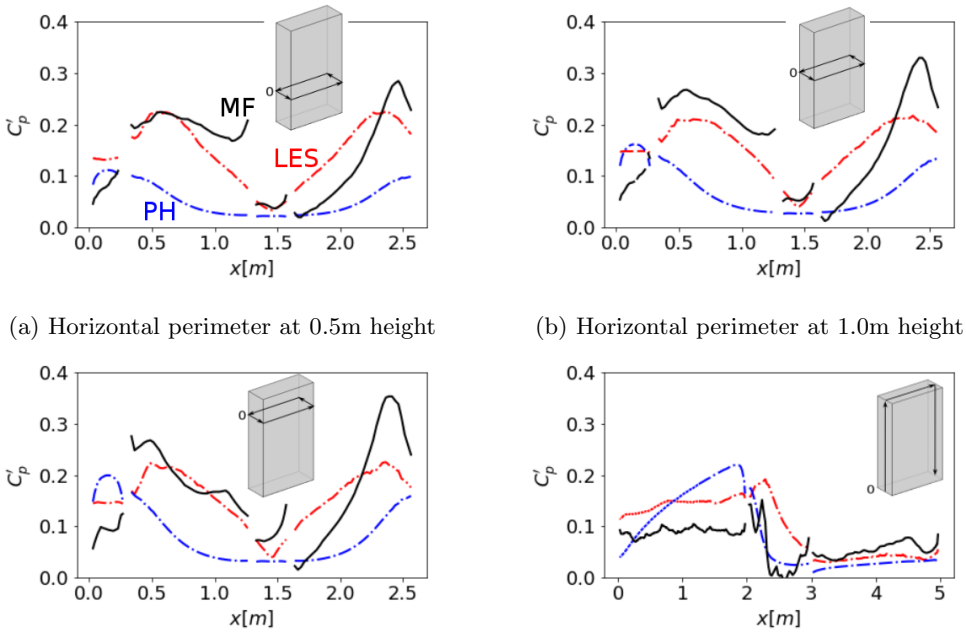

(a) Horizontal perimeter at 0.5m height

(b) Horizontal perimeter at 1.0m height

(c) Horizontal perimeter at 1.5m height

(d) Vertical perimeter

Figure 7.11: Profiles of rms pressure coefficient at 0°.

20° wind direction

Figure 7.12c shows the MF model evaluated at $\theta = 20°$ wind direction, while Figures 7.12a and 7.12b shows the results of the LES and empirical model, respectively. The MF result is in discrete agreement with the LES data, despite some discrepancies on the roof and side walls; conversely, the Paterson-Holmes model evaluated on the RANS flow field, cannot capture the correct trend of C'_p. The better performance of the MF model is also reflected in the RMSE, which is 90% lower than the one achieved by the empirical model.

The better agreement between LES and MF results is confirmed in Figure 8.9; as evident from the plots, the Paterson-Holmes model completely misses the correct trend of C'_p, while the MF update can significantly improve the prediction. The maximum absolute errors experienced by the Paterson-Holmes and MF models are ~ 0.2 and ~ 0.17, respectively.

40° wind direction

The results of the three methods at 40° are shown in Figure 7.14. At this wind direction, the agreement between the C'_p outcome of the MF model and LES data is quite good, while the performance of the Paterson-Holmes model doesn't improve across the wind directions. The RMSE of the MF result is indeed more than 2 times smaller than the one achieved by the empirical model.

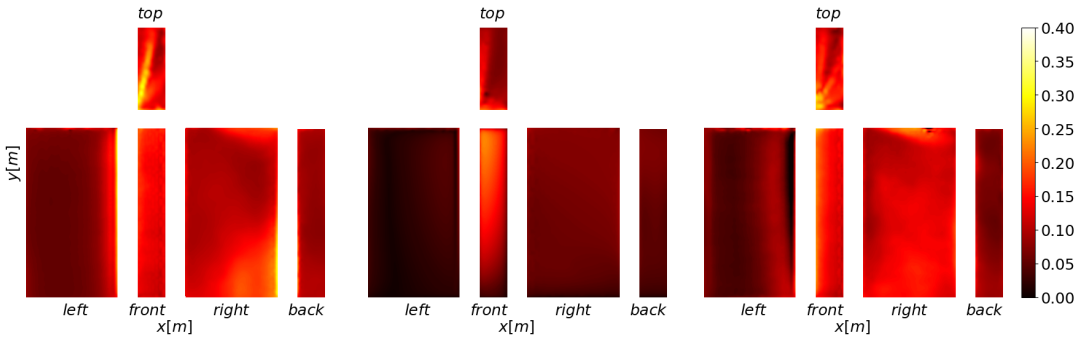

(a) LES (b) RANS + Paterson-Holmes (c) Multi-fidelity

Figure 7.12: Contours of rms pressure coefficient at 20°.

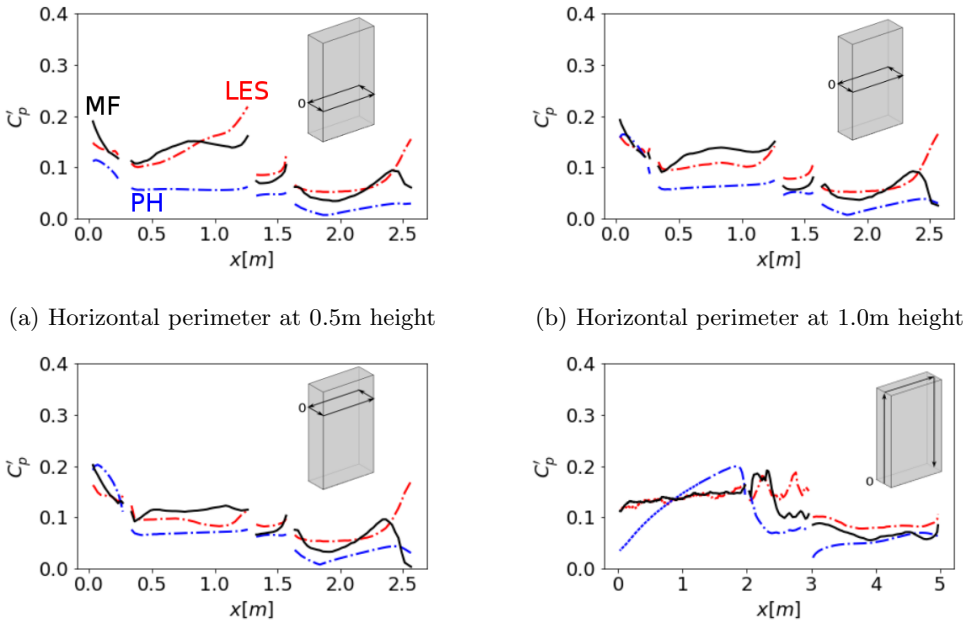

(a) Horizontal perimeter at 0.5m height (b) Horizontal perimeter at 1.0m height

(c) Horizontal perimeter at 1.5m height (d) Vertical perimeter

Figure 7.13: Profiles of rms pressure coefficient at 20°.

The plots of Figure 7.15 highlight once more the discrete performance of the MF model everywhere around the building, where the Paterson-Holmes model fails. The maximum discrepancy between the empirical model and the LES data along the profiles of Figure 7.15, is ~ 0.21, while it drops to ~ 0.07, when the multi-fidelity approach is employed.

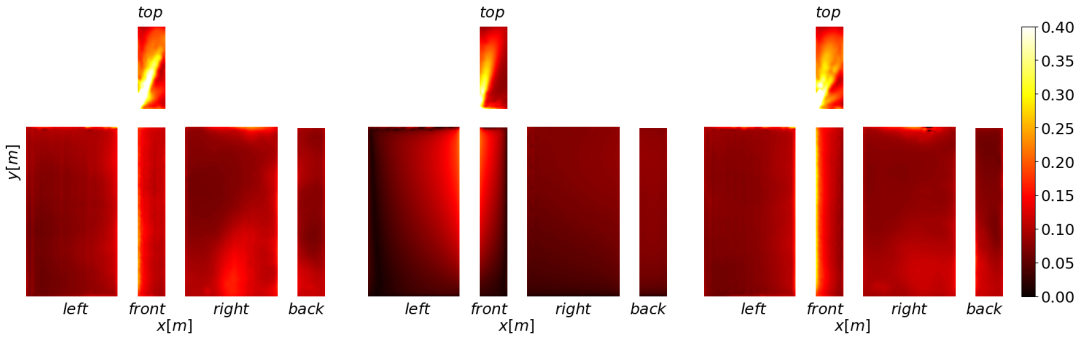

(a) LES (b) RANS + Paterson-Holmes (c) Multi-fidelity

Figure 7.14: Contours of rms pressure coefficient at 40°.

60° wind direction

Finally, Figure 7.16c shows the MF model evaluated at $\theta = 60°$, while Figures 7.16a and 7.16b show the results of the LES and empirical model, respectively. The MF result is in good agreement with the LES data on the *left*, *right* and *back* walls, while the correct trend is missed on the roof and some discrepancies exist on the *front* face. On the other hand, the Paterson-Holmes model evaluated on the RANS flow field, can capture the correct trend of C'_p only on the *top* face. As a consequence, the RMSE achieved by the empirical model is $\sim 47\%$ higher than the one achieved by the MF approach.

Similar conclusions can be drawn from Figure 7.17; discrepancies up to ~ 0.14 exist between the LES and MF results on the *front* and *top* faces, but the agreement is rather good on the side and back walls. If not for the roof, the Paterson-Holmes model misses the correct trend of C'_p, resulting in a maximum absolute error of ~ 0.16.

7.4 Summary

The chapter proposed a multi-fidelity framework that combines the information from RANS simulations, at a high number of wind directions, with the results of LES simulations, at a small subset of wind directions. The goal of the framework was twofold: (1) improve the confidence in the RANS prediction of the mean pressure coefficient on high-rise buildings, (2) enable the estimation of the rms pressure coefficient from the RANS flow field. The framework considered only the wind direction

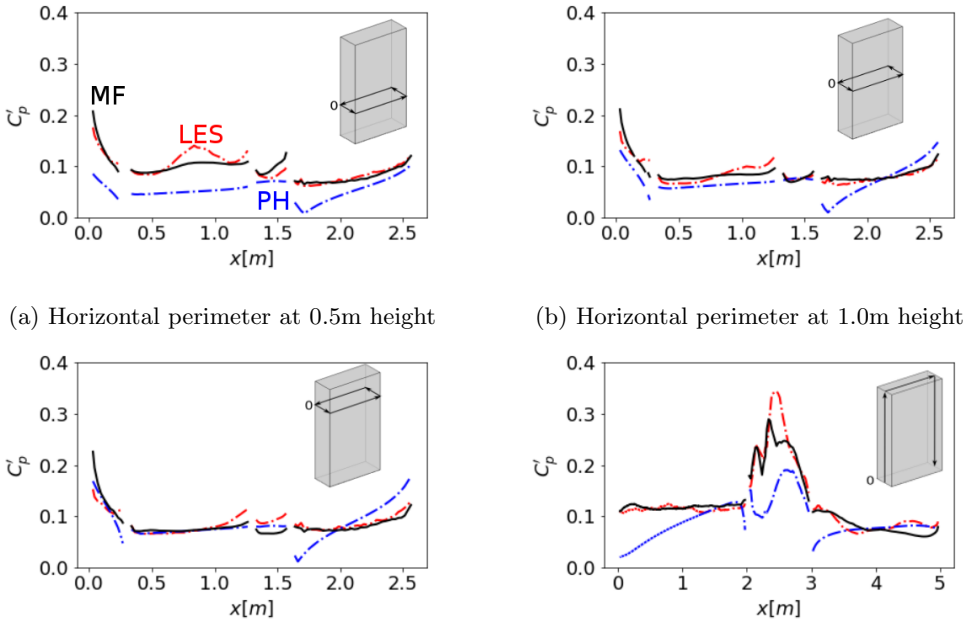

(a) Horizontal perimeter at 0.5m height

(b) Horizontal perimeter at 1.0m height

(c) Horizontal perimeter at 1.5m height

(d) Vertical perimeter

Figure 7.15: Profiles of rms pressure coefficient at 40°.

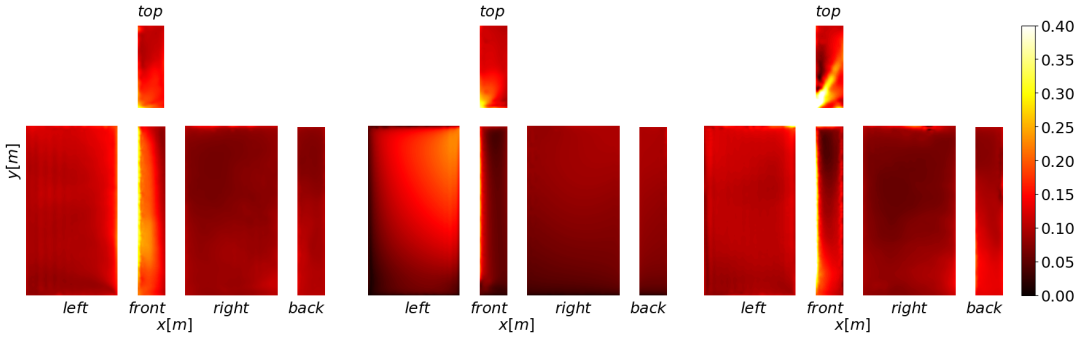

(a) LES

(b) RANS + Paterson-Holmes

(c) Multi-fidelity

Figure 7.16: Contours of rms pressure coefficient at 60°.

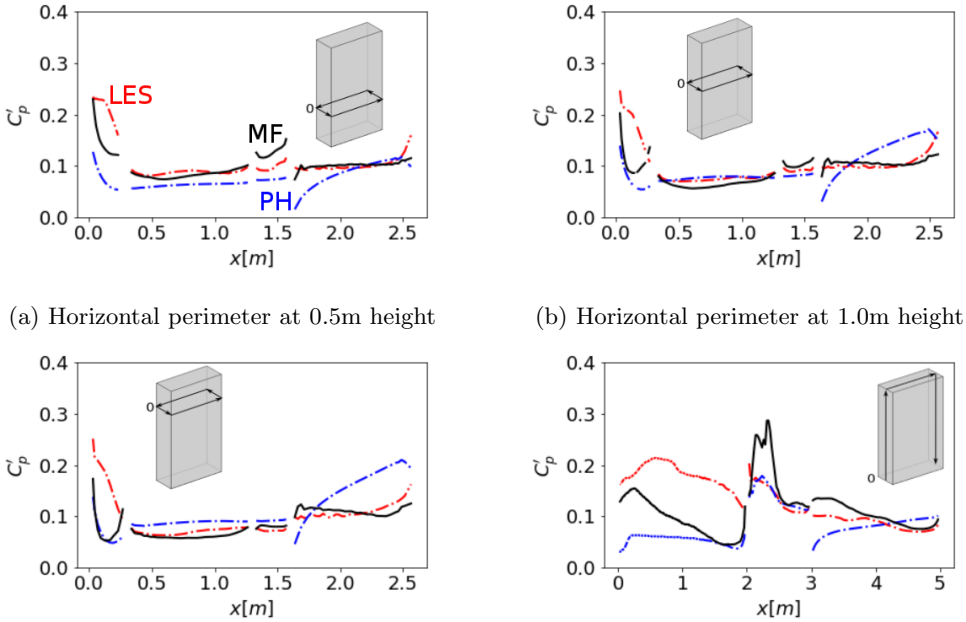

(a) Horizontal perimeter at 0.5m height

(b) Horizontal perimeter at 1.0m height

(c) Horizontal perimeter at 1.5m height

(d) Vertical perimeter

Figure 7.17: Profiles of rms pressure coefficient at 60°.

as uncertain parameter and employed non-intrusive PCE to approximate the stochastic models of both the low-fidelity model and discrepancy function between low- and high-fidelity models [84].

First, we constructed the multi-fidelity model for the mean pressure coefficient, by using RANS simulations at 15 wind directions and 3 LES simulations. The MF model represented a significant improvement over simple RANS simulations, at most of the wind directions considered. Furthermore, the MF model outperformed a pure LES-based PCE, in predicting the mean pressure coefficient at wind directions not included in the quadrature points. Three LES simulations were not enough to build a PCE that well extrapolates to unseen wind directions, while including information from the RANS simulations significantly improved the results.

Subsequently, we extended the framework to enable the computation of the rms pressure coefficient. In this case, the low-fidelity model was an empirical model evaluated on the RANS variables. When comparing the performance of the MF framework against the standard Paterson-Holmes model, at different wind directions, we saw that the MF model better reproduces the trend of C'_p around most of the building's surface. However, no advantage of using the MF approach over building a PCE from the 3 LES simulations, appeared for this QoI.

In summary, by leveraging the results of 3 LES simulations, we can significantly improve the prediction of mean and rms pressure coefficients from the RANS flow field. Nonetheless, when the low-fidelity model has poor accuracy, such as the empirical model, the MF framework is only as

good as a surrogate model built using the available LES simulations.

Chapter 8

Multi-fidelity machine learning framework

Chapter 7 showed that standard multi-fidelity methods can improve the RANS-based prediction of mean and rms pressure coefficients on high-rise buildings. Nonetheless, when the low-fidelity model is poorly correlated with the high-fidelity one, as it was the case for standard empirical models, the MF method doesn't provide any benefit over a pure LES-based surrogate model. Therefore, this chapter explores an alternative approach to improve the accuracy in the prediction of the rms pressure coefficient from time-averaged quantities. The chapter proposes a multi-fidelity machine learning approach that aims to find a functional form that well relates LES data of rms pressure coefficient to mean RANS variables. The objective of the procedure is to reduce the number of LES simulations necessary for design, while maintaining acceptable accuracy of the results. Therefore, we train different machine learning models using data from a subset of wind directions and then use these models to predict the rms pressure coefficient at the left-out wind directions.

In the remaining of the chapter, we first introduce the machine learning method; subsequently, the results of the framework at different wind directions are compared to the LES database.

8.1 Machine learning method

In the following, we first present our dataset and features; for more details about the RANS and LES setup used to obtain the dataset, the reader is referred to Section 7.1. Subsequently, we show how principle component analysis (PCA) can be used to visualize and quantify similarity between the distribution of the features across the different wind directions. Lastly, the details of the hyperparameters and model search are presented.

8.1.1 Features and Dataset

The goal of the machine learning algorithm is to find the functional form that better relates the LES data of C'_p, to 5 non-dimensional and Galilean invariant features constructed from the RANS flow variables [72], summarized in Table 8.1.

Mean pressure coefficient (C_P)	$\frac{P}{0.5\rho U_H^2}$
Non-dimensional turbulence kinetic energy	$\frac{k}{U_H^2}$
Non dimensional streamwise inlet velocity	$\frac{U_0}{U_H}$
Non-dimensional pressure gradient norm	$\frac{H\|\|\nabla P\|\|}{0.5\rho U_H^2}$
Friction coefficient (C_f)	$\frac{\|\|\tau_w\|\|}{0.5\rho U_H^2}$

Table 8.1: Features of the machine learning model, where τ_w is the wall shear stress vector and H the height of the building; ν and ρ are the kinematic viscosity and density of the air, respectively.

Similar to standard empirical models, we select the mean pressure coefficient C_P, local turbulence kinetic energy k and inflow velocity profile U_0; in addition, we include the non-dimensional norm of the pressure gradient ∇P and the friction coefficient C_f to provide further information on the various flow regimes, i.e. separation, reattachment and fully attached flow. Figure 8.1 shows contour plots of the output and the features relative to the 0° wind direction on the building's external facade; the building is unfolded to visualize the entire surface. The rms pressure coefficient (Figure 8.1a) is higher inside the separation region of the flow (yellow region of Figure 8.1a); therefore, having features that are able to distinguish regions of flow separation from regions of attached flow, is essential for the accuracy of the method. Figure 8.1 shows that, excluding the inflow velocity profile, all remaining features provide some information on the different flow regimes. Before training the models, the features are centered and normalized by subtracting their mean value and dividing by their standard deviation across the dataset. This pre-processing step allows to obtain features with similar order of magnitude, which can significantly improve the learning process.

The full dataset consists of RANS and LES simulations at 10 different wind directions, namely from 0° to 90°, with a 10° resolution. These wind directions are representative of the entire wind rose, given the symmetry of the building model. For each wind direction, we have $\sim 42,000$ data points, i.e. the number of RANS cells on the building surface, consisting of 1 output and 5 features. Since our goal is to reduce the number of LES simulations necessary for cladding design (as sketched in Figure 8.2), we will include the simulation at 10°, 30°, 50°, 70° and 90° wind directions in the training set; the test set contains the remaining 5 wind directions. In the next section, we present our approach for investigating if all training data should be used to learn a universal model that can be applied to all wind directions, or if the model accuracy can be improved by selecting a subset of the training data to obtain a different model for each wind direction in the test set.

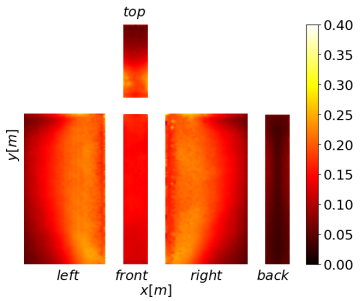

(a) Rms pressure coefficient

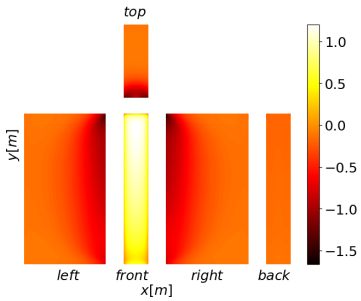

(b) Mean pressure coefficient

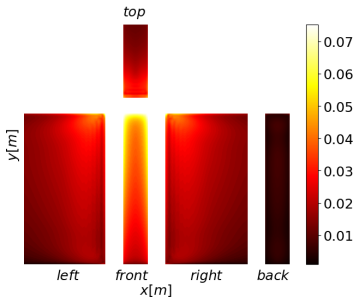

(c) Non-dimensional turbulence kinetic energy

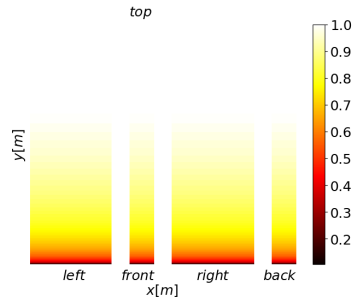

(d) Non dimensional inlet velocity

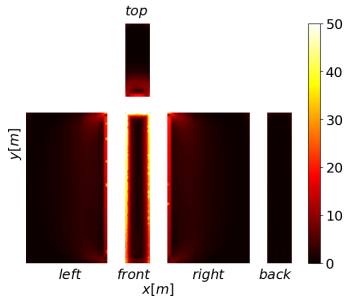

(e) Non-dimensional pressure gradient norm

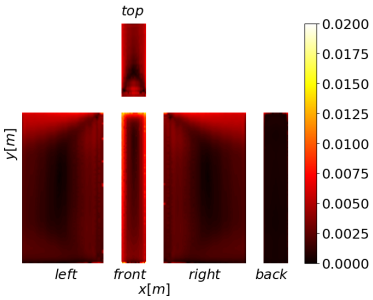

(f) Friction coefficient

Figure 8.1: Contours of the output and features at 0° wind direction.

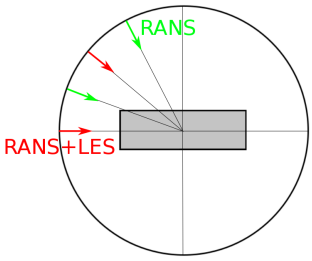

Figure 8.2: Sketch of the data-driven approach.

8.1.2 Principal component analysis

To better understand how the distribution of the features changes across the wind directions, we employ PCA [130]. The objective is to identify the wind directions in the training set that represent good training candidates for each of the tasks in the test set. As a result of PCA, the 5-dimensional feature space can be reduced to a 2-dimensional space, since most of the variance across the full dataset (i.e. including all wind directions) is explained by the first 2 principal components. Specifically, the first principal component X_1 and second principal component X_2 explain $\sim 97.5\%$ and $\sim 2.2\%$ of the variance, respectively.

Figure 8.3 shows the joint distribution of the first two principal components for all available wind directions. Even though most data points are located in a similar region of the reduced space, a variation with the wind direction can be noticed. With increasing inflow angle, the high concentration region (in red) seems to move to higher values of X_2, while a second region of relatively high probability, that arises at 10°, moves to more negative values of X_2.

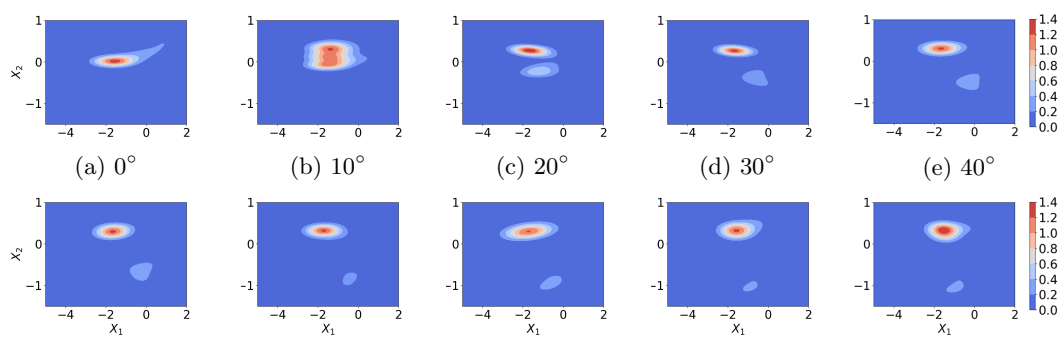

(a) 0° (b) 10° (c) 20° (d) 30° (e) 40°

(f) 50° (g) 60° (h) 70° (i) 80° (j) 90°

Figure 8.3: Contours of the joint distribution of the first two principal components.

In order to quantify the difference between the joint distributions of Figure 8.3, we compute the Kullback-Leibler divergence D_{KL} [62]:

$$D_{KL}(p||q) = \sum_i p_i \log \frac{p_i}{q_i} \tag{8.1}$$

where p_i and q_i represent the ith data points of the probability distributions p and q. Table 8.2 reports the values of D_{KL} between the wind directions in the test set (rows of Table 8.2) and the wind directions in the training set (columns of Table 8.2). For each task, the values in bold indicate the two wind directions that produce the smallest values of divergence and thus represent good candidates for training the corresponding model. Within the dataset, the 0° case deviates most from the others, having an average D_{KL} of ~ 1000 (Table 8.2).

To investigate the benefit of this analysis, Section 8.2 will compare the performance of a universal

$D_{KL}(p\|q)$	$q = 10°$	$q = 30°$	$q = 50°$	$q = 70°$	$q = 90°$	Average
$p = 0°$	**290**	1500	1100	1100	**990**	1000
$p = 20°$	**350**	**210**	350	1170	1000	770
$p = 40°$	520	**120**	**30**	370	440	300
$p = 60°$	340	390	**130**	170	**120**	290
$p = 80°$	400	790	280	**140**	**60**	420

Table 8.2: Kullback-Leibler divergence between wind directions in the test and training sets.

model, i.e. trained over the entire training set, to the approach in which 5 different models, i.e. one per wind direction in the test set, are built. For the latter approach, we will train the models using only the two wind directions that produce lowest D_{KL}, as well as consider the benefit of further experimentation to seek an even better subset of training wind directions.

8.1.3 Hyperparameters and model search

The model search and hyperparameters tuning is performed only once, by using the data at 30° wind direction for training and a left-out simulation at 45° for validation. To quantify the confidence in the machine learning prediction, we compute the mean and 95% confidence interval of C'_p using the bootstrap method [29]. Specifically, we generate $1,000$ training sets, by sampling with replacement the original training set; then, the corresponding machine learning models are trained and the ensemble of results are employed to compute a mean and confidence interval of C'_p.

The learnable parameters are computed by minimizing the squared-error loss with L2 regularization, on the training data:

$$L(\mathbf{w}) = \sum_i (y_i - f(x_i; \mathbf{w}))^2 + \lambda ||\mathbf{w}||_2^2 \tag{8.2}$$

where y_i and x_i are the output and features of the ith training example, $\mathbf{w}$ the vector of weights and λ the regularization strength.

A variety of models is considered, starting from less flexible ones, such as linear regression, to more advanced ones, such as random forests and neural networks. Table 8.3 reports the root mean square error (RMSE) in the training and validation sets, for some of the models that we considered. The RMSE is computed using the average of C'_p across the bootstrap samples.

	Train	**Valid**
Dataset	30°	45°
Linear regression (RMSE)	0.0192	0.0257
Linear regression + quadratic features (RMSE)	0.0131	0.0304
Random forest (RMSE)	0.0009	0.0270
5-layer Neural Network (RMSE)	0.0143	0.0221

Table 8.3: Root mean square error (RMSE) of the selected models.

The model that achieves the best performance in the validation set is a 5-layer neural network with 10 hidden units per layer and ReLU activation function (Figure 8.4). To train the model, we used the Adam optimization algorithm [61], with a learning rate of 0.001 and regularization strength of 0.01. Within the models considered, the neural network is the one that benefits most from the bootstrap technique: the technique prevents overfitting, which is critical for such a flexible model.

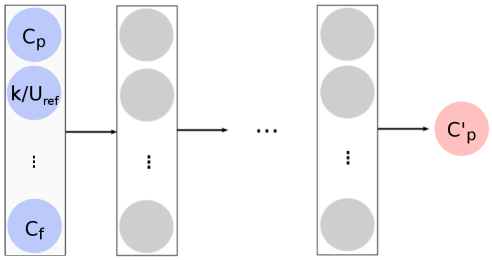

Figure 8.4: Neural network acrhirecture.

The better performance of the neural network model is confirmed in Figure 8.5, where the distribution of rms pressure coefficient around the building's surface is shown. The LES result (Figure 8.5a) is compared to the prediction given by the models listed in Table 8.3. The linear regression model with extended feature space and the random forests model manifest some degree of overfitting, which is also reflected in their low RMSE in the training set and high RMSE in the validation set (Table 8.3). Both the simple linear regression and neural network models are able to provide accurate prediction of C'_p around the building; nonetheless, the neural network slightly outperforms the linear regression model in the top and side walls, where separation and reattachment occur. Therefore, the remaining of the paper will present results obtained with the neural network. The model will be re-trained for each of the tasks in the test set, but keeping the architecture and hyperparameters fixed.

8.2 Results

In this section, first, the overall performance of the data-driven method is quantified in terms of RMSE. Furthermore, we investigate the benefit of training data selection (as outlined in Section 8.1.2) over building a universal model across the entire training set. Subsequently, we present a more comprehensive comparison between the rms pressure coefficient computed by the neural network, the LES result and empirical model prediction. For those models in which the best results are obtained using training sets different from the two wind directions with smallest D_{KL}, we also provide a comparison between the two approaches.

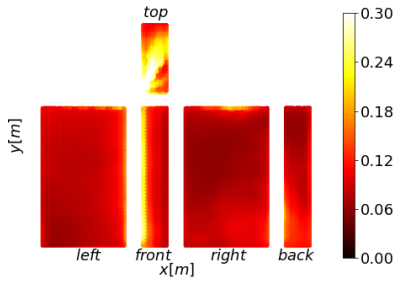

(a) LES

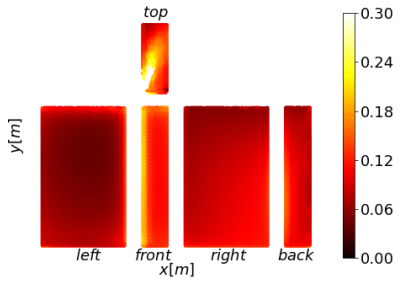

(b) Linear regression

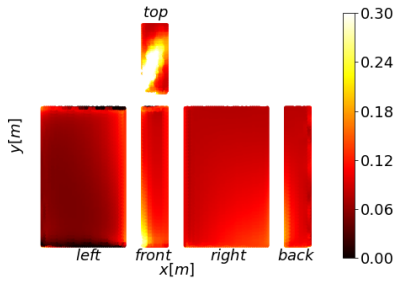

(c) Linear regression + quadratic features

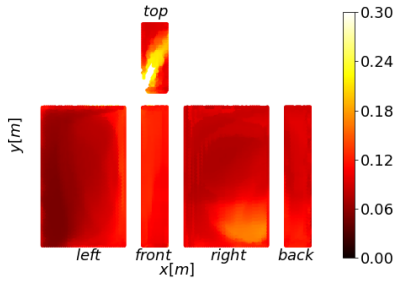

(d) Random forests

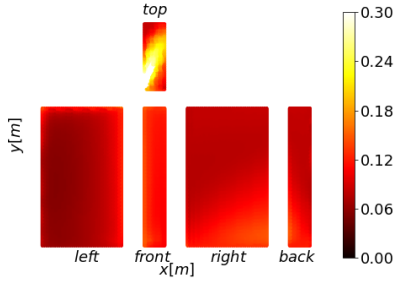

(e) Neural network

Figure 8.5: Contours of rms pressure coefficient at 45° wind direction.

0°	**Training data**	**Train RMSE**	**Test RMSE**
Paterson-Holmes	-	-	0.0897
Neural network (universal)	10°, 30°, 50°, 70°, 90°	0.0252	0.0520
Neural network (best)	10°, 90°	0.0163	0.0492
20°	**Training data**	**Train RMSE**	**Test RMSE**
Paterson-Holmes	-	-	0.0570
Neural network (universal)	10°, 30°, 50°, 70°, 90°	0.0252	0.0260
Neural network (best)	10°, 30°	0.0197	0.0252
40°	**Training data**	**Train RMSE**	**Test RMSE**
Paterson-Holmes	-	-	0.0438
Neural network (universal)	10°, 30°, 50°, 70°, 90°	0.0252	0.0334
Neural network (best)	30°, 50°	0.0149	0.0159
60°	**Training data**	**Train RMSE**	**Test RMSE**
Paterson-Holmes	-	-	0.0546
Neural network (universal)	10°, 30°, 50°, 70°, 90°	0.0252	0.0300
Neural network (lowest D_{KL})	50°, 90°	0.0147	0.0259
Neural network (best)	50°	0.0097	0.0241
80°	**Training data**	**Train RMSE**	**Test RMSE**
Paterson-Holmes	-	-	0.0475
Neural network (universal)	10°, 30°, 50°, 70°, 90°	0.0252	0.0210
Neural network (lowest D_{KL})	70°, 90°	0.0167	0.0273
Neural network (best)	50°, 70°, 90°	0.0241	0.0195
Average	**Training data**	**Train RMSE**	**Test RMSE**
Paterson-Holmes	-	-	0.0585
Neural network (universal)	-	0.0252	0.0325
Neural network (lowest D_{KL})	-	0.0166	0.0288
Neural network (best)	-	0.0166	0.0269

Table 8.4: Root mean square error (RMSE) of the neural network and Paterson-Holmes models, for each of the 5 wind directions in the test set.

8.2.1 Comparison of RMSE

Table 8.4 reports the training and test sets and RMSE relative to each of the models trained. The table summarizes the performance of the best models obtained, the performance of the models trained using only the two wind directions with lowest D_{KL}, and the performance of a single model trained over the entire training set. The simple procedure, in which all the wind directions in the training set are used to build a universal model, achieves an average RMSE of ~ 0.0325 on the test set, which already represents a $\sim 44\%$ improvement over the Paterson-Holmes model. By performing PCA and computing the Kullback-Leibler divergence to identify the two most similar wind directions to each condition, the average RMSE can be further decreased by $\sim 12\%$. Finally, by considering different combinations of the wind directions that give lowest D_{KL}, we are able to further improve the performance by $\sim 7\%$. Note that in 3 cases out of 5, i.e. 0°, 20° and 40°, no further experimentation is needed to obtain the best results.

In the end, the RMSE achieved by the best models is on average ~ 2 times smaller than the Paterson-Holmes model in the test sets, and more than 3 times smaller in the training sets. From the relatively low discrepancy between training and test errors, the neural network seems to well extrapolate to unseen wind directions. The test case to experience the worst agreement is the 0° wind direction; as explained in Section 8.1.2, this wind direction is characterized by a distribution of data that is significantly different to all the remaining wind directions. The lowest RMSE is achieved at 40° wind direction, i.e. the wind direction that is closest to the one selected for model search and hyperparameters tuning; this might indicate some level of overfitting to the validation set. Nonetheless, the variation in data distribution between 30° and 50° is not significant (Figure 8.3), meaning that the problem is better posed.

8.2.2 0° wind direction

The 0° wind direction represents a particular case in which the mean flow is symmetric and the side walls are long enough for the flow to recover from separation. The training set includes the two wind directions associated with smallest value of D_{KL}: 10° and 90°. The 10° wind direction represents the closest inflow condition, while the 90° wind direction is characterized by symmetric mean flow.

Figure 8.6 shows the contours of C_p' on the building's surface at 0° wind direction; once again, the building is unfolded to allow a complete qualitative comparison between LES data (Figure 8.6a), neural network's result averaged across the bootstrap samples (Figure 8.6b) and empirical model's result (Figure 8.6c). The neural network better captures the trend of C_p' everywhere on the building, compared to the empirical model. This is confirmed by the RMSE of 0.0492 on the test set, compared to 0.0897 of the Paterson-Holmes model. The Paterson-Holmes model inherits the limitations of the RANS simulations: the shape of the separation region appears identical between the features (dark region of Figure 8.1b) and output (yellow region of Figure 8.6c) of the model. On the other hand, the machine learning model is able to improve upon that, as evident from the yellow region of Figure

8.6b. Nonetheless, when compared to the LES result, the neural network on average under-predicts the size of the separation region and the corresponding values of C_p'.

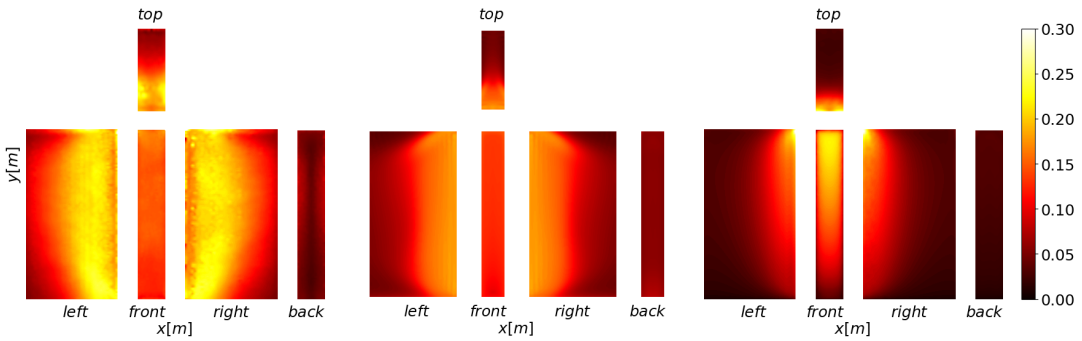

(a) LES (b) Neural network (c) Paterson-Holmes

Figure 8.6: Contours of rms pressure coefficient at 0° wind direction.

A more quantitative comparison is shown in Figure 8.7, where mean and 95% confidence interval outcome of the bootstrap procedure are compared to the LES data and empirical model, along different perimeters of the building. The plots confirm the good performance of the neural network on the *front*, *top* and *back* faces, together with the too fast recovery along the *left* and *right* facades. Overall, the bootstrap confidence interval contains 51% of the data across the entire dataset; the maximum discrepancy between confidence interval and LES data is ~ 0.1, compared to ~ 0.2 of the empirical model. The size of the interval confirms the importance of uncertainty in the input data, especially where separation and reattachment occur.

Once again, the performance of the model can be explained by the significantly different distribution of data points that characterizes the 0° wind direction.

8.2.3 20° wind direction

For this specific task the neural network model is trained using the data at 10° and 30° wind directions, namely the ones that produce the smallest values of D_{KL}. Figure 8.8 shows the contours of C_p' around the building's surface. As for the 0° case, the neural network better captures the trend of C_p' , compared to standard empirical models; the model achieves a RMSE of 0.0252 on the test set, compared to 0.0570 of the Paterson-Holmes model. The neural network is able to reproduce the correct behavior of C_p' everywhere around the building; however, on average, it over-predicts the values in the top part of the *right* face and under-predicts the values in the lower portion of the same face.

Figure 8.9 shows the mean and 95% confidence interval of the data-driven model, compared to the LES and empirical model results. Despite the relatively low RMSE, the Paterson-Holmes model totally misses the correct trend of C_p' in all the profiles considered. On the other hand, the neural

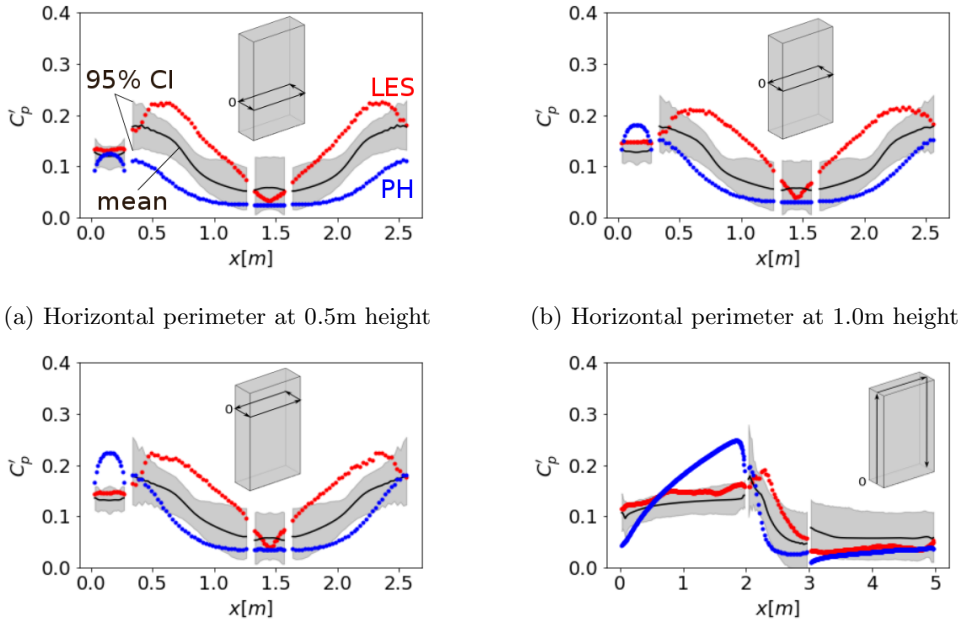

(a) Horizontal perimeter at 0.5m height

(b) Horizontal perimeter at 1.0m height

(c) Horizontal perimeter at 1.5m height

(d) Vertical perimeter

Figure 8.7: Profiles of rms pressure coefficient at 0° wind direction.

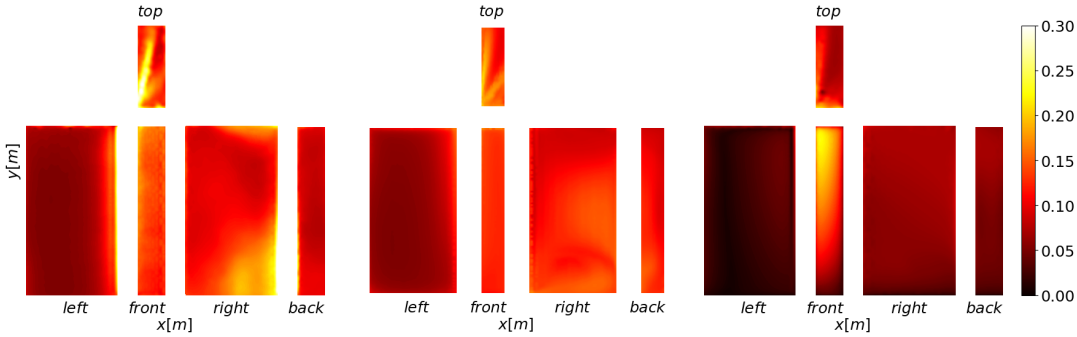

(a) LES

(b) Neural network

(c) Paterson-Holmes

Figure 8.8: Contours of rms pressure coefficient at 20° wind direction.

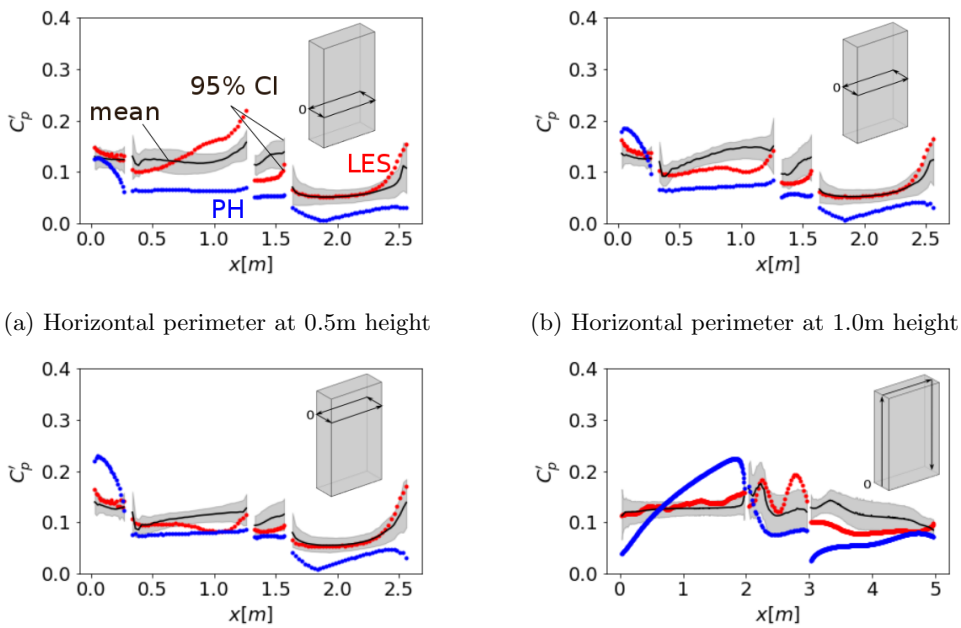

(a) Horizontal perimeter at 0.5m height

(b) Horizontal perimeter at 1.0m height

(c) Horizontal perimeter at 1.5m height

(d) Vertical perimeter

Figure 8.9: Profiles of rms pressure coefficient at 20° wind direction.

network is able to reproduce the behavior of C'_p around the building, despite some discrepancies. Across the entire dataset, the bootstrap confidence interval contains 70% of the data; the maximum discrepancy between confidence interval and LES data is ~ 0.07, compared to ~ 0.27 of the Paterson-Holmes model. The maximum discrepancy occurs in the bottom-rear portion of the *right* face.

8.2.4 40° wind direction

The data at 30° and 50° are used to train the neural network for the 40° task. Figure 8.10b shows the model result at 40°, while Figures 8.10a and 8.10c the LES data and empirical model prediction, respectively. The agreement is rather good: the neural network is able to provide accurate prediction of C'_p everywhere around the building. The resulting RMSE is 0.0159, compared to 0.0438 achieved by the Paterson-Holmes model.

The good agreement is confirmed in Figure 8.11: the LES data is almost everywhere encompassed by the framework result, along the perimeters considered. Overall, the bootstrap confidence interval contains 84% of the data; the maximum discrepancy between confidence interval and LES across the entire dataset is ~ 0.08. The maximum absolute error experienced by the empirical model is ~ 0.28.

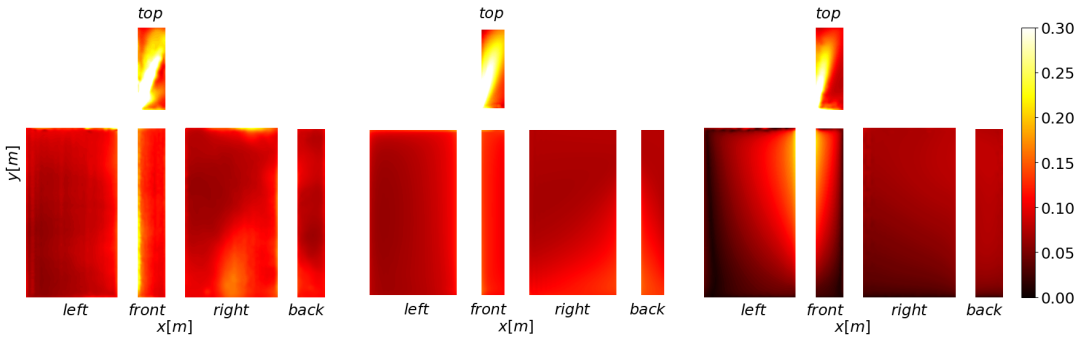

(a) LES (b) Neural network (c) Paterson-Holmes

Figure 8.10: Contours of rms pressure coefficient at 40° wind direction.

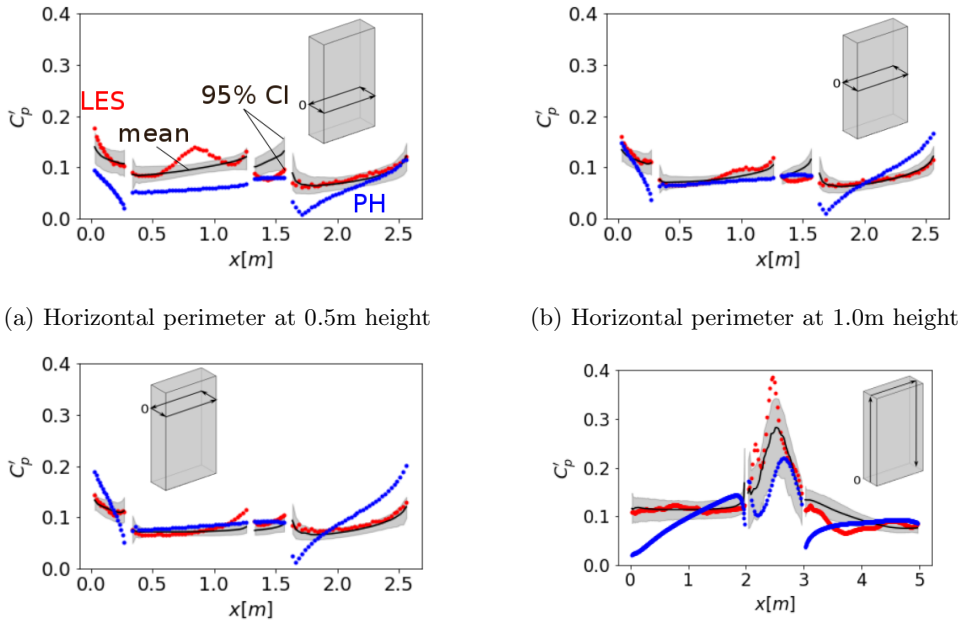

(a) Horizontal perimeter at 0.5m height (b) Horizontal perimeter at 1.0m height

(c) Horizontal perimeter at 1.5m height (d) Vertical perimeter

Figure 8.11: Profiles of rms pressure coefficient at 40° wind direction.

8.2.5 60° wind direction

To fulfill the task of predicting the rms pressure coefficient at 60° wind direction, the best results are obtained by training the neural network only on the 50° data. Figure 8.12 shows the contours of C'_p on the building's surface at 60° wind direction. The framework and LES results well agree, especially throughout the *left*, *right* and *back* faces. The *front* face is the one that manifest the worst agreement. The data-driven model outperforms the empirical model everywhere around the building, resulting in a RMSE of 0.0241 against a RMSE of 0.0546 of the Paterson-Holmes model.

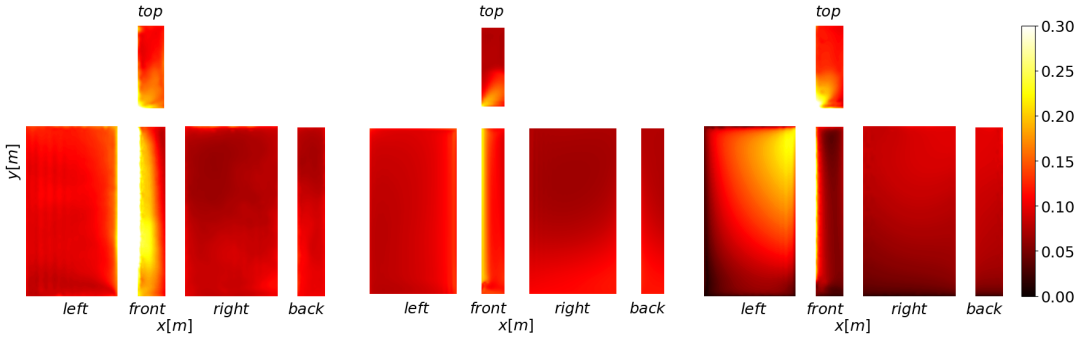

(a) LES (b) Neural network (c) Paterson-Holmes

Figure 8.12: Contours of rms pressure coefficient at 60° wind direction.

The better performance of the data-driven model, with respect to the Paterson-Holmes model, is confirmed in Figure 8.13. Overall, the bootstrap confidence interval contains 77% of the data, while the maximum discrepancy between confidence interval and LES across the entire dataset is ~ 0.07 and occurs right at the windward edge of the *front* face. The maximum absolute error resulting from the empirical model is ~ 0.16.

If the 5-layer neural network was trained using the two wind directions that produce lowest Kullback-Leibler divergence, the resulting RMSE would be 0.0259, i.e. $\sim 7\%$ higher; the bootstrap confidence interval would contain 65% of the data and the maximum absolute error would be 0.08

8.2.6 80° wind direction

The best results are obtained by training the model using the data at 50°, 70° and 90°, i.e. the three wind directions that produce lowest values of D_{KL}. Figure 8.14b shows the contours of C'_p on the building's surface at 80° wind direction, as predicted by the neural network model. The model well predicts the quantity of interest everywhere around the building, if compared to the LES data (Figure 8.14a); the corresponding RMSE is 0.0195. The empirical model instead is not able to capture the correct trend, as evident from Figure 8.14c, resulting in a RMSE of 0.0475.

The analysis is confirmed by the profiles of Figure 8.15, where mean and 95% confidence interval outcome of the framework are compared to the LES data and empirical model result. Across the

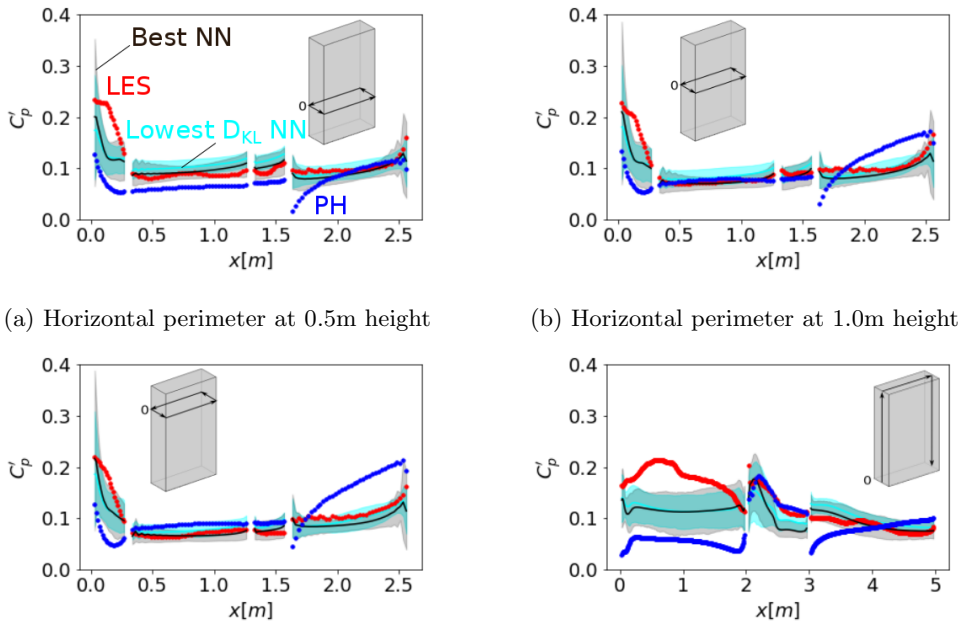

(a) Horizontal perimeter at 0.5m height

(b) Horizontal perimeter at 1.0m height

(c) Horizontal perimeter at 1.5m height

(d) Vertical perimeter

Figure 8.13: Profiles of rms pressure coefficient at 60° wind direction.

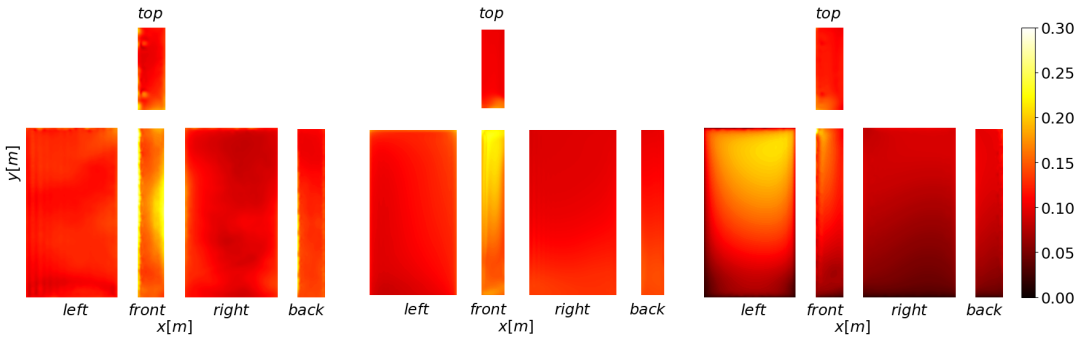

(a) LES

(b) Neural network

(c) Paterson-Holmes

Figure 8.14: Contours of rms pressure coefficient at 80° wind direction.

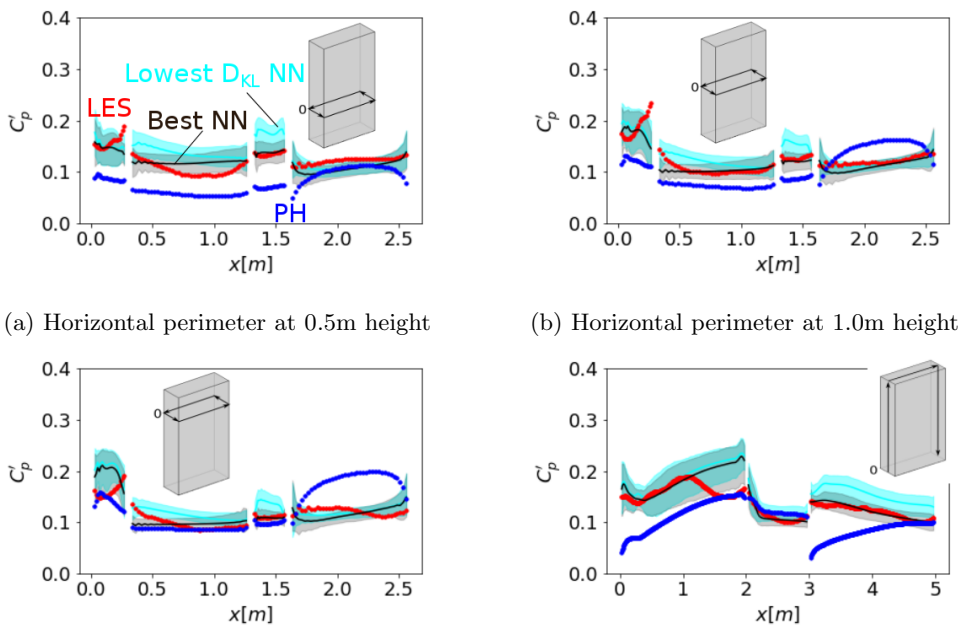

(a) Horizontal perimeter at 0.5m height

(b) Horizontal perimeter at 1.0m height

(c) Horizontal perimeter at 1.5m height

(d) Vertical perimeter

Figure 8.15: Profiles of rms pressure coefficient at 80° wind direction.

entire dataset, the bootstrap confidence interval contains 77% of the data; the maximum discrepancy between confidence interval and LES data is ~ 0.06, against a maximum absolute error of ~ 0.13 of the Paterson-Holmes model.

Figure 8.15 also shows profiles of C'_p as predicted by the neural network trained on the two wind directions with smallest D_{KL}, i.e. 70° and 90°. The model achieves a RMSE of 0.0273, i.e. $\sim 40\%$ higher than the best result. Across the entire dataset, the 95% confidence interval outcome of this model contains 52% of the data, while the maximum discrepancy remains ~ 0.06.

8.3 Summary

The present chapter proposed a multi-fidelity machine learning framework, with the goal of providing accurate predictions of rms pressure coefficient on high-rise buildings, while maintaining acceptable computational cost. The procedure sought a functional form that well relates 5 non-dimensional and Galilean invariant features, constructed from the RANS flow variables, to the C'_p outcome of the LES. Since the goal of the framework was to reduce the number of LES simulations necessary for cladding design, we split the dataset by wind directions; as a result half of the LES simulations were used only to evaluate the performance of the framework.

Principal component analysis was employed to visualize and investigate the data distribution

across the wind directions. Contour plots of the joint distribution of the first two principal components, which together explained 99.7% of the variance, showed that the data concentration can significantly change with the wind direction. As a result, we decided to build 5 machine learning models, i.e. one per wind direction in the test set, instead of seeking a unique model for all the tasks. To inform the selection of the training wind directions for each particular task, we computed the Kullback-Leibler divergence between wind directions in the test and training sets.

However, to simplify the procedure, we performed model search and hyperparameters tuning only once, by employing a left-out simulation at 45°. The model that achieved the lowest RMSE in this validation set was a 5-layer neural network with 10 hidden units per layer and ReLU activation function. The model was re-trained for each of the 5 tasks in the test set. Overall, the procedure provided a significant improvement over standard empirical models, achieving a RMSE that was on average 2 times smaller at the test wind directions and 3 times smaller at the training ones. The better performance of the framework was confirmed when looking at contour plots and profiles of rms pressure coefficient, throughout the building's surface. The neural network was able to reproduce the correct trend of C_p' almost everywhere around the building and across the wind directions, despite some discrepancies. The test case that experienced the worst agreement was the 0° one, namely the wind direction with highest average Kullback-Leibler divergence. At the remaining wind directions, the performance of the method was rather good: between 70% and 84% of the data were encompassed by the 95% bootstrap confidence interval and the maximum absolute error was 0.08.

In summary, the framework has the potential to significantly reduce the number of LES simulations needed for design, while assuring significantly higher accuracy than standard empirical models.

Chapter 9

Conclusions

9.1 Contributions

This thesis proposed a numerical framework to support the design of cladding systems at all stages. The framework includes two CFD models characterized by opposite level of fidelity and computational cost, i.e. LES and RANS, and state-of-the-art methods from the fields of optimization, uncertainty quantification and machine learning.

The first part of thesis addressed some of the issues that affect LES of ABL flows and are preventing its use for wind loading design. Specifically, we proposed an efficient inflow optimization framework, able to produce user-specified turbulence statistics at a downstream location of interest in the domain. The framework represents a substantial improvement over standard synthetic turbulence generators, in terms of accuracy of the results, and over recycling methods, in terms of efficiency and automation of the solution. The inflow optimization is the starting point of a LES UQ framework, that has not only the goal to produce desired ABL statistics, but also to account for inherent uncertainty in the definition of these target profiles. The framework provides a systematic way to address the great sensitivity to the inflow conditions, that LES on high-rise buildings manifested in literature [123], and has the potential to enable the use of LES for cladding design, as demonstrated through validation against wind tunnel data.

The second part of the thesis focused on reducing the computational cost associated with the procedure, by leveraging RANS. First, we combined previously developed UQ methods under a unique framework, which quantifies the effect of the inflow conditions and turbulence model on the RANS prediction of the mean pressure distribution on high-rise buildings. The method confirmed the well know RANS limitations in dealing with the flow around bluff bodies. To address these limitations, we developed a multi-fidelity framework, that leverages the results of few LES simulations to update the mean pressure distribution, predicted by RANS. Validation against LES at different wind directions, showed significant improvement over the standard RANS method. Finally, to enable the

use of RANS for wind loading design, we proposed a machine learning approach, which relates the rms pressure coefficient outcome of LES, to the RANS flow field. The procedure has the potential to drastically reduce the number of LES simulations needed for design, while assuring good level of accuracy.

9.2 Future work

In addition to the wind tunnel experiments presented in Chapter 3, other tests were performed at the WoW for higher Reynolds numbers and a different terrain exposure. These data will be analyzed to better understand the effect of the inflow profiles on the pressure distribution around the building. Furthermore, we will consider quantitative analysis of the space-time characteristics of the pressure signals to provide further insight on the relevance of the pressure peaks phenomena for cladding design.

Concerning the LES framework, future work will focus on the potential benefits of using a more advanced subgrid model, such as the dynamic k-equation model, particularly when considering local peak pressure coefficient. Specific to the inflow generation code, future improvements will primarily focus on a more accurate representation of the length scales. One could implement different inlet zones over the height of the surface layer, each with their own length scale. This would enable optimizing the length scales at different heights, similar to the process for optimizing the Reynolds stress profiles. We will also perform additional steps in the optimization to verify if the solution can be further improved, and implement an automatic stopping criteria that balances computational cost and maximum allowed discrepancy to the target profiles.

Regarding the RANS UQ framework, the current approach towards predicting turbulence model form uncertainty was shown to have some limitations in terms of predicting the uncertainty in the mean pressure coefficient in the region surrounding reattachment of the flow on the lateral facade. This could be related to the spatial uniformity of the directions and magnitudes of the Reynolds stress eigenvalue perturbations; the different turbulence characteristics in the stagnation region just upstream of the leeward edge versus the downstream separation region might require a non-uniform definition of the perturbations.

Finally, the multi-fidelity approach of Chapter 7 will be applied to more complicated test cases and the machine learning procedure will be extended to directly provide the peak pressure coefficient or the design pressure coefficient of glazed panels. In addition, we will explore the use of the data-driven method in support to wind tunnel experiments; in this case the goal would be to extrapolate to different regions of the building, from limited measurements locations.

Bibliography

[1] H. Aboshosha, A. Elshaer, G. T. Bitsuamlak, and A. El Damatty. Consistent inflow turbulence generator for les evaluation of wind-induced responses for tall buildings. *Journal of Wind Engineering and Industrial Aerodynamics*, 142:198–216, 2015.

[2] Tayyab Ahmad, Ajibade Aibinu, and Muhammad Jamaluddin Thaheem. The effects of high-rise residential construction on sustainability of housing systems. *Procedia engineering*, 180:1695–1704, 2017.

[3] L. Amerio. Numerical and experimental analysis of peak pressure loads on rectangular building. 2014.

[4] L. Amerio. *Experimental high resolution analysis of the pressure peaks on a building scale model façades*. PhD thesis, Politecnico di Milano, 2018.

[5] S Banerjee, R Krahl, F Durst, and Ch Zenger. Presentation of anisotropy properties of turbulence, invariants versus eigenvalue approaches. *Journal of Turbulence*, (8):N32, 2007.

[6] B. Blocken, T. Stathopoulos, and J. Carmeliet. Cfd simulation of the atmospheric boundary layer: wall function problems. *Atmospheric Environment*, 41:238–252, 2007.

[7] Bert Blocken. 50 years of computational wind engineering: past, present and future. *Journal of Wind Engineering and Industrial Aerodynamics*, 129:69–102, 2014.

[8] Bert Blocken, Ted Stathopoulos, Jan Carmeliet, and Jan LM Hensen. Application of computational fluid dynamics in building performance simulation for the outdoor environment: an overview. *Journal of Building Performance Simulation*, 4(2):157–184, 2011.

[9] Bert Blocken, Ted Stathopoulos, P Saathoff, and X Wang. Numerical evaluation of pollutant dispersion in the built environment: comparisons between models and experiments. *Journal of Wind Engineering and Industrial Aerodynamics*, 96(10-11):1817–1831, 2008.

[10] W. J. Bohnhoff, K. R. Dalbey, J. P. Eddy, J. R. Frye, R. W. Hooper, K. T Hu, P. D. Hough, M. Khalil, E. M. Ridgeway, and A. Rushdi. Dakota, a multilevel parallel object-oriented framework for design optimization, parameter estimation, uncertainty quantification, and sensitivity

analysis: version 6.6 user's manual. *Sandia National Laboratories, Tech. Rep. SAND2010-2183*, 2009.

[11] Luca Bruno, Maria Vittoria Salvetti, and Francesco Ricciardelli. Benchmark on the aerodynamics of a rectangular 5: 1 cylinder: an overview after the first four years of activity. *Journal of Wind Engineering and Industrial Aerodynamics*, 126:87–106, 2014.

[12] Steven L Brunton, Bernd R Noack, and Petros Koumoutsakos. Machine learning for fluid mechanics. *Annual Review of Fluid Mechanics*, 52:477–508, 2020.

[13] M. Caramia and P. Dell' Olmo. Multi-objective optimization. *Multi-objective Management in Freight Logistics: Increasing Capacity, Service Level and Safety with Optimization Algorithms*, pages 11–36, 2008.

[14] J E Cermak. Wind-tunnel development and trends in applications to civil engineering. *Journal of wind engineering and industrial aerodynamics*, 91(3):355–370, 2003.

[15] X Chen and A Kareem. Coupled dynamic analysis and equivalent static wind loads on buildings with three-dimensional modes. *Journal of Structural Engineering*, 131(7):1071–1082, 2005.

[16] F Cluni, V Gusella, SMJ Spence, and G Bartoli. Wind action on regular and irregular tall buildings: Higher order moment statistical analysis by hffb and smpss measurements. *Journal of Wind Engineering and Industrial Aerodynamics*, 99(6-7):682–690, 2011.

[17] Paul G Constantine, Eric Dow, and Qiqi Wang. Active subspace methods in theory and practice: applications to kriging surfaces. *SIAM Journal on Scientific Computing*, 36(4):A1500–A1524, 2014.

[18] Paul G Constantine, Michael Emory, Johan Larsson, and Gianluca Iaccarino. Exploiting active subspaces to quantify uncertainty in the numerical simulation of the hyshot ii scramjet. *Journal of Computational Physics*, 302:1–20, 2015.

[19] Nicholas J Cook. on the gaussian-exponential mixture model for pressure coefficients. *Journal of Wind Engineering and Industrial Aerodynamics*, 153:71–77, 2016.

[20] NJ Cook and JR Mayne. A novel working approach to the assessment of wind loads for equivalent static design. *Journal of Wind Engineering and Industrial Aerodynamics*, 4(2):149–164, 1979.

[21] NJ Cook and JR Mayne. A refined working approach to the assessment of wind loads for equivalent static design. *Journal of Wind Engineering and Industrial Aerodynamics*, 6(1-2):125–137, 1980.

[22] A Dagnew and Girma T Bitsuamlak. Computational evaluation of wind loads on buildings: a review. *Wind Struct*, 16(6):629–660, 2013.

[23] Agerneh K Dagnew, Girma T Bitsuamalk, and Ryan Merrick. Computational evaluation of wind pressures on tall buildings. In *11th American conference on Wind Engineering. San Juan, Puerto Rico*, 2009.

[24] Agerneh K Dagnew and Girma T Bitsuamlak. Computational evaluation of wind loads on a standard tall building using les. *Wind and Structures*, 18(5):567–598, 2014.

[25] Steven J Daniels, Ian P Castro, and Zheng-Tong Xie. Peak loading and surface pressure fluctuations of a tall model building. *Journal of Wind Engineering and Industrial Aerodynamics*, 120:19–28, 2013.

[26] Alan Garnett Davenport. The application of statistical concepts to the wind loading of structures. *Proceedings of the Institution of Civil Engineers*, 19(4):449–472, 1961.

[27] Alan Garnett Davenport. Note on the distribution of the largest value of a random function with application to gust loading. *Proceedings of the Institution of Civil Engineers*, 28(2):187–196, 1964.

[28] Karthik Duraisamy, Gianluca Iaccarino, and Heng Xiao. Turbulence modeling in the age of data. *Annual Review of Fluid Mechanics*, 51:357–377, 2019.

[29] Bradley Efron. Bootstrap methods: another look at the jackknife. In *Breakthroughs in statistics*, pages 569–593. Springer, 1992.

[30] M. Emory, J. Larsson, and G. Iaccarino. Modeling of structural uncertainties in reynolds-averaged navier-stokes closures. *Physics of Fluids*, 25(11):110822, 2013.

[31] Jörg Franke. *Best practice guideline for the CFD simulation of flows in the urban environment.* Meteorological Inst., 2007.

[32] C García-Sánchez, G Van Tendeloo, and C Gorlé. Quantifying inflow uncertainties in rans simulations of urban pollutant dispersion. *Atmospheric environment*, 161:263–273, 2017.

[33] E Gavanski and Y Uematsu. Local wind pressures acting on walls of low-rise buildings and comparisons to the japanese and us wind loading provisions. *Journal of Wind Engineering and Industrial Aerodynamics*, 132:77–91, 2014.

[34] Michael B Giles. Multilevel monte carlo path simulation. *Operations research*, 56(3):607–617, 2008.

[35] C. Gorlé, M. Emory, J. Larsson, and G. Iaccarino. Epistemic uncertainty quantification for rans modeling of the flow over a wavy wall. *Center for Turbulence Research, Annual Research Briefs*, 2012.

[36] C. Gorle, C. Garcia-Sanchez, and G. Iaccarino. Quantifying inflow and RANS turbulence model form uncertainties for wind engineering flows. *Journal of Wind Engineering and Industrial Aerodynamics*, 144:202–212, 2015.

[37] C. Gorlé, Zeoli S., M. Emory, J. Larsson, and G. Iaccarino. Epistemic uncertainty quantification for reynolds-averaged navier-stokes modeling of separated flows over streamlined surfaces. *Physics of Fluids*, 2019.

[38] R. Harris. On the spectrum and auto-correlation function of gustiness in high winds. *Electrical Research Association*, 1968.

[39] V. Holmén. Methods for vortex identification. *Master's Theses in Mathematical Sciences*, 2012.

[40] JD Holmes. Non-gaussian characteristics of wind pressure fluctuations. *Journal of Wind Engineering and Industrial Aerodynamics*, 7(1):103–108, 1981.

[41] JD Holmes. Distribution of peak wind loads on a low-rise building. *Journal of Wind Engineering and Industrial Aerodynamics*, 29(1-3):59–67, 1988.

[42] John D Holmes. *Wind loading of structures*. CRC press, 2018.

[43] John Dean Holmes. Equivalent time averaging in wind engineering. *Journal of Wind Engineering and Industrial Aerodynamics*, 72:411–419, 1997.

[44] John Dean Holmes, George Redvers Walker, and William Henry Melbourne. *A commentary on the Australian standard for wind loads AS 1170 Part 2, 1989*. Australian Wind Engineering Society, 1990.

[45] Gang Hu and KCS Kwok. Predicting wind pressures around circular cylinders using machine learning techniques. *arXiv preprint arXiv:1901.06752*, 2019.

[46] MF Huang, IWH Lau, Chun Man Chan, Kenny CS Kwok, and Guojie Li. A hybrid rans and kinematic simulation of wind load effects on full-scale tall buildings. *Journal of wind engineering and industrial aerodynamics*, 99(11):1126–1138, 2011.

[47] MF Huang, W Lou, C M Chan, N Lin, and X Pan. Peak distributions and peak factors of wind-induced pressure processes on tall buildings. *Journal of Engineering Mechanics*, 139(12):1744–1756, 2013.

[48] SH Huang, QS Li, and JR Wu. A general inflow turbulence generator for large eddy simulation. *Journal of Wind Engineering and Industrial Aerodynamics*, 98(10-11):600–617, 2010.

[49] Shenghong Huang, QS Li, and Shengli Xu. Numerical evaluation of wind effects on a tall steel building by cfd. *Journal of Constructional Steel Research*, 63(5):612–627, 2007.

[50] G. Iaccarino, A.A. Mishra, and S. Ghili. Eigenspace perturbations for uncertainty estimation of single-point turbulence closures. *Physical Review Fluids*, 2:024605, 2017.

[51] Peter Irwin, Roy Denoon, and David Scott. *Wind Tunnel Testing of High-Rise Buildings*. Routledge, 2013.

[52] N. Jarrin. *Synthetic inflow boundary conditions for the numerical simulation of turbulence*. PhD thesis, University of Manchester, 2008.

[53] N. Jarrin, S. Benhamadouche, D. Laurence, and R. Prosser. A synthetic-eddy-method for generating inflow conditions for large-eddy simulations. *International Journal of Heat and Fluid Flow*, 27(4):585–593, 2006.

[54] N Jarrin, R Prosser, J-C Uribe, S Benhamadouche, and D Laurence. Reconstruction of turbulent fluctuations for hybrid rans/les simulations using a synthetic-eddy method. *International Journal of Heat and Fluid Flow*, 30(3):435–442, 2009.

[55] Lluis Jofre, Gianluca Geraci, Hillary Fairbanks, Alireza Doostan, and Gianluca Iaccarino. Multi-fidelity uncertainty quantification of irradiated particle-laden turbulence. *arXiv preprint arXiv:1801.06062*, 2018.

[56] IM Kalkman, AJ Bronkhorst, CA van Bentum, and J Franke. A comparison of rans computations and wind tunnel tests for rms pressures on a high-rise building model. In *Proceedings of the Seventh International Colloquium on Bluff Body Aerodynamics and Applications (BBAA7) Shanghai, China; September 2-6, 2012, 1-10*, 2012.

[57] A Kareem and J Zhao. Analysis of non-gaussian surge response of tension leg platforms under wind loads. 1994.

[58] A. Keating, U. Piomelli, E. Balaras, and H.J. Kaltenbach. A priori and a posteriori tests of inflow conditions for large-eddy simulation. *Physics of Fluids*, 16(12):4696–4712, 2004.

[59] W Kim, Y Tamura, and A Yoshida. Interference effects on local peak pressures between two buildings. *Journal of Wind Engineering and Industrial Aerodynamics*, 99(5):584–600, 2011.

[60] Y. Kim, I. P. Castro, and Z. T. Xie. Divergence-free turbulence inflow conditions for large-eddy simulations with incompressible flow solvers. *Computers & Fluids*, 84:56–68, 2013.

[61] Diederik P Kingma and Jimmy Ba. Adam: A method for stochastic optimization. *arXiv preprint arXiv:1412.6980*, 2014.

[62] Solomon Kullback and Richard A Leibler. On information and sufficiency. *The annals of mathematical statistics*, 22(1):79–86, 1951.

[63] Dae Kun Kwon and Ahsan Kareem. Peak factors for non-gaussian load effects revisited. *Journal of Structural Engineering*, 137(12):1611–1619, 2011.

[64] G. Lamberti, L. Amerio, G. Pomaranzi, A. Zasso, and C. Gorlé. Comparison of high resolution pressure measurements on a high-rise building in a closed and open-section wind tunnel. *Journal of wind engineering and industrial aerodynamics*, 2020.

[65] G. Lamberti, C. García-Sánchez, J. Sousa, and C. Gorlé. Optimizing turbulent inflow conditions for large-eddy simulations of the atmospheric boundary layer. *Journal of Wind Engineering and Industrial Aerodynamics*, 177:32–44, 2018.

[66] R. Laraufie, S. Deck, and P. Sagaut. A dynamic forcing method for unsteady turbulent inflow conditions. *Journal of Computational Physics*, 230(23):8647–8663, 2011.

[67] T V Lawson. *Wind Effects on Buildings: Design Applications*, volume 1. Spon Press, 1980.

[68] TV Lawson. The design of cladding. *Building and Environment*, 11(1):37–38, 1976.

[69] Yu-Tai Lee, William K Blake, and Theodore M Farabee. Modeling of wall pressure fluctuations based on time mean flow field. *Journal of Fluids Engineering*, 127(2):233–240, 2005.

[70] Hee Chang Lim, TG Thomas, and Ian P Castro. Flow around a cube in a turbulent boundary layer: Les and experiment. *Journal of Wind Engineering and Industrial Aerodynamics*, 97(2):96–109, 2009.

[71] Julia Ling, Reese Jones, and Jeremy Templeton. Machine learning strategies for systems with invariance properties. *Journal of Computational Physics*, 318:22–35, 2016.

[72] Julia Ling and J Templeton. Evaluation of machine learning algorithms for prediction of regions of high reynolds averaged navier stokes uncertainty. *Physics of Fluids*, 27(8):085103, 2015.

[73] K. Liu and R. H. Pletcher. Inflow conditions for the large eddy simulation of turbulent boundary layers: a dynamic recycling procedure. *Journal of Computational Physics*, 219(1):1–6, 2006.

[74] Xiaoping Liu, Jianlei Niu, and Kenny CS Kwok. Evaluation of rans turbulence models for simulating wind-induced mean pressures and dispersion around a complex-shaped high-rise building. In *Building Simulation*, volume 6, pages 151–164. Springer, 2013.

[75] T. S. Lund, X. Wu, and K. D. Squires. Generation of turbulent inflow data for spatially-developing boundary layer simulations. *Journal of Computational Physics*, 140(2):233–258, 1998.

[76] E Maruta, M Kanda, and J Sato. Effects on surface roughness for wind pressure on glass and cladding of buildings. *Journal of Wind Engineering and Industrial Aerodynamics*, 74:651–663, 1998.

[77] WH Melbourne. Comparison of measurements on the caarc standard tall building model in simulated model wind flows. *Journal of Wind Engineering and Industrial Aerodynamics*, 6(1-2):73–88, 1980.

[78] Pedro M Milani and John K Eaton. Magnetic resonance imaging, optimization, and machine learning to understand and model turbulent mixing. *Magnetic Resonance Imaging*, 10:13, 2018.

[79] Pedro M Milani, Julia Ling, and John K Eaton. Physical interpretation of machine learning models applied to film cooling flows. *Journal of Turbomachinery*, 141(1):011004, 2019.

[80] Akashi Mochida and Isaac YF Lun. Prediction of wind environment and thermal comfort at pedestrian level in urban area. *Journal of wind engineering and industrial aerodynamics*, 96(10-11):1498–1527, 2008.

[81] D Mohotti, K Wijesooriya, and D Dias-da Costa. Comparison of reynolds averaging navier-stokes (rans) turbulent models in predicting wind pressure on tall buildings. *Journal of Building Engineering*, 21:1–17, 2019.

[82] Hamid Montazeri and Bert Blocken. Cfd simulation of wind-induced pressure coefficients on buildings with and without balconies: validation and sensitivity analysis. *Building and Environment*, 60:137–149, 2013.

[83] L.W.T. Ng and M.S. Eldred. Multifidelity uncertainty quantification using non-intrusive polynomial chaos and stochastic collocation. In *53rd AIAA/ASME/ASCE/AHS/ASC Structures, Structural Dynamics and Materials Conference*, 2012.

[84] L.W.T. Ng and M.S. Eldred. Multifidelity uncertainty quantification using non-intrusive polynomial chaos and stochastic collocation. *53rd AIAA/ASME/ASCE/AHS/ASC Structures, Structural Dynamics and Materials Conference*, 2:024605, 2017.

[85] K. Nozawa and T. Tamura. Large eddy simulation of the flow around a low-rise building immersed in a rough-wall turbulent boundary layer. *Journal of Wind Engineering and Industrial Aerodynamics*, 90(10):1151–1162, 2002.

[86] OpenAIRE. Zenodo. https://zenodo.org, 2019.

[87] A. Parente, C. Gorle, J. van Beeck, and C. Benocci. Improved kappa-epsilon model and wall function formulation for the RANS simulation of ABL flows. *Journal of Wind Engineering and Industrial Aerodynamics*, 99:267–278, 2011.

[88] D A Paterson, J Holmes, et al. Computation of wind flow around the texas tech building. 1989.

[89] DA Paterson. Predicting rms pressures from computed velocities and mean pressures. In *Computational Wind Engineering 1*, pages 431–437. Elsevier, 1993.

[90] L Patruno and M Ricci. A systematic approach to the generation of synthetic turbulence using spectral methods. *Computer Methods in Applied Mechanics and Engineering*, 340:881–904, 2018.

[91] L Patruno, M Ricci, S De Miranda, and F Ubertini. Numerical simulation of a 5: 1 rectangular cylinder at non-null angles of attack. *Journal of Wind Engineering and Industrial Aerodynamics*, 151:146–157, 2016.

[92] Benjamin Peherstorfer, Karen Willcox, and Max Gunzburger. Survey of multifidelity methods in uncertainty propagation, inference, and optimization. *Siam Review*, 60(3):550–591, 2018.

[93] Xinlai Peng, Luping Yang, Eri Gavanski, Kurtis Gurley, and David Prevatt. A comparison of methods to estimate peak wind loads on buildings. *Journal of wind engineering and industrial aerodynamics*, 126:11–23, 2014.

[94] R. Poletto, T. Craft, and A. Revell. A new divergence free synthetic eddy method for the reproduction of inlet flow conditions for les. *Flow, turbulence and combustion*, 91(3):519–539, 2013.

[95] Stephen B Pope. Turbulent flows, 2001.

[96] M Ricci, L Patruno, I Kalkman, S de Miranda, and B Blocken. Towards les as a design tool: Wind loads assessment on a high-rise building. *Journal of Wind Engineering and Industrial Aerodynamics*, 180:1–18, 2018.

[97] PJ Richards and BS Wanigaratne. A comparison of computer and wind-tunnel models of turbulence around the silsoe structures building. *Journal of Wind Engineering and Industrial Aerodynamics*, 46:439–447, 1993.

[98] W Rodi. Comparison of les and rans calculations of the flow around bluff bodies. *Journal of wind engineering and industrial aerodynamics*, 69:55–75, 1997.

[99] Luna M Rodriguez, Paul E Bieringer, and Tom Warner. Urban transport and dispersion model sensitivity to wind direction uncertainty and source location. *Atmospheric environment*, 64:25–39, 2013.

[100] PJ Saathoff and WH Melbourne. The generation of peak pressures in separated/reattaching flows. *Journal of Wind Engineering and Industrial Aerodynamics*, 32(1-2):121–134, 1989.

[101] Fahim Sadek and Emil Simiu. Peak non-gaussian wind effects for database-assisted low-rise building design. *Journal of Engineering Mechanics*, 128(5):530–539, 2002.

[102] Michael Schatzmann and Bernd Leitl. Issues with validation of urban flow and dispersion cfd models. *Journal of Wind Engineering and Industrial Aerodynamics*, 99(4):169–186, 2011.

[103] U. Schumann. Realizability of reynolds-stress turbulence models. *The Physics of Fluids*, 20(5):721–725, 1977.

[104] Stanford University SDR. Stanford digital repository. https://library.stanford.edu/research/stanford-digital-repository, 2019.

[105] R Panneer Selvam. Computation of pressures on texas tech building. *Journal of Wind Engineering and Industrial Aerodynamics*, 43(1-3):1619–1627, 1992.

[106] Pranay Seshadri, Shahrokh Shahpar, Paul Constantine, Geoffrey Parks, and Mike Adams. Turbomachinery active subspace performance maps. *Journal of Turbomachinery*, 140(4), 2018.

[107] Lawrence Sirovich. Turbulence and the dynamics of coherent structures. i. coherent structures. *Quarterly of applied mathematics*, 45(3):561–571, 1987.

[108] J Smagorinsky. General circulation experiments with the primitive equations: I. the basic experiment. *Monthly weather review*, 91(3):99–164, 1963.

[109] A Smirnov, S Shi, and I Celik. Random flow generation technique for large eddy simulations and particle-dynamics modeling. *Journal of Fluids Engineering*, 123(2):359–371, 2001.

[110] R. C. Smith. *Uncertainty quantification: theory, implementation, and applications*, volume 12. Siam, 2013.

[111] J Sousa, C García-Sánchez, and C Gorlé. Improving urban flow predictions through data assimilation. *Building and Environment*, 132:282–290, 2018.

[112] J. Sousa and G. Paniagua. Entropy minimization design approach of supersonic internal passages. *Entropy*, 17(8):5593–5610, 2015.

[113] C G Speziale and S Thangam. Analysis of an rng based turbulence model for separated flows. 1992.

[114] T Stathopoulos. *Turbulent wind action on low rise Structures.* PhD thesis, PhD Thesis, Univ. of Western Ontario, 1979.

[115] Theodore Stathopoulos. The numerical wind tunnel for industrial aerodynamics: Real or virtual in the new millennium? *Wind and Structures*, 5(2_3_4):193–208, 2002.

[116] D Surry and D Djakovich. Fluctuating pressures on models of tall buildings. *Journal of Wind Engineering and Industrial Aerodynamics*, 58(1-2):81–112, 1995.

[117] D Surry and T Stathopoulos. An experimental approach to the economical measurement of spatially-averaged wind loads. *Journal of Wind Engineering and Industrial Aerodynamics*, 2(4):385–397, 1978.

[118] Laura P Swiler, Thomas L Paez, and Randall L Mayes. Epistemic uncertainty quantification tutorial. In *Proceedings of the 27th International Modal Analysis Conference*, 2009.

[119] G. R Tabor and M.H. Baba-Ahmadi. Inlet conditions for large eddy simulation: a review. *Computers & Fluids*, 39(4):553–567, 2010.

[120] T Tamura. Towards practical use of les in wind engineering. *Journal of Wind Engineering and Industrial Aerodynamics*, 96(10-11):1451–1471, 2008.

[121] G. I. Taylor. The spectrum of turbulence. In *Proceedings of the Royal Society of London A: Mathematical, Physical and Engineering Sciences*, volume 164, pages 476–490. The Royal Society, 1938.

[122] Marco Tezzele, Francesco Ballarin, and Gianluigi Rozza. Combined parameter and model reduction of cardiovascular problems by means of active subspaces and pod-galerkin methods. In *Mathematical and Numerical Modeling of the Cardiovascular System and Applications*, pages 185–207. Springer, 2018.

[123] Marie Skytte Thordal, Jens Chr Bennetsen, and H Holger H Koss. Review for practical application of cfd for the determination of wind load on high-rise buildings. *Journal of Wind Engineering and Industrial Aerodynamics*, 186:155–168, 2019.

[124] Yoshihide Tominaga, Akashi Mochida, Shuzo Murakami, and Satoshi Sawaki. Comparison of various revised k–ε models and les applied to flow around a high-rise building model with 1: 1: 2 shape placed within the surface boundary layer. *Journal of Wind Engineering and Industrial Aerodynamics*, 96(4):389–411, 2008.

[125] T Tschanz and A G Davenport. The base balance technique for the determination of dynamic wind loads. In *Wind Engineering 1983, Part 3A*, pages 429–439. Elsevier, 1984.

[126] M Tsuchiya, S Murakami, A Mochida, K Kondo, and Y Ishida. Development of a new k-ε model for flow and pressure fields around bluff body. *Journal of Wind Engineering and Industrial Aerodynamics*, 67:169–182, 1997.

[127] Meng Wang and Parviz Moin. Dynamic wall modeling for large-eddy simulation of complex turbulent flows. *Physics of Fluids*, 14(7):2043–2051, 2002.

[128] Peter Welch. The use of fast fourier transform for the estimation of power spectra: a method based on time averaging over short, modified periodograms. *IEEE Transactions on audio and electroacoustics*, 15(2):70–73, 1967.

[129] Norbert Wiener. The homogeneous chaos. *American Journal of Mathematics*, 60(4):897–936, 1938.

[130] Svante Wold, Kim Esbensen, and Paul Geladi. Principal component analysis. *Chemometrics and intelligent laboratory systems*, 2(1-3):37–52, 1987.

[131] X. Wu. Inflow turbulence generation methods. *Annual Review of Fluid Mechanics*, 49:23–49, 2017.

[132] Z. T. Xie and I. P. Castro. Efficient generation of inflow conditions for large eddy simulation of street-scale flows. *Flow, turbulence and combustion*, 81(3):449–470, 2008.

[133] S. Zéoli. *Numerical simulation of flows with application to wind engineering problems.* PhD thesis, University of Mons, 2018.

[134] JW Zhang and QS Li. Field measurements of wind pressures on a 600 m high skyscraper during a landfall typhoon and comparison with wind tunnel test. *Journal of Wind Engineering and Industrial Aerodynamics*, 175:391–407, 2018.